NORTHWESTERN UNIVERSITY

The Functional Organization of Excitatory Synaptic Input to Place Cells in the Hippocampus

A DISSERTATION

SUBMITTED TO THE GRADUATE SCHOOL
IN PARTIAL FULFILLMENT OF THE REQUIREMENTS

for the degree

DOCTOR OF PHILOSOPHY

Field of Neuroscience

By

Michael Adoff

EVANSTON, ILLINOIS

March 2020

Abstract

The hippocampus has been identified as a critical structure for supporting spatial memory processes in both humans and animals alike. Many of these processes such as the ability to self-localize in a given environment as well as engage in goal-directed navigation are thought to depend on the location-specific firing of CA1 hippocampal pyramidal neurons called place cells. The position of an environment at which the firing rate of a place cell increases is called its place field and the formation of this field is thought to depend on the integration of spatial inputs from upstream brain regions. While experimental work in vitro has shown that CA1 hippocampal pyramidal neurons are capable of both passive and active forms of synaptic integration, surprisingly little is known about how these inputs are integrated to generate a place cell's spatially precise activity patterns in vivo. This is largely due the inherent difficulty of obtaining electrical recordings from pyramidal neuron dendrites in awake, behaving animals, a prerequisite for identifying place cells in rodents.

Currently, in vivo imaging exists as one of the few techniques available to probe subcellular activity in the behaving animal. Thus, the aim of my dissertation work was to determine the functional and anatomical organization of synaptic input to hippocampal place cells during active navigation behavior using in vivo two-photon imaging of glutamate activity. By investigating the patterns of synaptic activity which underlie place cell firing, it is possible to gain a greater understanding of how individual neurons process behaviorally-relevant information in the intact brain. Additionally, determining the rules by which dendrites process input under normal conditions will help address how abnormalities in input integration can result in neuropathological disease.

Acknowledgements

I would first like to thank my wife Kim for both marrying during my graduate career and not divorcing me over the course of it for incessant complaining. Also, I would like to thank her for her endless support. I would like to thank my PI Dan Dombeck for his mentorship throughout everything. He was always there for me, whether I wanted him to be or not, and without him I would not have been able to finish this project or have become the scientist I am today. I would like to thank all my friends, both within Northwestern and outside of it for making me laugh when I needed it. I would like thank Mark Sheffield for taking me under his wing and teaching me so much as well as letting me watch his dog Charlie. I would also like to thank Mark Howe for many discussions and for treating me to dinner so many times. No matter how down I was I could always count on beating Mark in squash to raise my mood. I would specifically like to thank Anant Jain for all his help with the ephys experiments and for just being a good friend. Same to my fellow graduate student and lab mate Brad Randvansky who always was there to talk or sing some karaoke. Thanks for being a good friend. I would like to thank both Jason Climer and Heydar Davoudi for helping to make my project into something we can all be proud of. To all my basketball teammates/lab mates, keep up the good fight and raise my jersey to the rafters during intramurals this year. Lastly, I would like to thank my dog Teddy who I love dearly and who supported me maybe more than anyone. Thank you everyone.

Table of Contents

Table of Figures

Chapter 1: General Introduction

1.1 The Hippocampus and Spatial Memory

How are the features of the world around us represented and stored in the brain? For centuries, this question has captivated philosophers and scientists alike, and remains one of the most studied but still unsettled questions in systems neuroscience. The ability to recall and use representations of previous experiences, i.e. memories, to alter future behavioral outcomes in response to environmental changes is a hallmark of higher order cognition. Yet, unlike in sensory systems, the existence of a dedicated neural circuit specifically responsible for representing the conjunctive features of a memory was still an uncertainty and thus defining the actual biological phenomenon underlying this process remained as elusive as the concept of memory itself. A major breakthrough came from studies of human patients who've experienced damage to their temporal lobe, the most well-known being Henry Molaison i.e. patient H.M. Following the bilateral lesioning of his medial temporal lobes (including the hippocampal formation) to treat severe epilepsy, H.M. demonstrated profound deficits in his ability to form new episodic memories but retained most sematic memories from the years prior to his operation (Scoville and Milner 1957).

The severity of H.M.'s deficits prompted researchers to turn to electrophysiological approaches in animal models to further investigate hippocampal function. This resulted in the next big breakthrough, the discovery of neurons in the rat hippocampus that selectively fire as a function of an animal's spatial position (O'Keefe and Dostrovsky 1971), aptly named place cells. Neighboring place cells were shown to fire at different spatial locations and through their combined activity were thought to provide the animal with a map-like representation of the entire environment (O'Keefe 1976). Based on this finding and inspired by Tolman's theory that rats use internal cognitive maps to navigate and complete goal-directed behaviors (Tolman 1948), it was proposed that place cells serve as the basic unit of a cognitive map. Thus, through the coordinated activity of multiple place cells an animal gains an allocentric representation of space defined by its own spatial position in respect to landmarks (O'Keefe and Nadel 1978). The discovery of these cells, along with human lesion studies of the temporal lobe, revolutionized the study of memory and identified the hippocampus as a critical brain structure for supporting spatial memory processes in both humans and animals alike. Additionally, the discovery that discrete physical locations in space can be represented by neural activity in the hippocampus provided an experimentally accessible means to study how different external features and components of position are mapped in the brain and advanced the view that the hippocampus serves as the neural substrate for an internal representation of space. The neural mechanisms involved in guiding navigation and spatial memories may also underlie other types of memories encoded in the hippocampus, such as declarative memories. Thus, investigating the mechanisms by which place cells generate their activity may provide insight into the general principles of hippocampal memory formation (Buzsaki and Moser 2013).

1.2 Circuit Anatomy of the Hippocampus and CA1 cellular morphology

The hippocampus is one of the most studied regions of the brain dating back to Ramon y Cajal’s original depictions of hippocampal anatomy more than a century ago. Anatomical tracing studies since then have unveiled the primary glutamatergic circuitry comprising the hippocampal formation and its connectivity patterns. Based on the work of Lorente de Nó, the hippocampus can be subdivided into distinct regions based on projections patterns and cellular morphologies. These include the dentate gyrus (DG) and cornu Ammonis areas, CA3, CA2 and CA1(Lorente De Nó 1934). The different regions of the hippocampus are coupled through distinct and largely unidirectional projections. The predominant excitatory pathway, termed the “trisynaptic circuit”, originates from the superficial layers of the medial entorhinal cortex (MECII) and goes to granule cells in the dentate gyrus through the perforant pathway. The granule cells send their projections to pyramidal neurons in the CA3 region which make recurrent connections back onto themselves before projecting to the neurons in the CA1 region through the Schaffer collaterals. CA1 neurons then complete this synaptic loop by projecting back to the deeper layers of the EC by way of the subiculum. CA1 neurons also receive direct monosynaptic input from layer III of the EC via the temporoammonic pathway. The hippocampus has a laminar organization such that the somata of individual CA1 pyramidal cells are restricted to a single layer termed the stratum pyramidale (S-P). The dendritic tree of each cell is comprised of two distinct compartments which span longitudinally across the remaining layers. The basal dendritic domain extends from the base of the cell body into the stratum oriens (S-O) and the apical dendritic domain branches from the apex of the cell into the stratum radiatum (S-R) and stratum lacunosum-moleculare (S-LM).

In rodents, a single CA1 pyramidal neuron receives approximately 30,000 excitatory synaptic inputs which are scattered across a dendritic arbor spanning a length of approximately 12 mm. Pyramidal neurons in the adjacent CA3 region provide the majority of these inputs which primarily synapse onto basal dendrites in the S-O and proximal apical dendrites in the S-R. The EC also sends a small number of inputs directly to distal apical tuft dendrites in the S-LM (Megias, Emri et al. 2001). These afferent inputs are thought to convey functionally distinct information streams, with medial entorhinal cortex carrying information from grid cells to distal dendrites and CA3 relaying input from upstream place cells to more proximal dendrites. The distinct morphologies and functional heterogeneity of inputs to these separate dendritic compartments suggests that the integration of different inputs and their influence on somatic output may heavily depend on the dendritic domain at which they arrive.

1.3 Mechanisms of Dendritic integration in CA1 neurons

Understanding how synaptic inputs are integrated and converted into action potential output is essential to understanding how the brain computes and stores information. CA1 hippocampal pyramidal neurons have been studied extensively for their proposed role in learning and memory processes and most of what is currently known about dendritic function stems from studies on these cells in brain slices. Dendrites have traditionally been viewed as passive structures which mainly serve to gather incoming synaptic input and transmit it to the soma to influence action potential firing. In vitro work in brain slices over the past few decades has challenged this view by demonstrating that dendrites express a variety of voltage- gated channels and thus, like axons, are highly electrically excitable structures that play an active role synaptic integration. These studies have shown that CA1 pyramidal cell dendrites are capable of different modes of integration based on their biophysical properties and the spatial and temporal arrangement of incoming synaptic inputs (Grienberger, Chen et al. 2015). Asynchronous or spatially distributed synaptic inputs arriving at the dendrites are integrated linearly to influence action potential generation, while synchronous and clustered inputs onto the same dendrite can sum supra-linearly through activation of voltage-gated channels to generate local dendritic spikes (Cash and Yuste 1999, Losonczy and Magee 2006). By locally amplifying synaptic signals, dendritic spikes boost the amount of synaptic input that directly reaches the soma and increase the impact that individual synaptic inputs have on neuronal output. This form of non-linear dendritic integration enables regenerative events to occur locally at the dendrites in addition to the soma and axon and is thought to enhance the computational and storage capacity of the cell

(Larkum and Nevian 2008). In these experiments dendritic integration is generally studied in brain slices by using two-photon uncaging of the caged compound MNI-Glu to mimic excitatory synaptic input onto CA1 dendrites while measuring changes in membrane potential induced by uncaging (gluEPSPs) at the soma (Losonczy and Magee 2006). Due to its high solubility, stability at physiological pH and light absorption properties, MNI-Glu was one of the first compounds to work well with 2-photon uncaging(Ellis-Davies 2018). Its development offered a means to optically mimic quantal glutamate release with great spatial and temporal precision and probe the mechanisms of dendritic integration with a level of control previously unavailable. In these experiments dendritic integration is quantified by comparing the somatic depolarization resulting from the synchronous activation of nearby synapses to the arithmetic sum of the individual excitatory post-synaptic potentials (uEPSPs) from the same synapses. Integration is deemed to be either linear or supra-linear depending on whether the observed response equals or exceeds the predicted arithmetic sum response (Gomez Gonzalez, Mel et al. 2011).

Using this technique, it was estimated that around ~6 spines must be activated (within a ~25 to 40 um distance) within a time period of <~6 milliseconds to evoke a local dendritic spike and that 6 evoked uEPSPs of 0.75 mV generate a somatic depolarization comparable to that of 25 uEPSPs of 0.25 mV. Any less synchronous input patterns will be summated linearly (Losonczy and Magee 2006). These local dendritic spikes are mediated by the activation of different channel types (Na^+, voltage-gated Ca^{2+}, and NMDA) and are distinct from back-propagating action potentials (APs) in that they occur in the absence of axonal APs and are for the most part functionally compartmentalized. These three types of dendritic spikes can influence AP output but in different capacities. Na^+channel mediated spikes are faster and narrower (<5 ms) than dendritic calcium and NMDA spikes and tend to fail as they propagate. While their direct influence on the soma is minimal their activation can relieve the Mg^{2+} block on NMDARs at the site of stimulation as well as activate voltage-gated calcium channels (VGCCs). Calcium and NMDA spikes on the other hand are slower and broader and as a result can trigger longer-lasting regenerative dendritic events called plateau potentials (Stuart and Spruston 2015). Studies in slice have shown that concurrent activity in CA3 and EC pathways can drive VGCC/NMDA receptor mediated plateau potentials in the distal dendrites of CA1 neurons leading to a high-frequency AP bursts of diminishing amplitude that coincide with global dendritic calcium spikes (Takahashi and Magee 2009, Bittner, Grienberger et al. 2015). Local NMDA spikes are generated through synchronous activation of a small number of nearby synapses on the same dendritic segment and require both the presence of glutamate as well as local depolarization of the membrane for their generation. While restricted in their spread, the resulting large amplitude and sustained depolarization they generate can amplify the effect of subsequent inputs and help to boost the amount of distal inputs that reach the soma by overcoming the strong attenuation experienced by these synaptic potentials as they propagate through the dendritic arbor. NMDA spikes can also modify dendritic excitability by potentiating the clustered inputs which participated in their generation through calcium dependent mechanisms(Schiller, Major et al. 2000) (Cichon and Gan 2015).

Although in vitro slice experiments have provided a wealth of information regarding the biophysical characteristics and computational capabilities of dendrites, it remains unclear whether the modes of synaptic integration observed in vitro substantially contribute to the encoding of behaviorally-relevant information in vivo. Currently, it is not possible to record the activity of dendrites and spines in behaving rodents using electrophysiology. For this reason, in vivo calcium imaging exists as one of the only techniques capable of probing the integrative properties of dendritic branches during behavior. Using this technique in the hippocampus it was shown that local dendritic calcium transients occur in the absence of detectable somatic activity in the basal dendrites of CA1 hippocampal place cells as an animal navigates an environment (Sheffield and Dombeck 2015). These dendritic calcium transients are confined to individual branches and are likely the result of local dendritically generated spikes (such as Na^+, NMDA and calcium spikes). Dendritic calcium transients were also found to commonly co-occur with somatic firing in place cells with the number of active branches varying between place field traversals. In contrast to the above work, a study using whole-cell recordings and dendritic calcium imaging of CA1 basal dendrites in anesthetized animals found no evidence of local dendritic calcium transients restricted to individual branches. Instead they found that the activation of NMDA receptors in basal CA1 dendrites can trigger large scale global dendritic calcium transients that invade the entire arbor and that these global calcium events were essential for the generation of complex spike bursts(Grienberger, Chen et al. 2014). These experiments suggest a role for regenerative dendritic events in determining CA1 firing in vivo but that branches may work alone or together depending on the cognitive state of the animal.

1.4 Synaptic Organization In Vivo

While the existence of local dendritic calcium transients suggests a role for non-linear dendritic integration of clustered inputs in CA1 neurons during behavior, how synaptic inputs are functionally organized throughout the dendritic arbor of CA1 place cells has never been directly measured and therefore remains unknown. Recent work has attempted to address the question of how synaptic input is organized onto dendritic branches in different brain areas by using calcium imaging to record sensory-evoked calcium transients from dendritic spines of mouse cortical neurons in vivo. These spine isolated calcium transients result from excitatory synaptic input and are thought to result mainly from calcium influx through NMDA receptors (Chen, Leischner et al. 2011, Chen, Wardill et al. 2013). These studies showed that in the visual cortex neighboring spines on the same dendritic branch were often tuned to different orientations of a moving visual stimulus and that spines sharing the same orientation preference were randomly distributed across the dendritic arbor (Chen, Wardill et al. 2013). Analogous studies in the auditory and barrel cortex reported similar findings indicating that synapses carrying similar sensory information are heterogeneously distributed across the dendritic tree (Chen, Leischner et al. 2011, Varga, Jia et al. 2011). However, a recent study using the same methods in the ferret visual cortex showed that nonlinearities resulting from the functional clustering of synaptic inputs within the dendritic tree are important for shaping orientation selectivity in layer 2/3 neurons (Wilson, Whitney et al. 2016). Additionally, an anatomical study using a technique to specifically label only sites of synaptic contact between presynaptic CA3 and postsynaptic CA1 pyramidal neurons showed that inputs on specific branches were significantly more clustered than expected by chance (Druckmann, Feng et al. 2014). As these studies provide evidence both for and against functional clustering of synaptic inputs in vivo, the predominant mode by which synaptic inputs are integrated in the intact brain remains unsettled.

1.5 Models of Place Field Formation

Localizing one’s position relative to their surrounding environment depends on the activity of place cells in the hippocampus. Each place cell is active at a specific location in the environment and through their ensemble activity form a cognitive map of the outside world. These cells receive thousands of synaptic inputs from upstream spatially tuned neurons, but how CA1 place cells integrate and respond to these inputs to form their spatially selective firing fields remains unknown. The two main models proposed to underlie the formation of CA1 place are through a linear combination of differently spaced grid cell inputs and various mechanisms of Hebbian synaptic plasticity. As the main source of excitatory drive from cortical regions, grid cell input was initially viewed as the primary determinant of place cell firing and prominently featured into many of the models predicting how place fields are generated. These models proposed that hippocampal place fields arise through the linear summation of inputs from grid cells with overlapping firing fields of variable spacing and orientation(Burgess and O'Keefe 1996, McNaughton, Battaglia et al. 2006, Solstad, Moser et al. 2006). Subsequent research in pre-weanling rats challenged this view of grid cells as the primary source of place fields by showing that stable place fields emerged several weeks before grid firing patterns stabilized (Langston, Ainge et al. 2010, Wills, Cacucci et al. 2010). If grid cell activity was mostly responsible for the generation of place fields, stable grid fields would be expected to appear prior to or simultaneously with that of place fields rather than afterwards in the developing animal.

When a rat is placed into a novel environment, some cells showed stable place fields immediately (Hill 1978, Frank, Stanley et al. 2004) while others took several minutes of exploration before developing a stable field (Wilson and McNaughton 1993, Frank, Stanley et al. 2004). These results suggest that multiple mechanisms may contribute to the formation of place fields, and at least a subset of cells may undergo activity-dependent Hebbian synaptic plasticity during spatial encoding. Support for this comes from studies showing that pharmacological blockade of NMDA receptors alters place field stability (Kentros, Hargreaves et al. 1998) and inhibits the asymmetric backward shift in fields (Ekstrom, Meltzer et al. 2001) thought to depend on experience-dependent long-term synaptic plasticity (Mehta, Quirk et al. 2000). While directly assessing the connection between hippocampal plasticity and place field formation in awake animals remains a difficult undertaking, recent work points to a role for active dendritic mechanisms in the formation of place fields. Using whole-cell recordings from CA1 neurons in head-restrained mice navigating a fabric treadmill, it was shown that place fields can be formed at any location on the track by artificially inducing plateau potentials through current injection, and that trains of APs by themselves are insufficient to evoke stable fields. These fields remained stable on subsequent laps after the initial induction protocol due to the likely strengthening of synaptic inputs coincident with plateau generation (Bittner, Grienberger et al. 2015). This suggests that CA1 cells receives significant input at every location along the track and implies that it is the potentiation of specific subsets of inputs by plateau potentials rather than an increase in the number of inputs at a specific location which determines a place fields' firing location. This enables CA1 cells to express location-specific firing at any position and implicates a strong role for active dendritic plasticity mechanisms in the generation of CA1 place fields. Recent work from our lab using calcium imaging supports this by showing that regenerative dendritic events can occur in place cells and their prevalence predicts place field stability and precision though this was in an already familiar environment(Sheffield and Dombeck 2015). In addition to the global dendritic events which commonly co-occurred with somatic firing, local dendritic calcium transients which occurred in the absence of detectable somatic activity were also found in place cells. These dendritic calcium transients were confined to individual branches and are thought to result from coincident synaptic activation and calcium influx through NMDA receptors. Local NMDA spikes can potentiate subsets of co-activated neighboring inputs thereby enhancing the effect of these inputs on neuronal output. These local dendritically generated spikes can also induce long-term changes in dendritic excitability, lowering the threshold for future spike generation and enhancing spike propagation (Frick, Magee et al. 2004, Xu, Kang et al. 2005, Losonczy, Makara et al. 2008). Thus, local dendritic NMDA spikes may contribute to natural place field formation in novel environments either in coordination with or complimentary to mechanisms of dendritic plateau potentials.

1.6 Thesis Overview

In my thesis I have conducted experiments to explore the role of dendritic integration and local dendritic spiking in place field formation and maintenance by imaging dendritic activity and the patterns of synaptic input to hippocampal place cells during navigation behavior using in vivo two-photon imaging of calcium and glutamate transients. I then used two-photon glutamate uncaging and in vitro whole-cell recordings to characterize the origin of the dendritic calcium and glutamate transients observed in vivo and explore the detection efficiency of our in vivo imaging method. In collaboration with Mark Sheffield, a post-doctoral fellow in the lab, I first examined whether branch spiking events occur during natural place field formation in novel environments and how their emergence correlates with the somatic place field location. These experiments, detailed in *Chapter 2*, lay the groundwork for the experiments conducted in *Chapter 4* in which I explore the relationship between the functional and anatomical organization of inputs onto CA1 place cell dendrites and the spatial location of the somatic place field. Details regarding the technical difficulties and various methodologies used to complete these experiments are described in *Chapter 3*. In these experiments I addressed several prominent questions in the field such as: What type of information do CA1 pyramidal neurons receive during awake behavior e.g., do inputs exhibit spatial tuning? Is this tuning localized to specific track positions or evenly distributed across space? How is this input anatomically organized along the dendrite e.g., clustered in space and time or randomly distributed? What is relationship between the tuning of inputs and the spatial tuning of the somatic field? What is the relationship between the functional and anatomical organization of inputs onto the dendrite and the spatial location of the somatic place field e.g., are inputs that are clustered in anatomical dendritic space also clustered in space on the track at the cell's place field? The findings from these two studies imply that regenerative dendritic events and super-linear dendritic summation contribute to the formation and maintenance of CA1 place fields and provide support for a new model in which an increased number of synapses from presynaptic neurons with the same field form functional clusters onto CA1 neuron dendrites to drive place specific firing.

Chapter 2: Increased prevalence of calcium transients across the dendritic arbor during place field formation

2.1 Summary

Hippocampal place cell ensembles form a cognitive map of space during exposure to novel environments. However, surprisingly little evidence exists to support the idea that synaptic plasticity in place cells is involved in forming new place fields. Here we used high-resolution functional imaging to determine the signaling patterns in CA1 soma, dendrites and axons associated with place field formation when mice are exposed to novel virtual environments. We found that putative local dendritic spikes often occur prior to somatic place field firing. Subsequently, the first occurrence of somatic place field firing was associated with widespread regenerative dendritic events, which decreased in prevalence with increased novel environment experience. This transient increase in regenerative events was likely facilitated by a reduction in dendritic inhibition. Since regenerative dendritic events can provide the depolarization necessary for Hebbian potentiation, these results suggest that activity dependent synaptic plasticity underlies the formation of many CA1 place fields.

2.2 Introduction

The hippocampus is critical for the formation and storage of spatial memories (Morris, Garrud et al. 1982, Teng and Squire 1999). Hippocampal place cells not only fire when animal’s move through a particular location (place field)(O'Keefe and Dostrovsky 1971), but during sleep and rest subsequent to the experience they can reactivate in the same (or reverse) sequence as during the experience (Wilson and McNaughton 1994, Foster and Wilson 2006, Carr, Jadhav et al. 2011, Sadowski, Jones et al. 2016, van de Ven, Trouche et al. 2016). This has led to the idea that place cell ensembles represent a cognitive map of space and a memory of places.

Hippocampal pyramidal neurons, which are the cells that form place fields during spatial navigation, are capable of engaging activity dependent Hebbian synaptic plasticity (Bliss and Collingridge 1993), a potential mechanism by which spatial information can be encoded and stored. Indeed, disruption of components of the molecular pathways involved in synaptic plasticity, such as NMDA receptors or CaMKII, is correlated with behavioral deficits in memory or spatial navigation tasks (Morris, Anderson et al. 1986, Silva, Paylor et al. 1992, Tsien, Huerta et al. 1996). Given that ensembles of place fields are thought to represent spatial memories and are likely used for spatial navigation, these findings have led to the hypothesis that place fields may form *de novo* through activity dependent synaptic plasticity (Takeuchi, Duszkiewicz et al. 2014), with some evidence supporting this view (Monaco, Rao et al. 2014, Bittner, Grienberger et al. 2015). However, there is significant evidence supporting an alternative view, that synaptic plasticity may not be required for place field formation (Hill 1978, McHugh, Blum et al. 1996, Kentros, Hargreaves et al. 1998, Frank, Stanley et al. 2004, Cacucci, Wills et al. 2007, Dragoi and Tonegawa 2011, Dragoi and Tonegawa 2013). For example, after hippocampal synaptic plasticity is perturbed or blocked, place fields are typically less precise (McHugh, Blum et al. 1996, Rotenberg, Mayford et al. 1996, Kentros, Hargreaves et al. 1998, Cacucci, Wills et al. 2007), less stable (Rotenberg, Mayford et al. 1996, Kentros, Hargreaves et al. 1998) and fail to shift backward (Ekstrom, Meltzer et al. 2001), but nonetheless place fields still form. Additionally, many place fields are immediately present upon the animal's first traversal across a novel environment (Hill 1978, Frank, Stanley et al. 2004). Such a rapidly appearing cognitive map suggests that hippocampal representations could arise through the novel stimulus dependent selection of pre-strengthened neuronal ensembles (Deguchi, Donato et al. 2011, Dragoi and Tonegawa 2011, Lee, Lin et al. 2012, Dragoi and Tonegawa 2013, Dragoi and Tonegawa 2014).

These results call into question the idea that place fields form *de novo* through synaptic plasticity during experience of a novel environment.

It has been difficult to assess directly the involvement of synaptic plasticity in awake animals engaged in navigation tasks. One step towards this goal would be to investigate dendritic regenerative events (back propagating action potentials or dendritically generated spikes, here collectively referred to as branch spikes (Sheffield and Dombeck 2015)), which are thought to provide the post-synaptic depolarization necessary for Hebbian potentiation when paired with presynaptic input (Magee and Johnston 1997, Schiller, Schiller et al. 1998, Golding, Staff et al. 2002). Measuring the occurrence of branch spikes during place field formation would therefore indicate periods in which Hebbian synaptic potentiation could be occurring. A recent study used somatically recorded plateau potentials to infer the existence of branch spiking events throughout the arbor and found that such events may underlie the formation of both artificially induced and spontaneously appearing place fields in familiar environments (Bittner, Grienberger et al. 2015). The technology now exists to record branch spiking directly in behaving mice and, in fact, these events have recently been detected in hippocampal place cells, though again these observations were made during navigation in familiar environments (Sheffield and Dombeck 2015). This previous research (Sheffield and Dombeck 2015) demonstrated that branch spiking and somatic firing are often dissociated in place cells, meaning that somatic firing does not provide a direct read out of branch spiking across the arbor. Thus, while there is now evidence to support the idea that branch spiking occurs in place cells and is likely capable of inducing plasticity which can lead to place field firing in familiar environments, it remains unclear whether branch spiking events occur during, or lead to, natural place field formation in novel environments.

Here we used virtual reality (VR) combined with two-photon functional imaging to either monitor large populations of hippocampal CA1 neuron somata, co-record CA1 neuron dendrites and somata or record CA1 interneuron axons while mice were rapidly exposed to novel virtual environments. Global remapping occurred during this paradigm and was similar to that described in real world environments (Muller and Kubie 1987, Bostock, Muller et al. 1991, Leutgeb, Leutgeb et al. 2004, Leutgeb, Leutgeb et al. 2005, Fyhn, Hafting et al. 2007), allowing us to continuously monitor the remapping process from the first moments of novel environment exposure. We found that regenerative dendritic events occur during the first appearance of somatic place field firing and during the first several novel environment traversals the prevalence of these events was increased across the arbor compared to familiar environments or later traversals in the novel environment. For some place fields, localized regenerative dendritic events preceded the appearance of detectable somatic place field firing and predicted the location of the later forming somatic place field. Additionally, we found a transient reduction in the magnitude of calcium transients in the axons of dendrite targeting interneurons on the first few laps in novel environments, while a brief increase in the magnitude of calcium transients in the axons of somatic targeting interneurons was found during a similar period. Finally, we found that when functional NMDA receptors are knocked out in CA1 neurons, the number of place fields that form across the population is reduced by ~50%. These results suggest that exposure to a novel environment is accompanied by a short time window of reduced dendritic inhibition in CA1, which leads to increased branch spiking, which may potentiate synapses in a subset of neurons to form new place fields. Together these results support the idea that activity dependent synaptic plasticity underlies the formation of a subset of CA1 place fields in the hippocampus during novel environment exposure.

2.3 Results

2.3.1 Novel virtual environment exposure leads to global remapping in the hippocampus in head restrained mice

We used VR to implement an environment switch paradigm to induce hippocampal global remapping in head-restrained mice (Figure 2.1, Figure 2.2). Mice were trained once a day for 7 days on a 1D treadmill to traverse a 3 m virtual visual linear track (Figure 2.2A, Figure 2.11A, B) for water rewards (Heys, Rangarajan et al. 2014). Subsequently, on experimental day 1, mice traversed this familiar environment (F) for at least 15 laps before F was rapidly (~30 ms) switched to a novel environment (N; Figure 2.2A, Figure 2.1A, B). Mice then experienced N for at least 20 laps, before being placed back in their home cage. The following day (experimental day 2) the mice were re-exposed to N where they traversed the track for at least 20 laps. An F-to-N switch was implemented twice for each mouse, with different environments for each switch (Figure 2.1A, B). To quantify behavior before, during, and after the switch, we measured mean lap velocity (Figure 2.2B2), stopping probability (Figure 2.1D) and mean stopping time (Figure 2.1E) on each lap. We found the first lap in N was traversed slower (15.6 ± 1.5 cm$_{-s}$ SEM on first lap in N vs. 27.7 ± 0.5 cm$_{-s}$ SEM in F, $p < 0.001$, Paired t-test , $n = 32$ sessions, $n = 16$ mice) and with more stops (0.8 ± 0.1 SEM on first lap in N vs. 0.19 ± 0.02 SEM in F, $p < 0.01$) that lasted longer (5.4 ± 2.1 s SEM on first lap in N vs. 0.63 ± 0.13 s SEM in F, $p < 0.001$) compared to F, but behavior quickly stabilized such that on all subsequent laps in N, mean lap velocity and mean stopping time were not different compared to F (mean lap velocity from all laps and excluding lap 1 in N: 27.7 ± 0.5 cm$_{-s}$ in F vs. 27.7 ± 0.5 cm$_{-s}$ in N, $p > 0.05$, Paired t-test; mean lap stopping time from all laps following lap 1: 0.63 ± 0.13 s SEM in F vs. 1.04 ± 0.25 s SEM in N, $p > 0.05$), and mean stopping probability was only slightly increased (mean lap stopping probability from all laps following lap 1: 0.19 ± 0.02 in F vs. 0.30 ± 0.02 SEM in N, $p < 0.001$, Paired t-test). Therefore, our VR paradigm allows for rapid switching from familiar to novel environments with relatively little change in behavior after the first traversal.

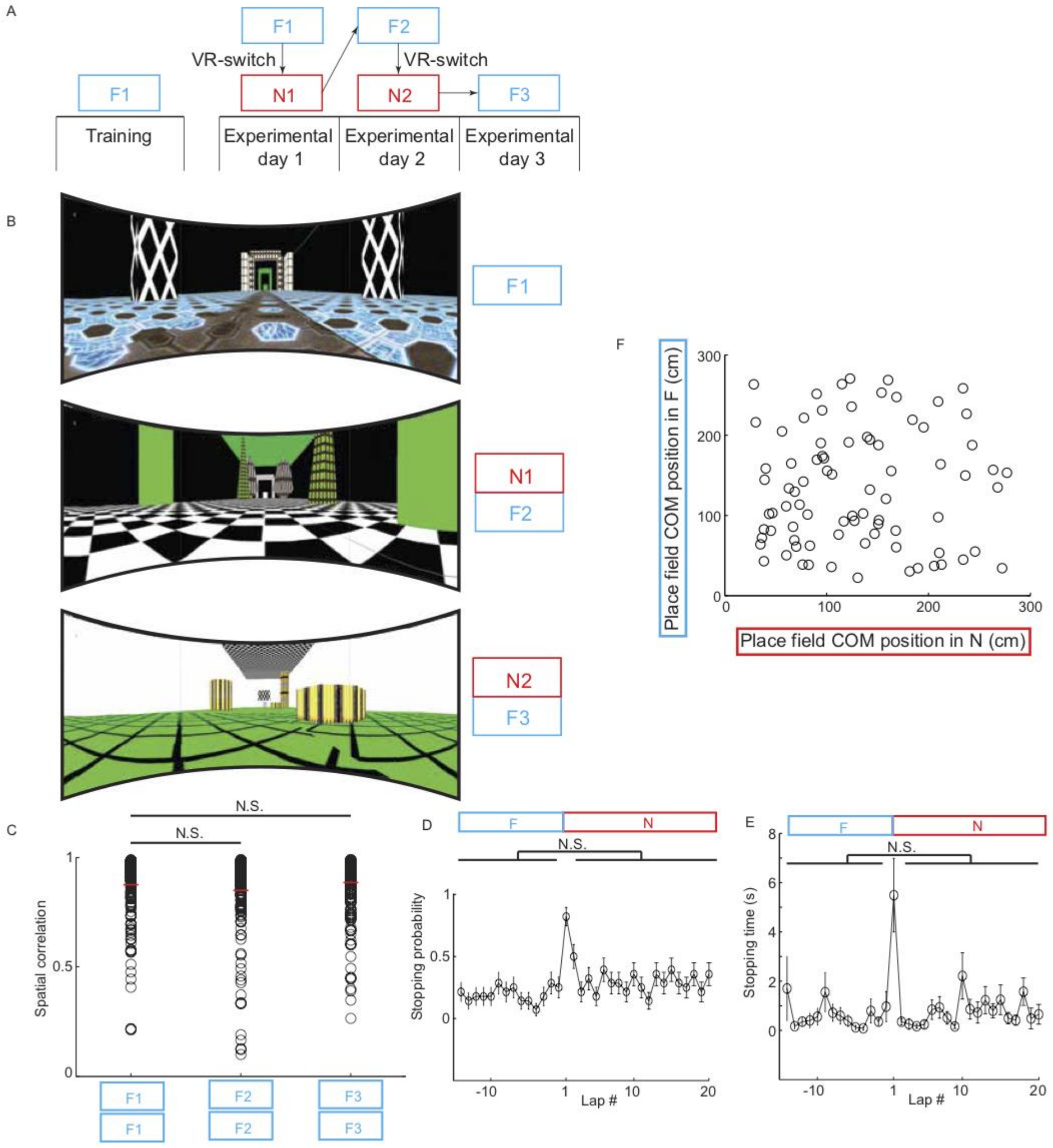

i Figure 2.1: Experimental timeline and place field spatial correlations in different virtual environments

(A) Schematic of experimental timeline. Training in F1 occurred over ~7 days. Imaging occurred on experimental day 1-3. Note, N1 and F2 are the same virtual environment as are N2 and F3.

(B) The three virtual environments used.

(C) Place field spatial correlation between first half and second half of sessions is not significantly different within F1 vs. within F2 or F3 (n = 4 mice, n = 4 sessions in each environment; unpaired t-test, $p > 0.05$).

(D) Stopping probability is higher on the first lap in N compared to F (Paired t-test, $p < 0.01$), but is only slightly above F levels from lap 2 onwards (Paired t-test, $p < 0.05$).

(E) Stopping time is significantly higher on the first lap in N compared to F (Paired t-test, $p < 0.001$), but matches F from lap 2 onwards (Paired t-test, $p > 0.05$).

(F) Plot of place field center of mass (COM) location in F vs N for the 81 cells that had place fields in both F and N (n = 4 mice, n = 8 environment switches from F to N). Each circle represents one place cell.

We then asked whether the switch from F to N caused global remapping in the hippocampus, a phenomenon that occurs in the real world when animals are placed in novel environments (Muller and Kubie 1987, Bostock, Muller et al. 1991, Leutgeb, Leutgeb et al. 2004, Leutgeb, Leutgeb et al. 2005, Fyhn, Hafting et al. 2007). We used our previously described methods to optically record somatic calcium transients (a measure of action potential firing; GCaMP6f) in populations of CA1 pyramidal neurons and defined the place firing field(s) of neurons within the population (Dombeck, Harvey et al. 2010, Sheffield and Dombeck 2015). Over all traversals in F, we found all neurons with significant mean place fields. From 8 sessions in F (n = 4 mice) we identified 347 place cells. Some place cells expressed 2 place fields, and we treated each place field independently (382 place fields total). A typical CA1 field of view contained place cells (Figure 2.2C bottom left) expressing place fields tiling the track (Figure 2.2C top left). We then switched from F to N and measured the firing patterns of the *same* neurons (the place cells that had place fields in F; Figure 2.2C bottom middle) over all traversals in N on experimental day 1 (Figure 2.2C top middle). We found that, across all mice, many cells identified as having place fields in F did not have place fields in N (301/382 place fields). For the cells that did have place fields in both F and N, the location of the fields were not correlated (see methods, Figure 2.1F) and showed significantly less spatial correlation compared to fields examined within F (Figure 2.2D, spatial correlation within first ½ to second ½ of F = 0.87 ± 0.01 SEM, n = 382 place fields vs. across F to N = 0.06 ± 0.04 SEM, n = 81 place fields, $p < 0.001$, unpaired t-test). However, additional place cells appeared in N (n = 263 total place cells; n = 279 total place fields across all mice; Figure 2.2C bottom right) and their place fields tiled the novel track (Figure 2.2C top right). These data are consistent with global remapping in real world environments (Muller and Kubie 1987, Bostock, Muller et al. 1991, Leutgeb, Leutgeb et al. 2004, Leutgeb, Leutgeb et al. 2005, Fyhn, Hafting et al. 2007) and in VR in body-tethered rats (Aronov and Tank 2014), and indicate that global remapping occurs in the hippocampus of head-restrained mice following a rapid switch from a familiar to a novel VR environment.

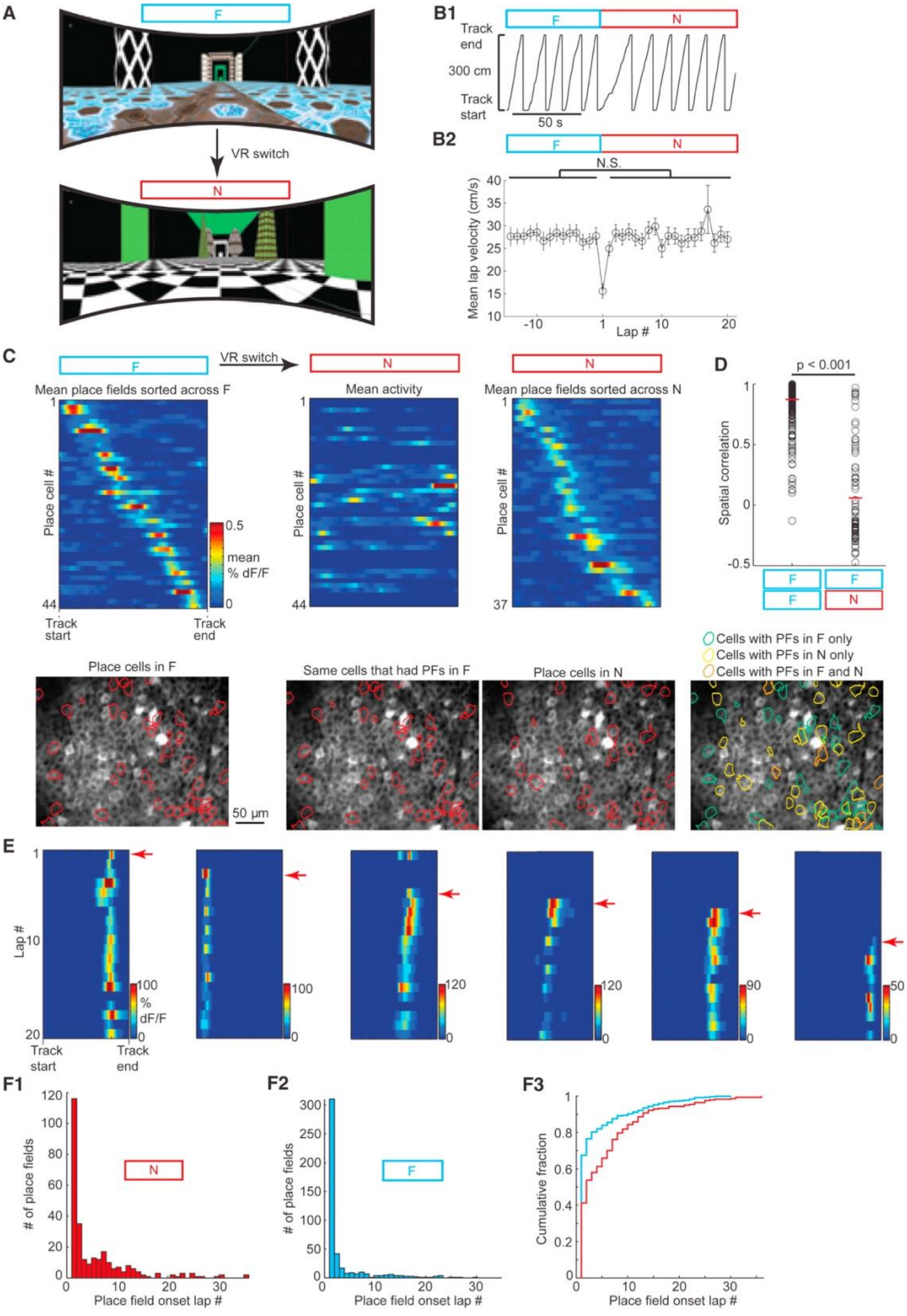
A
F
VR switch
N
B1
F
N
Track end
300 cm
Track start
50 s
B2
F
N
N.S.
Mean lap velocity (cm/s)
40
35
30
25
20
15
10
-10
1
10
20
Lap #
C
F
VR switch
N
N
Mean place fields sorted across F
Mean activity
Mean place fields sorted across N
Place cell #
1
44
0.5
mean % dF/F
0
Track start
Track end
1
44
1
37
D
p < 0.001
Spatial correlation
1
0.5
0
-0.5
F
F
F
N
Cells with PFs in F only
Cells with PFs in N only
Cells with PFs in F and N
Place cells in F
50 µm
Same cells that had PFs in F
Place cells in N
E
Lap #
1
10
20
100
% dF/F
0
Track start
Track end
100
0
120
0
120
0
90
0
50
0
F1
# of place fields
120
100
80
60
40
20
0
N
0
10
20
30
Place field onset lap #
F2
# of place fields
300
250
200
150
100
50
0
F
0
10
20
30
Place field onset lap #
F3
Cumulative fraction
1
0.8
0.6
0.4
0.2
0
0
10
20
30
Place field onset lap #

ii Figure 2.2: Switching virtual environments causes global remapping

(A) Examples of familiar (F) and novel (N) virtual environments.

(B1) Single mouse behavior showing track position vs time over F to N switch.

(B2) Summary across all mice of mean lap velocity over F to N switch (n = 16 mice; n = 32 F to N switches). Mean ± SEM; N.S. Paired t-test, $p > 0.05$.

(C) Bottom left: CA1 field of view indicating place cells encoding F (red). Top left: Mean place fields from cells (red) sorted by track position. Bottom middle: Same field of view and cells as in bottom left. Top middle: Mean activity of indicated cells in N sorted in same order as Top left. Bottom right: Same field of view as Bottom left with all place cells encoding N (red). Top right: Mean place fields from cells (red) sorted by track position. Bottom far right: Same field of view as Bottom left with all place cells colored to indicate F, N or both encoding.

(D) Place field spatial correlation within F vs. across F-to-N. $p < 0.001$, unpaired t-test.

(E) Somatic place field transients shown lap by lap in N for 6 example cells; first row represents first traversal mouse ever made across N. Red arrows indicate place field onset lap.

(F1 and F2) Histograms of place field onset lap number from all mice in N (F1; n = 4 mice; n = 8 sessions in N) and F (F2; n = 3 mice; n = 8 session in F).

(F3) Cumulative fraction plots of the data in F1 and F2**.** Place field onset lap distribution was shifted (Wilcoxon rank sum test, $P < 0.001$) such that place fields appeared earlier in F vs N.

Next, we tracked somatic calcium transients of the place fields that appeared in N on each lap starting from the very first lap in N (Figure 2.2E). We noticed that place fields abruptly appeared on a range of laps during the initial exposure to N (Figure 2.2E), an observation also consistent with remapping in real-world novel environments (Hill 1978, Frank, Stanley et al.

2004). To quantify this, for each place field detected in N, we identified the lap in which transients first began to robustly occur within the place field (place field onset lap; Figure 2.2E, red arrows; see methods). Pooling the place fields from all mice (n = 4 mice, n = 8 sessions in N), we found that 116/279 place fields appeared on the first lap in N, 35/279 had a place field onset lap of 2; and 128/279 had a place field onset lap greater than lap 2 (Figure 2.2F1; a different distribution compared to the same measurements in F, see Figure 2.2F2, F3). Overall, the vast majority of place fields appeared within the first several laps of N (224/279 (80%) within 8 laps and 261/279 (94%) within 16 laps; 92.3 ± 2.4 s SEM and 179.5 ± 3.2 s SEM was required to complete 8 and 16 laps respectively). These results demonstrate that exposure to novel environments leads to the appearance of place fields over the first few traversals and minutes.

2.3.2 Prevalence of dendritic branch spikes is increased in place cells during initial exposure to novel environments and predicts final place field location

To test whether synaptic plasticity could occur during the initial exposure to N, when the majority of place fields first appear, we asked if branch spiking (Sheffield and Dombeck 2015), which can provide the post-synaptic depolarization necessary for Hebbian synaptic potentiation (Magee and Johnston 1997, Schiller, Schiller et al. 1998, Golding, Staff et al. 2002), occurred or varied during this period. We sparsely labeled CA1 neurons with GCaMP6f (Figure 2.3A) and used multi-plane 2-photon imaging to co-acquire time-series datasets from CA1 basal dendrites and their parent somata (n = 9 mice, n = 18 sessions in N; n = 13 place cells; n = 17 place fields; number of dendrites imaged per cell: range = 9-36, mean = 17 ± 2; distance of dendritic imaging plane from somatic imaging plane: range = 61-103 µm, mean = 83 ± 8 µm (distal tips located in a plane ~120 μm from somata)) (Sheffield and Dombeck 2015). Individual dendrites were assigned to their parent somata offline using dendrite tracing from a z-series image stack (Sheffield and Dombeck, 2015; Methods). To quantify the prevalence of branch spiking over traversals in N, we calculated the branch spike prevalence (BSP) as the fraction of recorded branches from each cell with branch spikes during each traversal across the place field when somatic firing was detected (Figure 2.3B) (Sheffield and Dombeck 2015). We first observed that branch spiking was always associated with place field formation: branch spiking in the basal dendrites always occurred and was typically widespread during the first detectable somatic firing events in the place field (n = 17 place fields with branch spikes, mean BSP = 0.80 ± 0.07 SEM, range: 0.20 - 1.00 during first somatic firing in field; n = 11 place fields with BSP > 0.96 and n = 4 with BSP < 0.45; Figure 2.3A,B). During this first traversal and the following traversals across the place field in which somatic firing was detected, we observed variations in BSP from traversal to traversal (Figure 2.3A,B). For individual place cells, we noticed that the average BSP (binned over 4 laps) was nearly always elevated when the somatic place field first appeared during the initial exposure to N, and decreased with lap number during the session (Figure 2.3B right). This effect was significant on average across all place cells from all mice exposed to N (Figure 2.3C), and importantly did not occur at the beginning of sessions when mice were first exposed to F (Figure 2.4I, J). We measured average BSP from place cells in F (mean BSP = 0.43 ± 0.03 SEM), which was significantly lower than the average BSP that occurred during laps 1-4 in N (mean BSP = 0.75 ± 0.08 SEM, $p < 0.01$, unpaired t-test), laps 5-8 in N (mean BSP = 0.65 ± 0.07 SEM, $p < 0.05$, unpaired t-test; Figure 2.3C) and the first 4 laps from place field onset (mean BSP = 0.66 ± 0.05 SEM, $p < 0.01$, unpaired t-test; Figure 2.3F). We also compared average BSP during the first 8 (Figure 2.3D) or 16 laps (Figure 2.3E) in N to later laps in N (>

lap 16) in the same cells, and found average BSP was significantly higher early versus late in both cases (mean BSP from all laps following lap 16 = 0.38 ± 0.04 SEM vs. laps 1-8 = 0.69 ± 0.05 SEM, $p < 0.01$, Paired t-test, and vs. laps 1-16 = 0.62 ± 0.04 SEM, $p < 0.01$ Paired t-test). Again, these changes in BSP as a function of lap number were not seen in F (Figure 2.4J).

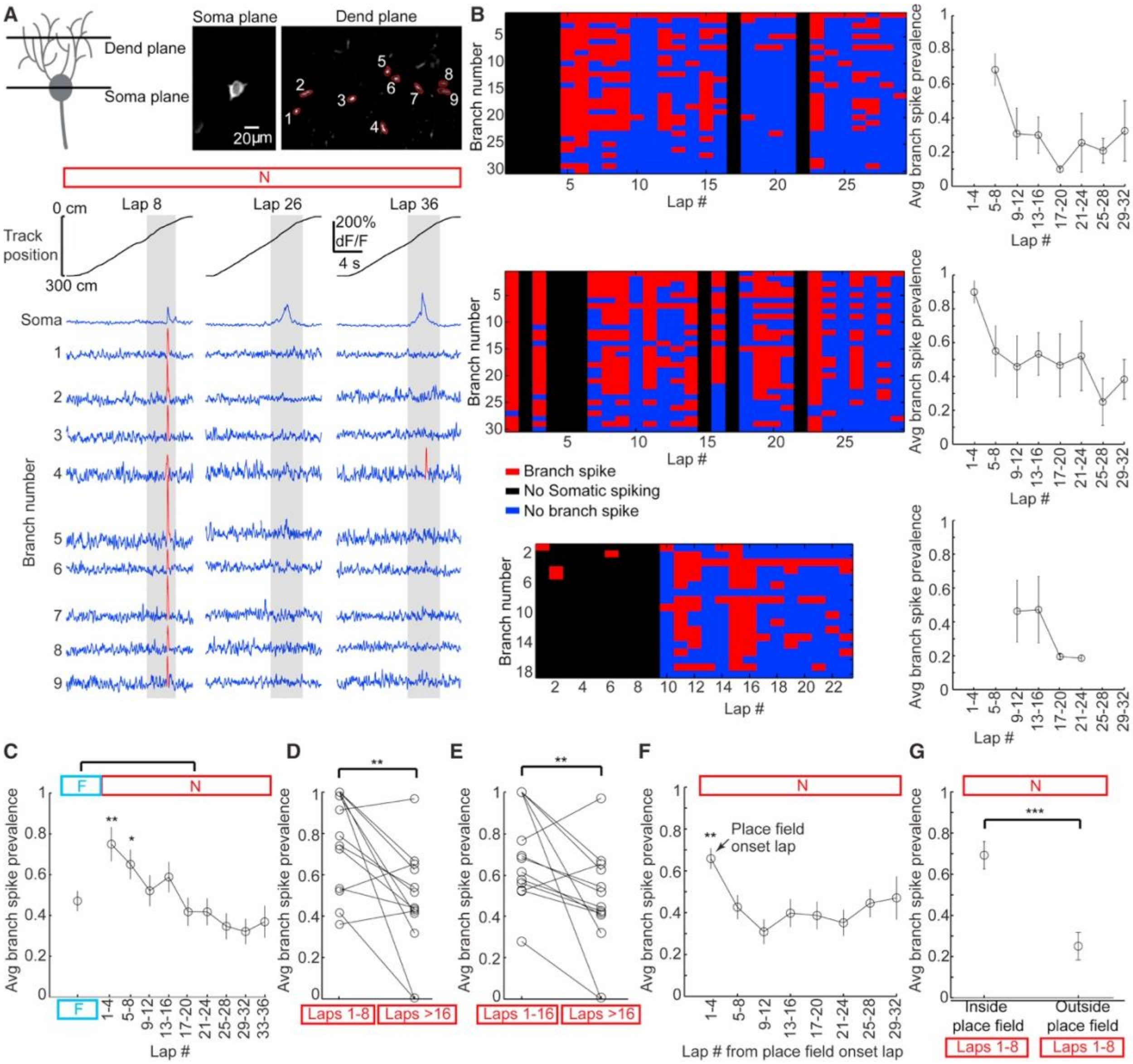

iii Figure 2.3: Dendritic branch spikes are more prevalent during initial exposure to novel environments and predict future place field location.

(A) Top, Cartoon depicting 2-photon imaging planes in the soma and basal dendrites of pyramidal cells and co-acquired images of place cell soma and dendrites from the same cell. Bottom, $\Delta F/F$ traces from the (co-acquired) soma and numbered dendritic branches during 3 place field traversals (grey columns, mean place field over session in N) in N. Red traces, transients of $P < 0.001$ from bootstrapping.

(B) Colored plots (left; three different place cells from two mice) show occurrence of detectable branch spiking in each imaged branch (rows) in the somatic place field on each lap in N, each column represents a different lap in N; first column represents first traversal mouse ever made across N. Red, significant transient in the imaged branch; blue, no significant transient in the branch during a co-occurring somatic calcium transient; black, no significant transient in the branch or soma. Right, plots of mean BSP (4 laps binned) vs laps in N from example cells on left.

(C) Summary across all mice of mean BSP in F (n = 10 place fields, n = 5 mice) and N (4 laps binned; n = 18 place fields, n = 9 mice).

(D) Mean BSP from first 8 laps vs all laps following lap 16 in N (n = 13 place fields, n = 7 mice). **, Paired t-test, $p < 0.01$.

(E) Same as D but using first 16 laps. **, Paired t-test, $p < 0.01$.

(F) Same as (C) but aligned to place field onset lap for each cell (depicted as lap 1).

(G) Average BSP in place fields versus outside of place fields in first 8 laps of N. ***,Paired t-test, $p < 0.001$.

Since dendritic branch spiking and somatic firing can be dissociated in CA1 place cells (Sheffield and Dombeck 2015), we next asked whether the location of branch spiking on the track during initial exposure to N was an indicator of where the mean place field would be located at the end of the session. We determined the track location of the mean somatic place field calculated from laps in the last half of the session in N. We then measured the average BSP that occurred within this location and compared it to the average BSP outside this location (fraction of branches with branch spikes during somatic firing detected outside of place field) during the first 8 laps of the session in N. We found that average BSP in the first 8 laps was significantly higher within the final place field location versus outside of this location, predicting the final field location (Figure 2.3G, average BSP inside = 0.67 ± 0.07 SEM, outside = 0.25 ± 0.07 SEM, Paired t-test, $p < 0.001$). Together, the above findings demonstrate that branch spiking in basal dendrites is elevated during somatic place field firing in the first several traversals of a novel environment, and is most prevalent at the track location of the final place field. These results support the idea that synaptic plasticity is taking place during a window in which place fields first appear in novel environments.

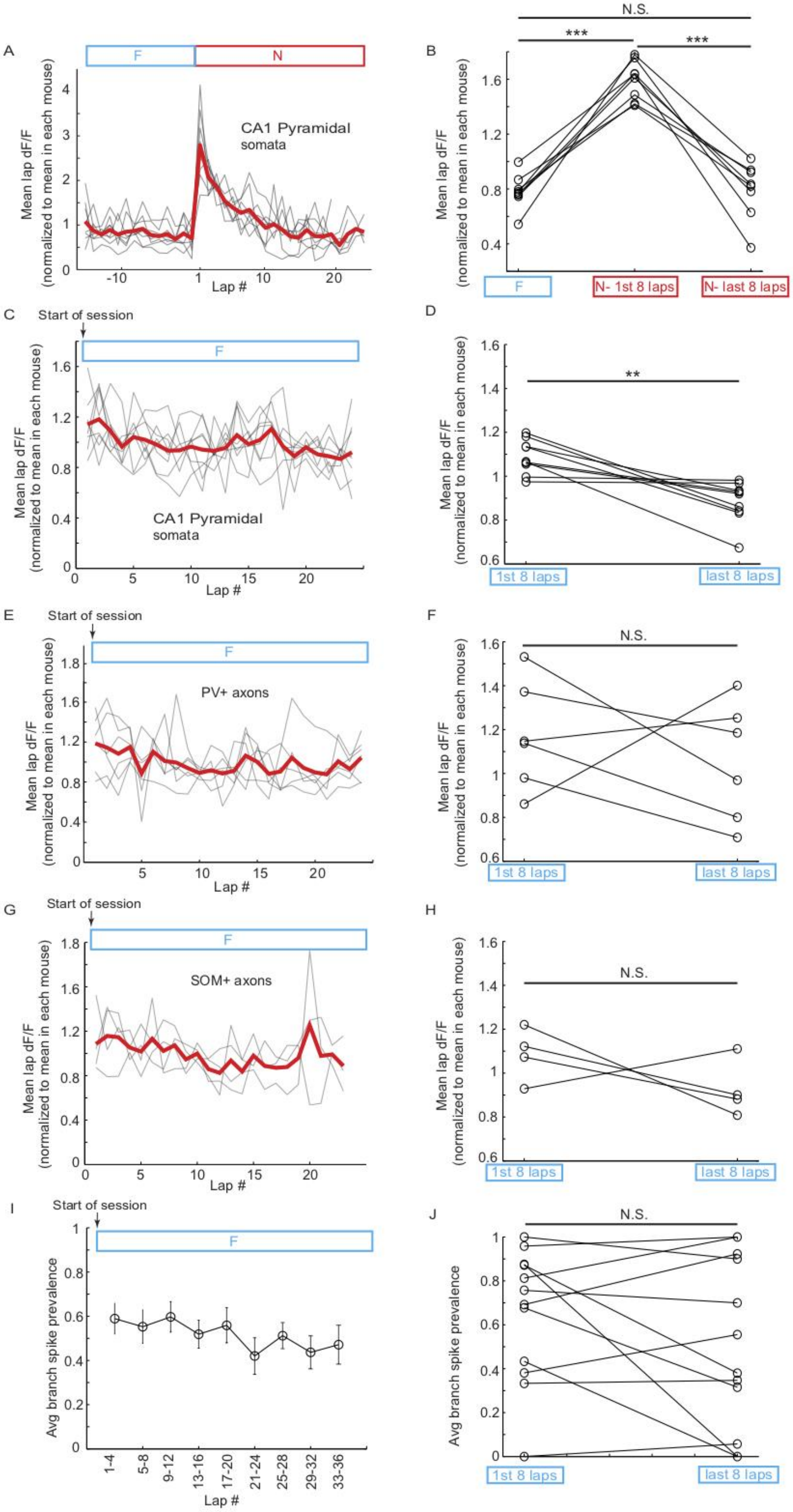
A
F
N
CA1 Pyramidal
somata
Mean lap dF/F
(normalized to mean in each mouse)
Lap #
-10
1
10
20
B
N.S.
***
***
F
N- 1st 8 laps
N- last 8 laps
C
Start of session
F
CA1 Pyramidal
somata
D
**
1st 8 laps
last 8 laps
E
Start of session
PV+ axons
F
N.S.
G
Start of session
SOM+ axons
H
N.S.
I
Start of session
Avg branch spike prevalence
1-4
5-8
9-12
13-16
17-20
21-24
25-28
29-32
33-36
Lap #
J
N.S.
1st 8 laps
last 8 laps

iv Figure 2.4: The changes in calcium signaling observed upon first exposure to novel environments do not occur upon re-exposure to familiar environments

(A) Mean somatic ΔF/F on each lap (normalized to the mean in each case) in F and N from CA1 pyramidal neuron populations ($n = 8$ environment switches from F to N; $n = 4$ mice; all active cells included). The mean from all mice is shown in red.

(B) Normalized Mean somatic ΔF/F in F, and the first and last 8 laps in N in CA1 pyramidal neurons. Open circles represent each environment switch from F to N ($n = 8$ from $n = 4$ mice; all active cells included). Mean lap ΔF/F is significantly larger during the first 8 laps in N compared to F (Repeated measures ANOVA with Tukey's post-test, $p < 0.001$), but returns to F levels during the last 8 laps in N ($p > 0.05$, Repeated measures ANOVA with Tukey's post-test).

(C – H) Mean dF/F (normalized to mean in each mouse) from the start of the session in F on each lap (left plots; lap 1 is first traversal of mouse across the familiar environment F on the given day; individual mice shown in gray, mean from all mice shown in red) or mean from first 8 and last 8 laps in F (right plots) of CA1 pyramidal cell somata (C and D; all active cells included), PV+ axons in pyramidal cell layer (E and F; dF/F calculated during running) and SOM+ axons in Stratum Oriens (G and H; dF/F calculated during running). Comparing mean dF/F from the first 8 to the last 8 laps revealed no significant difference in PV+ and SOM+ axons ($p > 0.05$, Paired t-test) and a slight decrease in CA1 pyramidal cell somata ($p < 0.01$, Paired t-test).

(I) Summary plot across all mice of mean branch spike prevalence (BSP) in F ($n = 14$ place fields from $n = 7$ mice; 4 laps binned; lap 1 is first traversal of mouse across the familiar environment F on the given day).

(J) Mean BSP from the first 8 laps in F ($n = 12$ place fields from $n = 6$ mice) in each place field is not significantly different from the last 8 laps (Paired t-test, $p > 0.05$). Note that some place fields did not have any somatic calcium transients in their place field in the first 8 laps and thus were not included.

2.3.3 Dendrite-localized calcium transients predict the track location of subsequent delayed onset place fields

As described above (Fig 2.1E and 2.1F1), some place cells in N had a delay period before their place fields first appeared. If synaptic plasticity is occurring during this delay period to contribute to the formation of new place fields, it appears to occur in the absence of somatic action potential firing and back-propagation into the dendrites. We therefore looked for dendrite-localized calcium transients that might result from local clustered synaptic input (possibly generating local regenerative events) capable of inducing synaptic potentiation in the absence of somatic firing (Schiller, Major et al. 2000, Oakley, Schwindt et al. 2001, Wei, Mei et al. 2001, Losonczy and Magee 2006, Milojkovic, Zhou et al. 2007, Major, Polsky et al. 2008, Palmer, Shai et al. 2014, Brandalise, Carta et al. 2016, Weber, Andrasfalvy et al. 2016).

Across 17 delayed onset place fields in N we detected 33 calcium transients that occurred in the basal dendrites in the absence of detectable somatic calcium transients (Figure 2.5B) during the delay period (these occurred across n = 8 place fields from n = 7 mice). Most of these dendrite-localized transients occurred in single branches (24/33; Figure 2.3B bottom, Figure 2.6A) with no detectable transients in the other imaged branches (mean number of branches imaged per cell was 17, range: 9-36). Interestingly, the other 9 dendritic transients occurred simultaneously in 9 different branches of the same cell (12 branches were imaged in total), again without a detectable somatic transient (Figure 2.5A). The majority (30/33) of these dendrite localized transients appeared to invade an area encompassing both shaft and spines across the imaged section of the local branch (Figure 2.6B and 2.6C; dendritic area of significant ΔF/F increases greater than single spines 5.58 – 26.11 μm2, n = 30) and therefore spread further across the branch than a separate class of calcium transients which were restricted to single spines (dendritic area of significant ΔF/F increases in spines 0.36 – 2.51 μm2, n = 63, data not shown) (Sheffield and Dombeck 2015). The spatial spread for the 30 dendrite localized transients represents a lower bound of the actual extent of the transients, since our imaging plane transected only a small region of each branch. We then identified the track locations where these 30 dendrite localized transients occurred and found that 22/30 occurred within the boundaries of the somatic place field that would soon form (occurring 9.1 ± 4.6 laps STD and 183.2 ± 96.6 seconds STD before place field onset), occurred more frequently at the beginning of these boundaries (19 occurred earlier on the track and 3 occurred later on the track relative to the mean somatic place field center of mass; Chi-squared test for proportional difference, $p < 0.001$), and occurred more within these boundaries than in other track locations (Figure 2.6A, 2.6D; Chi-squared test for proportional difference, $p < 0.001$).

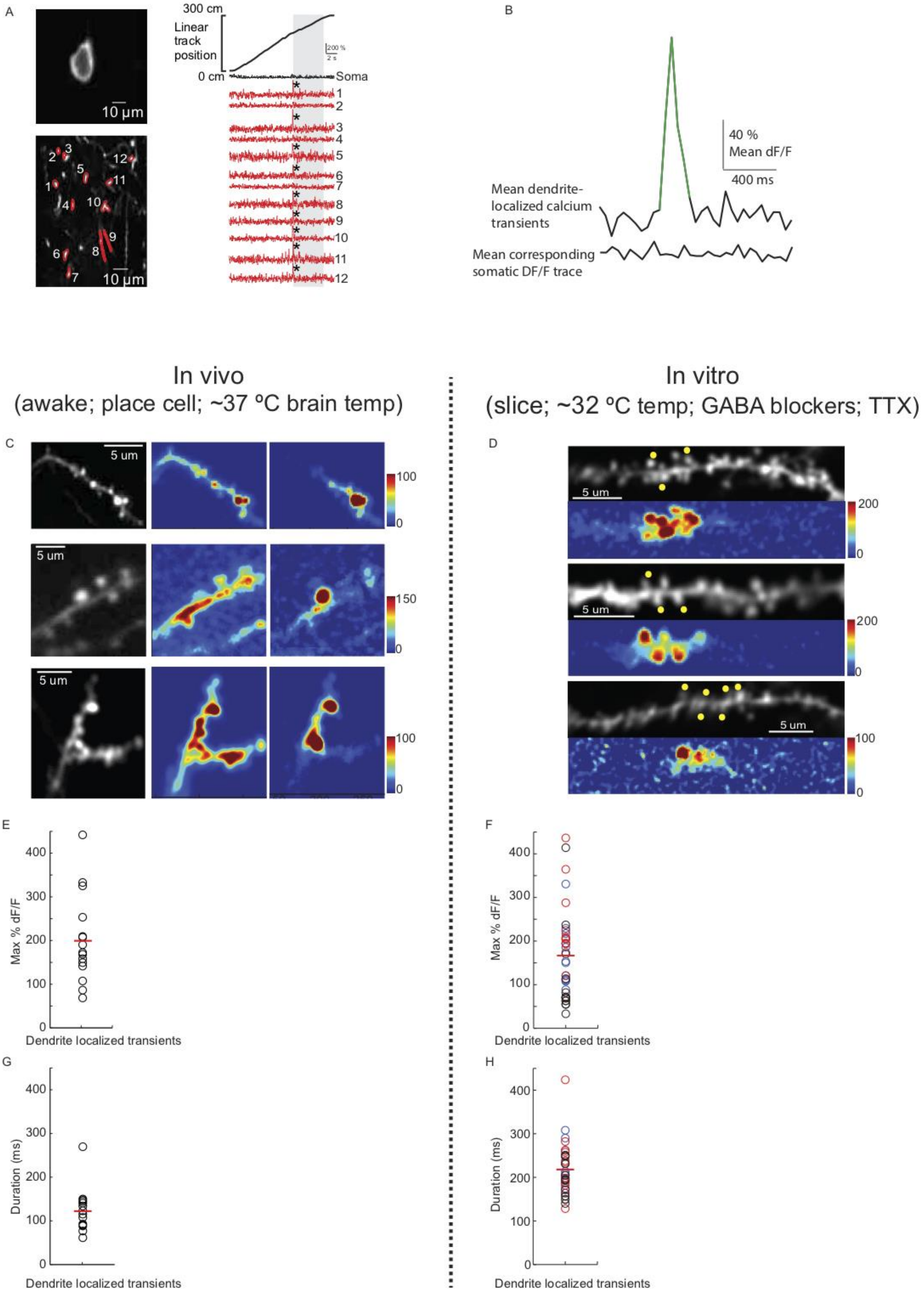
A
10 µm
10 µm
1
2
3
4
5
6
7
8
9
10
11
12
300 cm
Linear track position
0 cm
200 %
2 s
Soma
B
40 %
Mean dF/F
400 ms
Mean dendrite-localized calcium transients
Mean corresponding somatic DF/F trace
In vivo
(awake; place cell; ~37 ºC brain temp)
In vitro
(slice; ~32 ºC temp; GABA blockers; TTX)
C
5 um
100
0
5 um
150
0
5 um
100
0
D
5 um
200
0
5 um
200
0
5 um
100
0
E
Max % dF/F
0
100
200
300
400
Dendrite localized transients
F
Max % dF/F
0
100
200
300
400
Dendrite localized transients
G
Duration (ms)
0
100
200
300
400
Dendrite localized transients
H
Duration (ms)
0
100
200
300
400
Dendrite localized transients

v Figure 2.5: In vivo and in vitro dendrite restricted calcium transients have similar properties

(A) Left, co-acquired images of place cell soma and dendrites that displayed a delayed-onset place field in the novel environment. Right, ΔF/F traces from the (co-acquired) soma (black trace) and numbered dendritic branches (red traces) from a traversal during the delay period (lap 6; place field onset lap was lap 20). Gray column indicates the mean somatic place field. Significant calcium transients are indicated with stars. Note, 9/12 dendrites showed a significant calcium transient in the absence of a detectable somatic calcium transient on this lap during the delay period.

(B) Mean of all dendritic and all corresponding somatic ΔF/F traces for the 30 dendrite-localized calcium transients observed before place field firing; mean traces generated by triggering on peaks of the 30 dendrite-localized calcium transients. As in the individual ΔF/F traces, the average shows no detectable somatic calcium transient. Since even single action potentials are expected to generate transients greater than the 4.0% DF/F noise level (STD of noise) of the mean somatic trace using GCaMP6, these traces strongly suggests that no somatic action potentials are occurring with these 30 dendritic events.

(C) 3 example place cell dendrites (left; bottom and top are GCaMP6s-expressing, middle is GCaMP6f expressing) with heat maps depicting ΔF/F during dendrite-localized calcium transients (right) and branch spikes (middle, significant ΔF/F throughout entire branch) during high- resolution imaging. Images acquired during behavior in familiar environments.

(D) 3 example GCaMP6f-expressing dendrites in vitro with heat maps under each dendrite depicting ΔF/F during dendrite-localized calcium transients. Each transient was evoked by uncaging glutamate simultaneously on to the indicated spines (yellow circles).

(E) Max ΔF/F for each dendrite-localized calcium transient detected during the delay period of delayed-onset place fields (only GCaMP6f-expressing dendrites are included here; n = 16 dendrite-localized calcium transients from n = 4 mice).

(F) Max ΔF/F for each dendrite-localized calcium transient evoked in vitro with glutamate uncaging. Values are color coded for different ROIs: red depicts ROIs encompassing the entire spatial extent of the dendrite-localized calcium transient; blue depicts small ROIs (~1 μm diameter) placed in the center of the dendrite-localized calcium transient; black depicts small ROIs (~1 μm diameter) placed on the edge (away from soma) of the dendrite-localized calcium transient. (n = 13 dendrite-localized calcium transients from n = 5 mice). The range of dendrite-localized calcium transient amplitudes in vivo during the delay period is contained within the range of in vitro amplitudes (in vivo: 68%-442% ΔF/F vs. in vitro: 33%-436% ΔF/F), and the means were not significantly different (mean in vivo: 198.5% ± 27.5% ΔF/F vs. in vitro: 165.5% ± 16% ΔF/F, unpaired t-test, $p > 0.05$).

(G) Transient duration for each dendrite-localized calcium transient included in (E).

(H) Transient duration for each dendrite-localized calcium transient included in (F). Values are color coded for different ROIs in the same way as in (F). The range of dendrite-localized calcium transient durations in vivo were shorter, but largely contained within the range of in vitro durations (in vivo: 62-269 ms vs. in vitro: 128-424 ms), but the means were significantly different (mean in vivo: 121 ± 12 ms vs. in vitro: 215 ± 9 ms, unpaired t-test, $p < 0.001$). The longer durations in vitro could be due to general differences in conditions during in vitro recordings vs. in vivo, such as reduced temperature in vitro (~32 degrees C in vitro vs. 37 degrees C in vivo), blocked inhibition and greatly reduced network activity and neuromodulation. In addition, we measured ~5 times higher levels of baseline noise in the dF/F trace in vivo vs. in vitro. The increased noise in vivo would cause an ice-berg-like effect, leaving a portion of the transient hidden in the noise, making the observable transient duration shorter in vivo.

We next turned to an ex-vivo brain slice preparation to investigate possible mechanisms for the generation of dendrite localized calcium transients. We used established glutamate uncaging techniques to mimic synaptic inputs at selected spines along a single basal dendrite of a CA1 neuron expressing GCaMP6f (Losonczy and Magee 2006, Bloodgood and Sabatini 2007, Losonczy, Makara et al. 2008). Using a 2-photon microscope to image dendrites during spine stimulation, we found that simultaneous (within 5 ms) clustered input within 5-15 μm onto multiple spines (3 or more) often generated dendritic calcium transients that spread beyond the stimulated spines and into the nearby shaft (Figure 2.5D), a signature suggesting local dendritic spike generation (Schiller, Major et al. 2000, Oakley, Schwindt et al. 2001, Wei, Mei et al. 2001, Losonczy and Magee 2006, Milojkovic, Zhou et al. 2007, Major, Polsky et al. 2008, Palmer, Shai et al. 2014, Brandalise, Carta et al. 2016, Weber, Andrasfalvy et al. 2016). These dendrite-localized calcium transients stimulated in slice had transient amplitudes and durations similar to the dendrite-localized transients recorded during the delay period of delayed onset place fields in behaving mice (Figure 2.5).

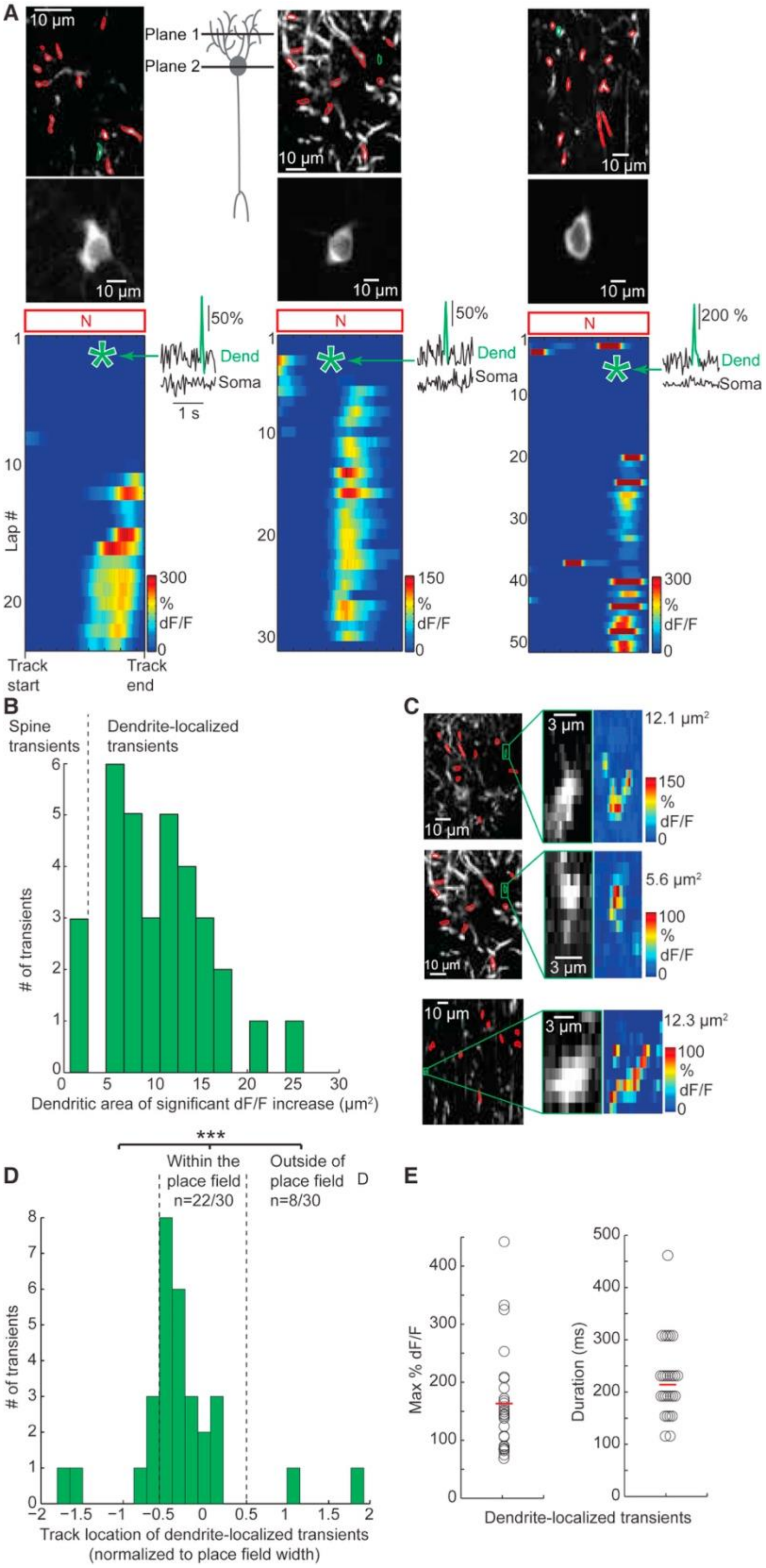
A
10 µm
Plane 1
Plane 2
10 µm
10 µm
10 µm
10 µm
10 µm
N
N
N
50%
50%
200 %
Dend
Soma
1 s
Dend
Soma
Dend
Soma
Lap #
1
10
20
1
10
20
30
1
10
20
30
40
50
300
%
dF/F
0
150
%
dF/F
0
300
%
dF/F
0
Track start
Track end
B
Spine transients
Dendrite-localized transients
# of transients
0
1
2
3
4
5
6
0
5
10
15
20
25
30
Dendritic area of significant dF/F increase (µm²)
C
10 µm
3 µm
12.1 µm²
150
%
dF/F
0
10 µm
3 µm
5.6 µm²
100
%
dF/F
0
10 µm
3 µm
12.3 µm²
100
%
dF/F
0
D
***
Within the place field n=22/30
Outside of place field n=8/30
D
# of transients
0
1
2
3
4
5
6
7
8
−2
−1.5
−1
−0.5
0
0.5
1
1.5
2
Track location of dendrite-localized transients (normalized to place field width)
E
Max % dF/F
0
100
200
300
400
Duration (ms)
0
100
200
300
400
500
Dendrite-localized transients

vi Figure 2.6: Putative local dendritic spikes predict the location of delayed onset somatic place fields

(A) Cartoon depicts co-recording from soma and basal dendrites of CA1 pyramidal cells. 3 Example place cells and their dendritic branches are shown (red regions, all branches belonging to the co-imaged soma; green regions, dendrites that displayed a dendrite-localized calcium transient; non-selected dendrites from different cells). Bottom, somatic place field transients lap by lap in N; first row representing first traversal mouse ever made across N. Green stars, track location where dendrite-localized calcium transient detected in indicated branch (at top) in the absence of a detectable somatic calcium transient (time-series ΔF/F traces from the branch and soma shown at right).

B) Histogram of the area of significant Δ*F/F* increase for each dendrite-localized calcium transient detected during the delay period of delayed-onset place fields. The area of significant Δ*F/F* increase for known single spine-restricted calcium transients (likely single synaptic inputs, not shown) are all less than dotted line.

(C) 3 example dendrites showing dendrite-localized calcium transients from different place cells during delay period. Left: Same as (A) top. Middle: magnified view of the indicated dendrites. Right: ΔF/F image of the indicated dendrites during dendrite-localized calcium transients. Area of significant Δ*F/F* increase (>3 s.d.) at right.

(D) Histogram of track locations of all dendrite-localized calcium transients that occurred during the delay period of delayed-onset place fields relative to the location of the later forming somatic place field (somatic field center at 0; running direction from negative to positive; only transients > threshold in (B) included). ***, Chi Squared proportionality test, $p < 0.001$.

(E) Max ΔF/F and transient duration for each dendrite-localized calcium transient (only transients > threshold in (B) included).

Based on the observations that the 30 dendrite-localized calcium transients 1. Occur in the absence of detectable somatic calcium transients, 2. Invade an area larger than a single spine and encompassing local spines and shaft in the imaging plane, and 3. Have amplitudes and durations similar to transients stimulated with clustered synaptic input in slice, we conclude that these dendrite-localized calcium transients are caused by clustered input onto single basal branches, presumably generating local dendritic spikes, during the delay period in delayed onset place cells. Some of these 30 dendrite-localized calcium transients may represent nonlinear amplification of spine calcium signals by clustered synaptic input that does not reach full dendritic spike status (Weber, Andrasfalvy et al. 2016), and therefore we refer to these 30 events as “putative” local dendritic spikes. Importantly, both full dendritic spikes and clustered inputs that just fall short of generating local dendritic spikes are capable of triggering synaptic potentiation (Weber, Andrasfalvy et al. 2016).

To approximate the frequency of these putative local dendritic spikes across the whole basal dendritic arbor of each delayed forming place cell (n = 17) on each lap during the delay period, it was first necessary to estimate the spatial spread of the putative local dendritic spikes *in vivo*. We made a separate set of high-resolution time-series movies from long stretches of basal dendritic branches of place cells (not during delay periods, n = 3 mice). We identified 4 putative local dendritic spikes from 3 different branches that closely resembled those observed in slice (Figure 2.5C, D). The total length of dendrite invaded by these transients could be measured since they were contained within the imaged branch: range of 5.9 - 8.5 um, mean of 7.5 um, similar to other reports (Schiller, Major et al. 2000, Major, Polsky et al. 2008, Lavzin, Rapoport et al. 2012, Palmer, Shai et al. 2014, Brandalise, Carta et al. 2016, Weber, Andrasfalvy et al.

2016). We first assumed that the spread of these 4 putative local dendritic spikes represents an estimate of the spread of the 30 putative local dendritic spikes observed during the delay period (the two classes of putative spikes, 4 and 30, had similar amplitude and kinetics as well). Then, based on this spread, the total length of the basal arbor in each cell and the fraction of the arbor imaged in each cell, and further assuming that putative local dendritic spikes occur at random locations in the arbor, we estimate that ~2 putative local dendritic spikes occur across the basal arbor on each lap during the delay period in each cell. Taken together, these results suggest that the first step in the formation of many delayed onset place fields may be the occurrence of clustered synaptic input leading to sparse local dendritic spiking and local synaptic potentiation.

2.3.4 Dendritic inhibition is transiently reduced during exposure to novel environments

Due to the observations that most place fields appear during the first 8 laps in N, dendritic branch spiking in place fields is increased during this period and putative local dendritic spikes are occurring in dendrites prior to the formation of many delayed onset place fields, we asked whether changes in dendritic inhibition might influence these processes. Inhibition levels in the hippocampus are altered during exposure to novel environments (Wilson and McNaughton 1993), although the specific interneuron subtypes involved remain unknown. We utilized somatostatin-Cre (SOM+) mice to obtain expression of GCaMP6f in a sub-population of interneurons (Lovett-Barron, Kaifosh et al. 2014), which includes cells targeting the basal dendrites of CA1 pyramidal cells in the Stratum Oriens region (Bistratified interneurons (Goldberg and Coulter 2013)), and imaged their axons in the Stratum Oriens, using the change in fluorescence across the axon population as a bulk measure of inhibition to the pyramidal cell dendritic region (Figure 2.7A).

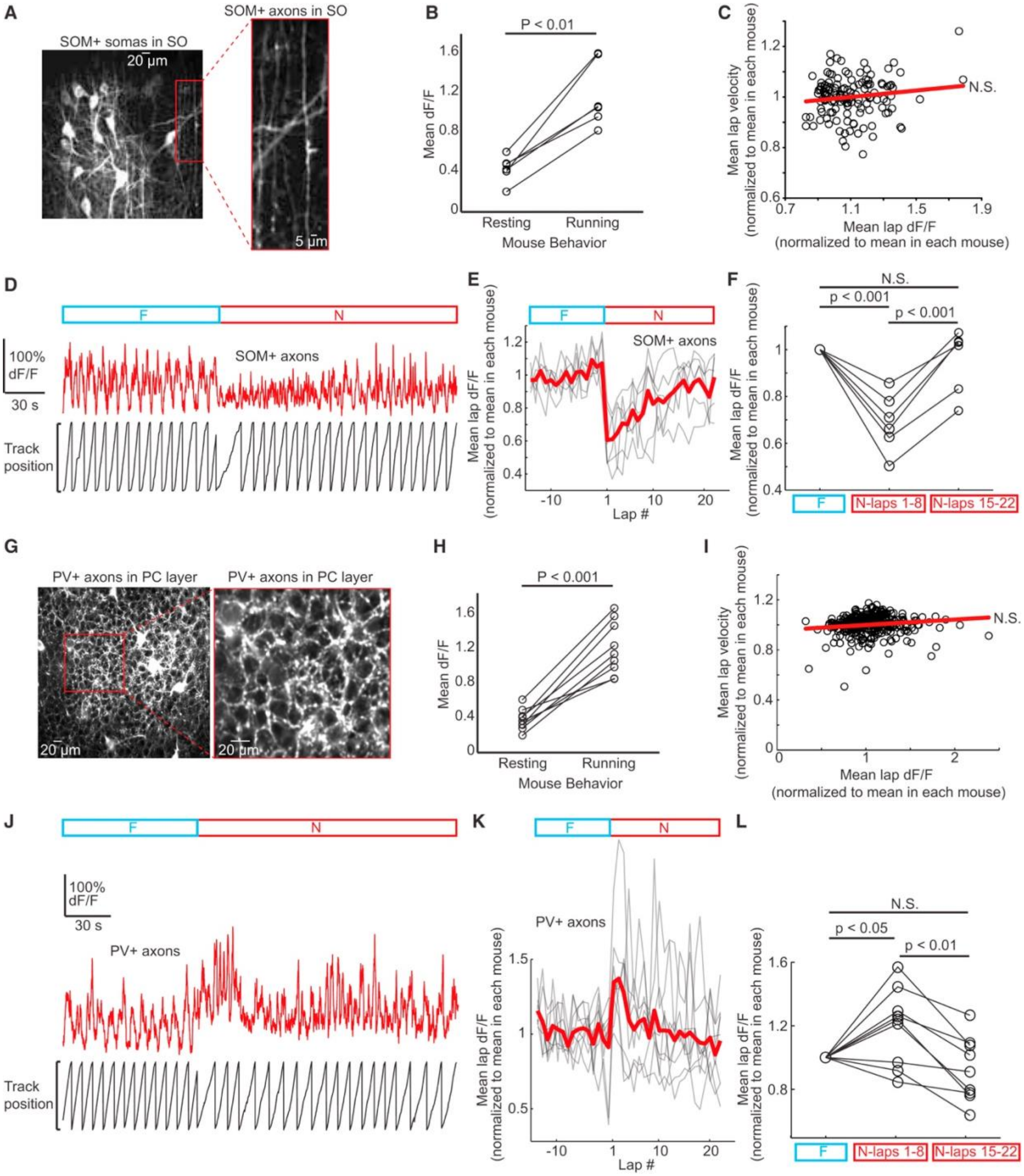

vii Figure 2.7: Dendritic inhibition is transiently reduced and somatic inhibition is transiently increased following exposure to novel environments

(A) GCaMP6f-expressing SOM+ interneuron cell bodies (left) and axons (right) in Stratum Oriens of CA1 *in vivo*.

(B) Mean SOM+ interneuron axonal ΔF/F (average over all axons in field) during running vs resting in F (Paired t-test). Open circle, means from 6 sessions in F from 3 mice.

(C) Mean velocity vs mean axonal ΔF/F on each lap in F (6 sessions). N.S., Linear regression, slope not significantly different from 0.

(D) Bottom: Single mouse behavior of track position vs time during F to N switch. Middle: axonal ΔF/F during switch.

(E) Mean axonal ΔF/F during running on each lap (normalized to the mean in F in each case) during F to N switch (6 switches; n = 3 mice). Mean from all mice in red.

(F) Normalized Mean axonal ΔF/F during running in F, laps 1-8 in N and laps 15-22 in N. Open circles represent each F to N switch. Repeated measures ANOVA with Tukey's post-test, N.S., $p > 0.05$.

(G) GCaMP6f-expressing PV+ interneuron cell bodies and axons in CA1 Pyramidal cell layer *in vivo*.

(H) Mean PV+ interneuron axonal ΔF/F (average over all axons in field) during running vs resting in F (Paired t-test). Open circle, means from 9 sessions in F from 5 mice (one mouse had only one F to N switch).

(I) Mean velocity vs mean axonal ΔF/F on each lap in F (9 sessions). N.S., Linear regression, slope not significantly different from 0.

(J) Bottom: Single mouse behavior of track position vs time during F to N switch. Middle: axonal ΔF/F during switch.

(K) Mean axonal ΔF/F during running on each lap (normalized to the mean in F in each case) during F to N switch (9 switches; n = 5 mice). Mean from all mice in red.

(L) Normalized Mean axonal ΔF/F during running in F, laps 1-8 in N and laps 15-22 in N. Open circles represent each F to N switch. Repeated measures ANOVA with Tukey's post-test, N.S., $p > 0.05$.

Axonal ΔF/F increased when mice transitioned from resting to running in F (Figure 2.7B; n = 3 mice, n = 6 sessions; mean resting ΔF/F = 43.8 ± 0.1%, mean running ΔF/F = 118.3 ± 0.1%; $p < 0.01$, Paired Student’s t-test), although their absolute velocity was not correlated to ΔF/F (Figure 2.7C; slope not significant with 95% confidence bounds). We found that switching from F to N was associated with an abrupt *decrease* in mean axonal ΔF/F during running (Figure 2.7-F; mean ΔF/F in the first 8 laps in N = 0.69 ± 0.05 SEM; each lap normalized to mean ΔF/F in F in each case; $p < 0.001$, Repeated measures ANOVA with Tukey's post-test) that gradually returned to F levels (Figure 2.7D-F; 0.94 ± 0.05 SEM in the last 8 laps in N; $p > 0.05$ compared to F, Repeated measures ANOVA with Tukey's post-test). Importantly, these changes were not observed at the beginning of sessions when mice were first exposed to F (Figure 2.4G). These data demonstrate that the level of pyramidal neuron basal dendritic inhibition from SOM+ interneurons transiently decreases during initial exposure to a novel environment. Such a reduction could create a time-window in which branch spikes and localized dendritic spikes induce synaptic potentiation, allowing specific sets of (potentiated) synapses to drive somatic firing in the place field once inhibition returns to F levels.

We next measured the level of somatic inhibition to CA1 pyramidal neurons during exposure to N. Parvalbumin-Cre mice were utilized to gain expression of GCaMP6f in basket cell axons using the same strategy as above for SOM+ axons. Axons from these interneurons form basket-like structures around CA1 pyramidal cell somata (Figure 2.7G). We measured mean changes in fluorescence of these axon structures as a bulk measure of somatic inhibition. As with SOM+ axons in the Stratum Oriens, basket cell axonal ΔF/F increased when mice transitioned from resting to running in F (Figure 2.7H; n = 5 mice, n = 9 sessions; mean resting ΔF/F = 38.9 ± 4.1%, mean running ΔF/F = 121.8 ± 10.2%; $p < 0.001$, Paired t-test), and their absolute velocity was also not correlated to ΔF/F (Figure 2.7I; slope not significant with 95% confidence bounds). Basket cell axons surrounding pyramidal cell somata showed an abrupt *increase* in mean axonal ΔF/F during running when the environment was switched from F to N (Figure 2.7J-L; mean ΔF/F in the first 8 laps in N (each lap normalized to mean ΔF/F in F in each case) = 1.15 ± 0.05 SEM; $p < 0.05$, Repeated measures ANOVA with Tukey's post-test) that gradually returned to F levels (Figure 2.7J-L; 0.94 ± 0.07 SEM; $p > 0.05$ compared to F, Repeated measures ANOVA with Tukey's post-test). Importantly, these changes were not observed at the beginning of sessions when mice were first exposed to F (Figure 2.4E). These data demonstrate that the level of pyramidal neuron somatic inhibition from PV+ interneurons transiently increases during initial exposure to a novel environment.

2.3.5 NMDA receptors in CA1 pyramidal neurons are required for the formation of a subset of place fields

To test the involvement of NMDA receptors in branch spiking, remapping and place field formation during novel environment exposure, we used an inducible NMDA knock-down strategy. The gene encoding the NR1 subunit that is necessary for functional NMDA receptors can be knocked down in *Grin1*$_{lox/lox}$ mice (referred to here as NR1 mice) in a Cre-dependent manner (McHugh, Blum et al. 1996, Tsien, Huerta et al. 1996). We therefore injected AAV-CaMKII-Cre along with AAV-Syn-flexed-GCaMP6f into the dorsal CA1 region of these mice to obtain Cre-dependent expression of GCaMP6f and Cre-dependent knock down of NR1 exclusively in the same neurons (Figure 2.8A).

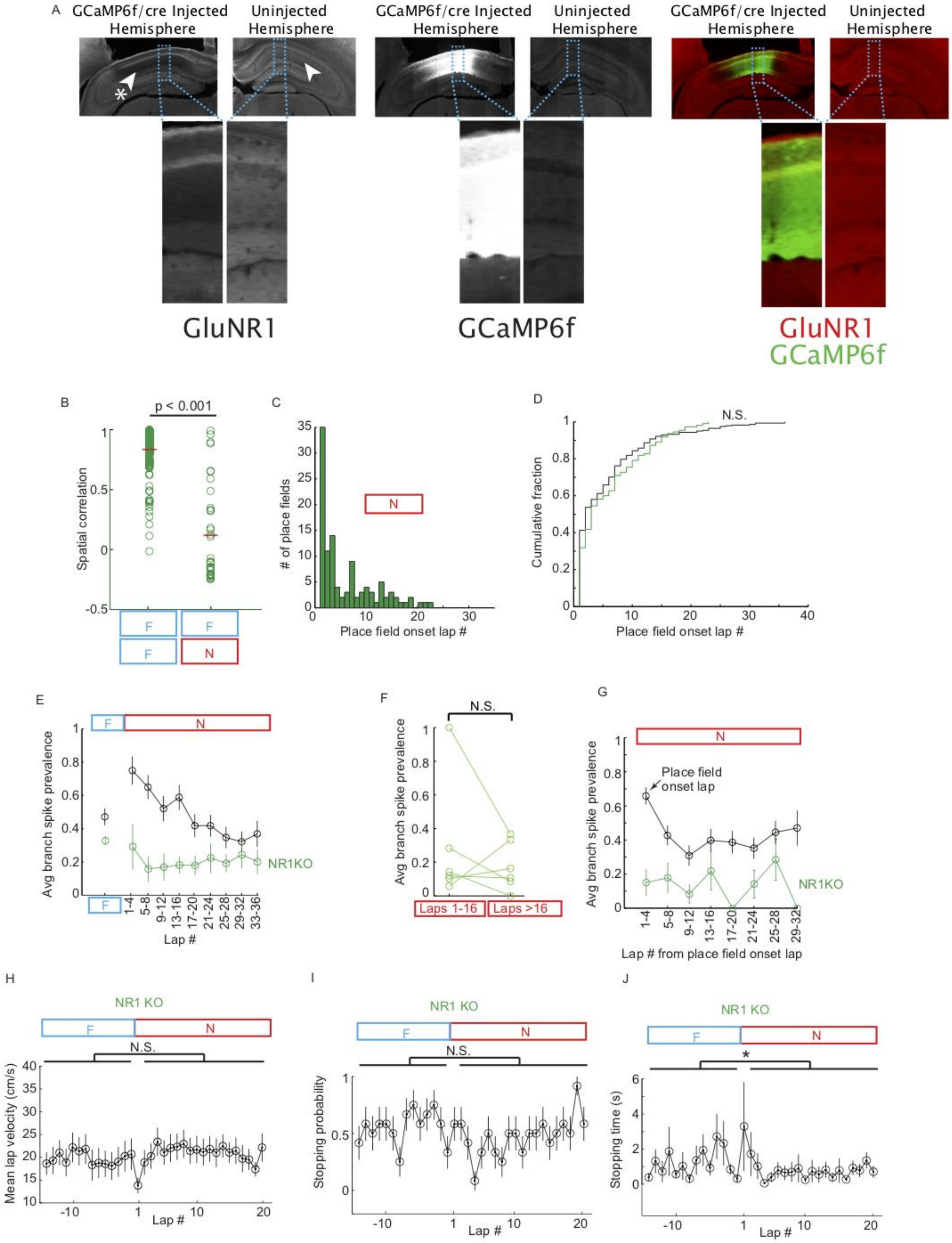

viii Figure 2.8: Mouse behavior, place field properties and branch spiking in NR1 mice

(A) Post mortem imaging of representative fixed slices from NR1 mice with functional NMDA receptors knocked out of GCaMP6f-expressing cells (green). Left slice from hemisphere with GCaMP6f/cre expression and right slice from contralateral hemisphere of same mouse without GCaMP6f/cre expression. NR1 subunit of NMDA receptors labeled via immunohistochemistry (red). Both hemispheres were imaged simultaneously so brightness can be compared directly. Note reduced NR1 immuno-fluorescence in injected vs uninjected hemisphere (white arrows). Based on this slice and similar slices from other animals, we estimate that ~50,000-100,000 CA1 neurons had knockdown of functional NMDA receptors in each mouse.

(B) Same as Figure 1D, but for NR1 mice with functional NMDA receptors knocked out of GCaMP6f-expressing cells ($n = 3$ NR1 mice, $n = 5$ environment switches from F to N; unpaired t- test, $p < 0.001$).

(C) Same as Figure 1F1, but for NR1 mice with functional NMDA receptors knocked out of GCaMP6f-expressing cells ($n = 3$ NR1 mice; $n = 5$ sessions in N)

(D) Cumulative fraction plots of the data in Figure S4C (green) and Figure 1F1 (black) (Wilcoxon rank sum test, $P > 0.05$)**.**

(E) Same as Figure 2C, but with the addition of branch spiking data from NR1 mice with functional NMDA receptors knocked out of (sparsely labeled) GCaMP6f-expressing cells. (F, $n = 16$ place fields from $n = 4$ NR1 mice; N, 4 laps binned, $n = 6$ place fields from $n = 3$ NR1 mice).

(F) Same as Figure 2E, but from NR1 mice with functional NMDA receptors knocked out of (sparsely labeled) GCaMP6f-expressing cells ($n = 6$ place fields from $n = 3$ NR1 mice; Paired t-test $p > 0.05$).

(G) Same as Figure 2F, but with the addition of branch spiking data from NR1 mice with functional NMDA receptors knocked out of (sparsely labeled) GCaMP6f-expressing cells.

(H) Summary data across all NR1 mice of mean lap velocity before and after environment switch (n = 7 NR1 mice; n = 12 environment switches from F to N). Data are presented as mean ± SEM for each lap. Lap velocity is significantly slower on the first lap in N compared to rest of N (Paired t-test, $p < 0.05$), but F and N lap 2 onwards are not significantly different (Paired t-test, $p > 0.05$). (I) Summary data across all NR1 mice of stopping probability before and after environment switch. Stopping probability is not significantly different on the first lap in N compared to F (Paired t-test, $p > 0.05$), nor is it different between F and N lap 2 onwards (Paired t-test, $p > 0.05$).

(J) Summary data across all NR1 mice of stopping time before and after environment switch. Stopping time is significantly higher on the first lap in N compared to F (Paired t-test, $p < 0.05$), and is higher in F compared to N lap 2 onwards (Paired t-test, $p < 0.05$).

We found that the fraction of place fields that formed in N was significantly reduced in populations of CA1 neurons with NR1 knocked down (Figure 2.9A-C) compared to wildtype (WT) controls (fraction of place fields that formed from the active cell population in N: 0.24 ± 0.04 SEM in WT controls versus 0.11 ± 0.05 SEM in NR1 knock down, Chi Squared proportionality test, $p < 0.05$), consistent with previous findings in which other components of the plasticity pathway were knocked out (Rotenberg, Mayford et al. 1996). We found transient durations were not different between the NR1 knock down and WT populations and the maximum standard deviation of transients above the noise were slightly higher in the NR1 knock down population (Figure 2.10A, B). Therefore, the reduction in place fields in the NR1 knock down population could not be explained by a reduced ability to detect somatic transients compared to WT. We did observe a few differences in NR1 mouse behavior (decrease in running velocity and increase in stopping probability, Figure 2.8H-J) and a reduction in branch spiking in NR1 knock down (sparse NR1 knockdown and GCaMP6f expression) compared to WT place cells (Figure 2.8E-G), but spatial correlations and place field onset lap (for the reduced number of place cells) appeared similar to WT (Figure 2.8B-D). Further, putative local dendritic spikes were not observed in NR1 knock down place cells (sparse NR1 knockdown and GCaMP6f expression) during the delay period before somatic place fields formed; though ~8-fold fewer place cell dendrite recordings were available for analysis from the NR1 (fewer place cells with fewer dendrites) vs WT mice. Based on the frequency of putative local dendritic spikes observed in WT place cells, ~4 putative local dendritic spikes were expected from the NR1 knock down recordings.

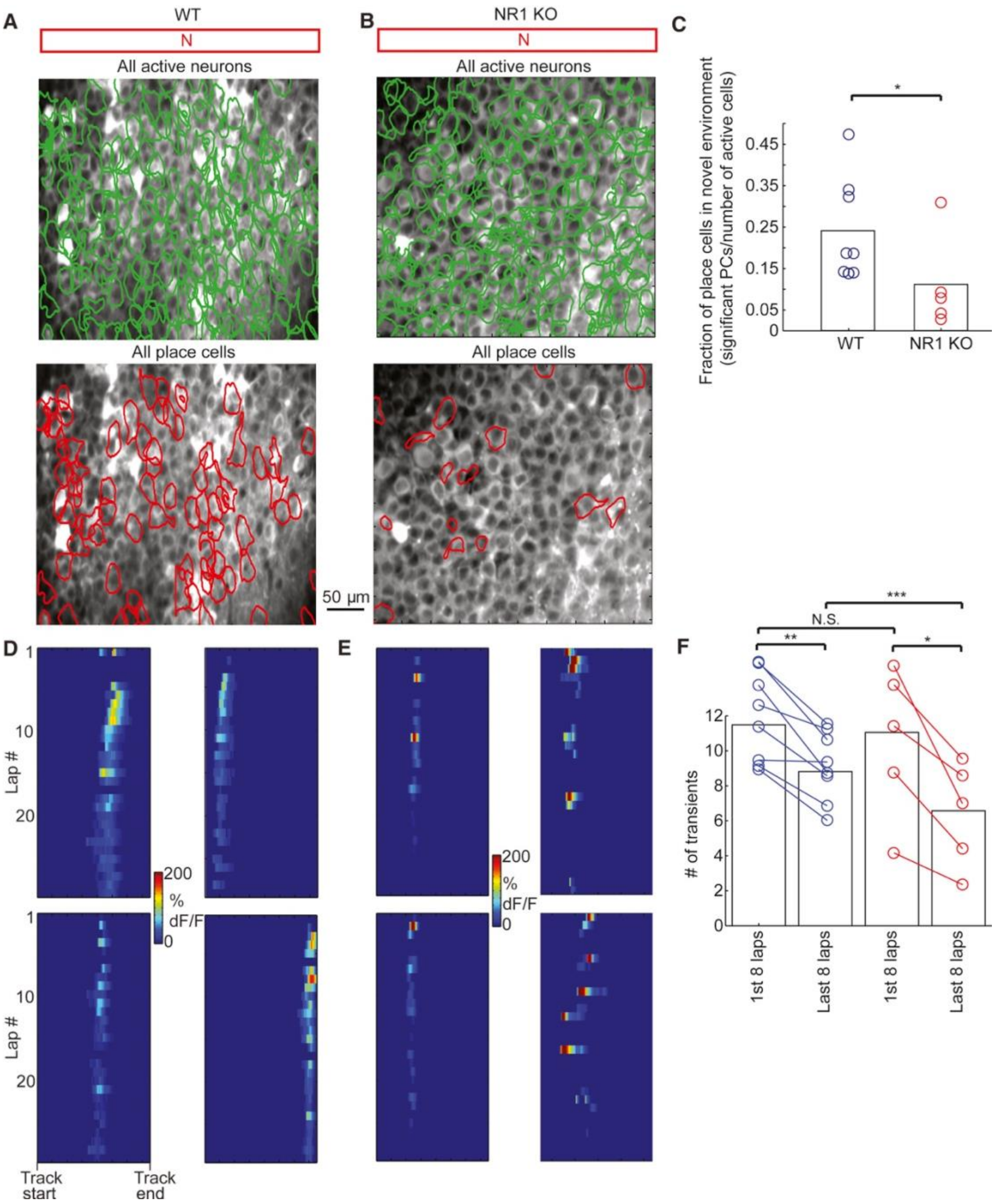

ix Figure: 2.9: NMDA receptors in CA1 pyramidal neurons are required for the formation of a subset of place fields

(A, B) GCaMP6f-expressing neurons in CA1 of WT (A) and NR1 (B, NMDA receptors functionally knocked out in GCaMP6f-expressing neurons) mouse. Top, all active neurons in the field of view in N (green). Bottom, All place cells encoding N (red).

(C) Fraction of the population of active cells in the field of view with a place field in N for WT vs NR1 mice. Open circles, fraction from individual fields of view. Bars, mean across all fields ($n = 8$ fields from WT $n = 5$ from NR1; from $n = 4$ WT, $n = 3$ NR1 mice). *, Chi Squared proportionality test, $p < 0.05$.

(D and E) Somatic place field transients shown lap by lap in N in WT mice (4 in D) and NR1 mice with functional NMDA receptors knocked out of GCaMP6f-expressing cells (4 in E); first row represents first traversal mouse ever made across N. Somatic place field calcium transients have higher dF/F amplitudes during initial laps and for cells lacking NMDA receptors, fields tend to disappear towards session end (E).

(F) Mean number of significant calcium transients detected from all active cells in WT mice ($n = 4$ mice, $n = 1882$ transients; blue) and NR1 mice with functional NMDA receptors knocked out of GCaMP6f-expressing cells ($n = 3$ mice; $n = 835$ transients; red). Blue to red, Unpaired t-test, ***, $p < 0.001$; N.S., $p > 0.05$; Within color, paired t-test, **, $p < 0.01$, * $p < 0.05$; all t-tests with Bonferroni correction. Bars, mean from all transients across all mice. Open circles, means from each field of view.

Interestingly, some of the place fields that formed in the NR1 knock down population in N displayed a reduction in somatic firing frequency throughout the session (somatic calcium transients decreased in frequency throughout the session; Figure 2.9E), more so than in the WT population (Figure 2.9D). This suggests that although place fields can form in CA1 pyramidal neurons in the absence of functional NMDA receptors, their ability to maintain place field firing over time is diminished. One possible explanation for this finding is that a lack of synaptic potentiation occurs in the dendrites of the NR1 knock down population during the window of lowered inhibition upon initial exposure to N, which leads to an effective reduction in synaptic drive when inhibition returns to baseline levels. To further explore this hypothesis, we measured the number of detectable somatic transients during the first 8 laps in N and compared these numbers to the last 8 laps in N in all active neurons in both the NR1 knock down and WT populations ($n = 1882$ neurons from $n = 4$ WT mice; $n = 835$ neurons from $n = 3$ NR1 mice; estimated fraction of active cells in the field of view in WT = 0.46 ± 0.02 SEM versus 0.46 ± 0.04 SEM in NR1). We found that in both populations the number of transients was significantly higher during the first 8 laps versus the last 8 laps (Figure 2.9F; first 8 laps WT = 11.5 ± 0.1 SEM vs. last 8 laps WT = 8.8 ± 0.1 SEM, $p < 0.01$, Paired t-test; first 8 laps NR1 = 11.1 ± 0.2 SEM vs. last 8 laps NR1 = 6.6 ± 0.2 SEM, $p < 0.05$, Paired t-test; t-tests with Bonferroni correction). Also, the number of transients during the first 8 laps was not different between the NR1 knock down and WT populations (Figure 2.9F; first 8 laps WT = 11.5 ± 0.1 SEM vs. first 8 laps NR1 = 11.1 ± 0.2 SEM, $p > 0.05$, Unpaired t-test). However, there was a greater reduction in transient number in the last 8 laps in the NR1 knock down versus WT populations (Figure 2.9F, last 8 laps WT = 8.8 ± 0.1 SEM vs. last 8 laps NR1 = 6.6 ± 0.2 SEM, $p < 0.001$, Unpaired t-test; t-tests with Bonferroni correction). At the same time, no differences in transient amplitude or duration were observed between the NR1 knock down and WT populations (Figure 2.10D,E).

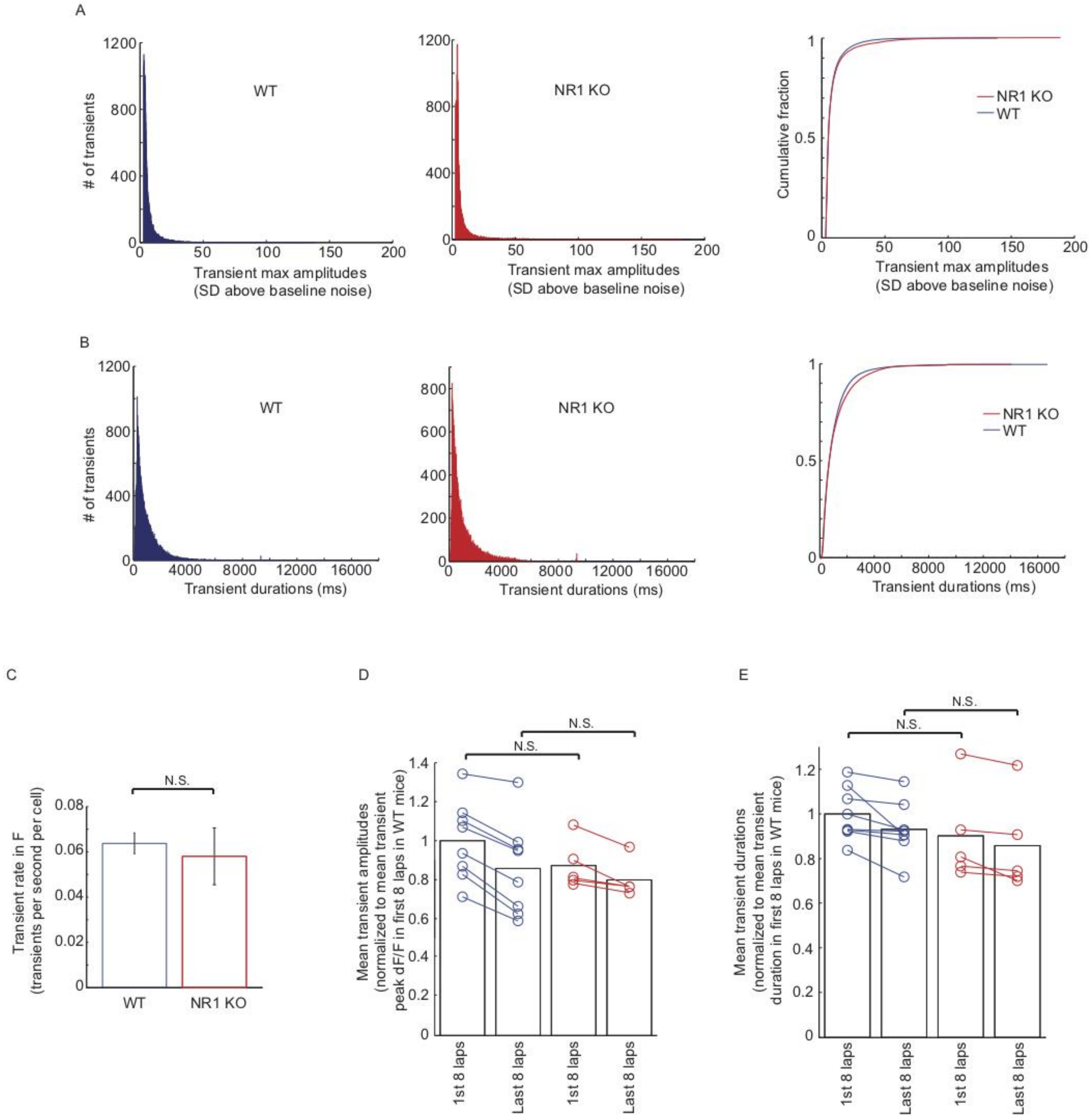

x Figure: 2.10: Somatic calcium transient detection is similar in NR1 knock down and WT populations

(A) Histograms showing maximum calcium transient amplitude of every transient detected from all active cells from all fields of view (in F) in units of standard deviation above baseline noise in wildtype (Left, blue, n = 35557 transients from n = 4 mice) and NR1 knock down (Middle, red, n

= 30293 transients from n = 3 mice) populations. Cumulative fraction plots of the histograms reveal a close similarity in the distribution, which are not statistically different (Wilcoxon rank sum test, $p > 0.05$). Cumulative plots are color coded to match histograms.

(B) Same as in (A) but for somatic calcium transient durations (in F). The cumulative fraction plot for NR1 knock down transients is slightly shifted to the right of the wildtype plot, indicating slightly longer transient durations in these mice (Wilcoxin rank sum test, $p < 0.001$).

(C) Transient rate (in F) for same transients from (A) and (B). No significant difference in transient rate between NR1 knock down and WT populations in F (Unpaired t test, $p > 0.05$).

(D) Transient amplitude (in N) for same transients from Figure 5F. No significant difference in amplitudes of these transients between NR1 knock down and WT populations in first or last 8 laps (Unpaired t test, $p > 0.05$).

(E) Transient durations (in N) for same transients from Figure 5F. No significant difference in durations of these transients between NR1 knock down and WT populations in first or last 8 laps (Unpaired t test, $p > 0.05$).

These results suggest that somatic firing is largely not dependent on functional NMDA receptors (McHugh, Blum et al. 1996, Kentros, Hargreaves et al. 1998, Ekstrom, Meltzer et al. 2001) during the initial exposure to a novel environment. Instead, NMDA receptors may act to potentiate synapses during this period so that when dendritic inhibition returns to baseline levels these synapses become strong enough to drive somatic firing. This process may be necessary for the formation of a firing field in a subset of CA1 place fields, although in other cells across the CA1 population place fields can still form without NMDA dependent synaptic potentiation (Figure 2.11).

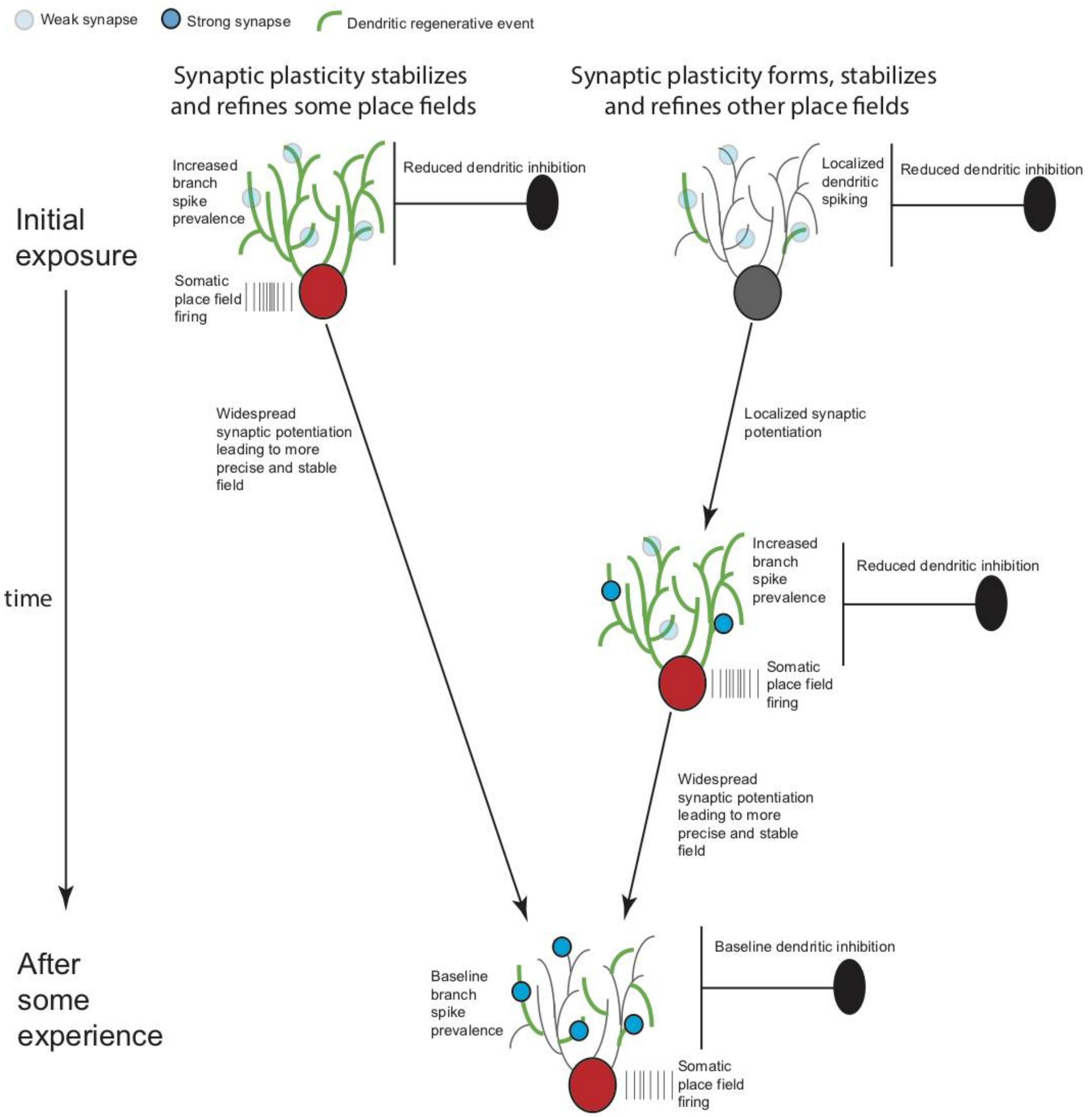

xi Figure 2.11: Proposed mechanisms of CA1 place field formation.

We propose that there are two different pathways that can lead to place field formation during exposure to novel environments. One pathway in which the sum of all synaptic inputs is strong enough upon initial exposure to drive action potential firing in the new place field (left), and one pathway in which the sum of all synaptic inputs is too weak to drive somatic firing (right).

Spatially clustered weak inputs can be potentiated in the presence of local dendritic spikes which are promoted during a window of reduced dendritic inhibition. Over many minutes these inputs become strong enough to drive somatic firing in a new place field. In both pathways, high levels of branch spiking co-occurs with the first appearance of somatic firing in the place field, which also occurs during lowered dendritic inhibition. This branch spiking likely serves to spatially refine and temporally stabilize the place field through induction or maintenance of widespread synaptic potentiation across the dendritic arbor. For both pathways, dendritic inhibition then increases back to familiar environment levels, closing the window for plasticity/potentiation and stabilizing the synaptic changes that took place to encode the new environment.

2.4 Discussion

We propose the existence of two pathways that can lead to place field formation during exposure to novel environments. In the first, the sum of all synaptic inputs is large enough upon initial exposure to drive action potential firing at a particular location (the new place field; Figure 2.11 left). The other pathway is one in which the sum of all synaptic inputs is initially too small to drive somatic firing, but after a subset of inputs that are active at a particular location are potentiated, they become strong enough to drive somatic place field firing in the new place field (Figure 2.11 right). Supporting the idea that some place fields do not require synaptic plasticity to form, we found many place fields with somatic firing on the first lap in a novel environment. Although this somatic firing co-occurred with high levels of branch spiking, any potentiation produced by these dendritic events could not have been required for the coincident firing in the new place field; instead, potentiation produced by these dendritic events may act to refine the fields further (see below). Supporting the case that synaptic plasticity is required to form many other place fields, we found localized putative dendritic spikes (likely NMDA spikes (Schiller, Major et al. 2000, Brandalise, Carta et al. 2016)) occurring before detectable somatic firing on the first few laps of novel environment exposure. These putative local dendritic spikes likely potentiate small clusters of synapses, which over many minutes become strong enough to drive somatic firing and increased levels of branch spiking in a new place field. In further support of the idea that two different pathways can lead to new place fields, we found that knocking out NMDA receptors in a population of CA1 neurons reduced the number of place fields that formed across the population by ~50%. This suggests that approximately half of CA1 place fields require synaptic plasticity to form, and half do not.

In both of the proposed pathways for place field formation, nearly all place fields displayed high BSP when somatic firing first appeared. One possible purpose of this high BSP may be to refine place fields by strengthening co-occurring inputs throughout the arbor so that somatic firing becomes more spatially precise and place fields more temporally stable (Cacucci et al., 2007; Kentros et al., 1998; McHugh et al., 1996; Rotenberg et al., 1996; Sheffield and Dombeck, 2015). This is supported by NMDA dependent plasticity perturbation experiments (Cacucci et al., 2007; Kentros et al., 1998; McHugh et al., 1996) in which the place fields that formed were less precise and less stable. Therefore, synaptic plasticity likely plays a fundamental role in the normal development of all place fields (Wilson and McNaughton 1993, Lever, Wills et al. 2002, Dragoi, Harris et al. 2003), by stabilizing and refining them, but is additionally required for the formation of a subset of place fields (through local dendritic spike induced potentiation). In both cases, these processes are likely influenced by the initial decrease in dendritic inhibition. The subsequent return of dendritic inhibition likely increases the amount of input required to drive any further synaptic changes, therefore closing the window for large amounts of synaptic plasticity to occur and stabilizing the synaptic changes that took place to encode the new environment.

Burst firing in CA1 pyramidal neurons, likely driven by coincident CA3 (onto CA1 basal, oblique and proximal apical dendrites) and EC3 input (onto CA1 distal apical tuft dendrites), is associated with the formation of new place fields in familiar environments (Bittner, Grienberger et al. 2015). Synapses from multiple input pathways may become potentiated during burst events, leading to the binding of information across multiple input streams and allowing these synapses to drive firing on subsequent traversals in a new place field. Our data showing high levels of branch spike prevalence (BSP) when place fields first appear in novel environments supports this idea. Indeed, high BSP in basal dendrites appears to be a dendritic measure indicating the occurrence of somatic burst firing in CA1 pyramidal neurons (Grienberger, Chen et al. 2014). It is therefore likely that somatic burst firing and high levels of BSP co-occur when somatic firing first appears in many place fields. However, we also found that the first appearance of a small percentage of place fields was associated with low levels of BSP, suggesting bursting, high levels of BSP and further binding of information across CA3 and EC3 is not necessary for the formation of all place fields. Furthermore, our observation of putative local dendritic spikes prior to the formation of detectable place field firing suggests that additional steps may be required to form place fields in many cells, with localized dendritic spikes starting the process by potentiating a small subset of synapses from one input stream or the other (CA3 or EC3). Once potentiated, these inputs can then drive place field firing, higher levels of BSP and burst firing to recruit more inputs (possibly over behavior timescales (Bittner, Milstein et al. 2017)) to make the fields more precise, stable and possibly representing bound information across EC3 and CA3.

Local dendritic spikes have been shown to play functionally important roles *in vivo* (Cichon and Gan, 2015; Lavzin et al., 2012; Palmer et al., 2014; Sheffield and Dombeck, 2015; Smith et al., 2013), and in brain slices are capable of inducing synaptic potentiation (Brandalise et al., 2016; Golding et al., 2002; Gordon et al., 2006; Hardie and Spruston, 2009; Magee and Johnston, 1997; Weber et al., 2016). We estimate that ~2 putative local dendritic spikes occur across the basal dendritic arbor on each lap during the delay period prior to somatic place field appearance. It has been proposed that network information storage capacity is maximized when very few synapses are modified to store each new input pattern through localized dendritic spikes (Wu and Mel, 2009). This model also predicts that single branches that have undergone synaptic potentiation can then cause somatic firing. Our observations are consistent with these predictions, and part of the delay period that we observed in some place fields could be due to the time required for long term potentiation to fully take effect (Hardie and Spruston, 2009; Murakoshi et al., 2011; Tigaret et al., 2016). This idea is partly supported by a recent somatic intracellular place cell recording study that found increasing sub threshold responses in novel virtual environments before somatic place field firing began (Cohen, Bolstad et al. 2017).

Our previous work fits with the idea that NMDA receptors are involved in refining place fields since as we found that place fields with the highest BSP were more precise and stable in familiar environments (Sheffield and Dombeck, 2015), likely through their effect on alleviating Mg^{2+} block of NMDA receptors in the presence of presynaptic input. This suggests that once a cognitive map has been established through the initial steps described above (Figure 2.11), the synapses that drive firing in individual place fields are maintained in strength by branch spikes each time the animal experiences the same environment (and also possibly offline through replay events). However, in addition to this role in refining fields, here we found that NMDA receptors are likely required for the formation of ~50% of place fields in novel environments. NMDA receptors in CA1 therefore likely serve many roles: forming place fields in novel environments through synaptic potentiation, refining place fields and make them more precise and stable, and maintaining the precision and stability of place fields over time in familiar environments by maintaining synaptic strength.

One possible explanation for how some place fields can form without synaptic potentiation is that some synapses are pre-strengthened prior to novel environment exposure and are activated during the experience to drive somatic place field firing. Certain cells can be predicted to express place fields prior to exposure to a novel environment based on their participation in pre-play (Dragoi and Tonegawa 2011, Dragoi and Tonegawa 2013, Dragoi and Tonegawa 2014), suggesting experience-dependent synaptic plasticity plays little to no role in the appearance of these fields since their inputs are already able to drive firing prior to the experience. Place fields that engage pre-strengthened inputs could appear immediately upon exposure to novel environments, or even following a delayed period, as changes in attention could later activate these pathways (Monaco et al., 2014). It is also possible that NMDA-dependent synaptic plasticity occurs in presynaptic regions to drive some CA1 place field formation (Marr 1971).

Similar to the findings here, differential inhibitory dynamics (differential changes in PV+ and SOM+ axonal boutons) have been observed in the motor cortex of mice during motor learning (Chen, Kim et al. 2015). Differential changes in inhibition across the somato-dendritic compartment during learning may be a general mechanism that supports the formation of new representations in the brain. Further, different interneuron subtypes may be involved in extracting different components of the learned representation (Lovett-Barron, et al., 2014) and may be involved in routing information flow from CA3 and EC3 pathways during place field firing (Fernandez-Ruiz, Oliva et al. 2017).

Interestingly, significant differences were observed here between the F to N transitions compared to the F to F transitions (Figures 2.3,2.4, and 2.7), suggesting that increased attention or environmental saliency may play a role in changing the functional state of circuits in CA1. Neuromodulatory pathways may control this process, with likely candidates including cholinergic (Hasselmo and McGaughy 2004, Teles-Grilo Ruivo, Baker et al. 2017) and/or dopaminergic (Kentros, Agnihotri et al. 2004) inputs.

2.5 Methods

Mouse surgery and virus injections

Mice were anesthetized (~1-2% Isoflurane) and a small (~0.5–1.0 mm) craniotomy was made over the hippocampus (1.8 mm lateral, 2.3 mm caudal of Bregma). For single cell dendritic imaging a low titer Cre -virus (AAV1-CamkII-Cre, 1.5x10$_8$ GC/mL, all virus from University of Pennsylvania Vector Core) was injected (1 injection of ~30 nL at a depth of ~1250 µm below the dural surface using a beveled glass micropipette: ~1-2 MΩ after beveling) in combination with a high titer of flexed-GCaMP6 virus ((Chen, Wardill et al. 2013) AAV1-Syn-flex-GCaMP6f or s, 1.4x10$_{13}$ GC/mL) leading to expression of GCaMP-6 in a sparse CA1 pyramidal neuron population. For population imaging, dense labeling was performed the same as sparse except only AAV1-Syn-GCaMP6f (1.5x10$_{13}$ GC/mL) was injected. For interneuron SOM+ or PV+ axon imaging, we injected a high titer of flexed-GCaMP6f virus (AAV1-Syn-flex-GCaMP6f, 1.4x10$_{13}$ GC/mL, ~30 nL) into the hippocampus of SOM+ or PV+ cre mice. Mouse water scheduling began the day after virus injections (0.8-1.0 mL/day, and continued through all training and experiments) followed ~7 days later by a hippocampal window and head-plate implantation surgery (as described in ((Dombeck, Harvey et al. 2010)). For live slice imaging and glutamate uncaging experiments, mice were injected following the same sparse labeling protocol and allowed to recover for 3 to 4 weeks prior to hippocampal slice preparation.

Behavior and virtual reality switching

We used the same virtual reality and treadmill set-up as previously described (Heys, Rangarajan et al. 2014), consisting of a 1D treadmill and a view angle within the virtual environment straight down the track. Training in a 3 m virtual linear track (F1; Figure 2.1; one ~40-60 minute session per mouse per day) began ~7 days after window implantation and continued until mice routinely ran along F1 to achieve a high reward rate (>~2 rewards/minute); rewards in F1 consisted of water (4 µl) delivered as described previously (Dombeck, Harvey et al. 2010). Mice were teleported back to the beginning of the track after each reward and after a short (1.5 sec) delay. Once this criterion was reached (~5-7 days of virtual reality training in F1), imaging commenced the following day (experimental day 1). Figure 2.1A shows the experimental timeline that each mouse underwent. Experimental day 1 consisted of mice running at least 15 laps in F1, at which point the virtual environment was switched to a novel environment (N1). This VR switch occurred rapidly (~33ms) and was triggered while mice were at the start of the F1 track. Rewards in N1 were delivered at the end of the track as in F1, but consisted of 8 µl instead of 4 µl water rewards. Mice were then allowed to traverse the track for at least 20 laps before being placed back into their home cage. 24 hours later, on experimental day 2, mice were placed back into the same environment, N1, and allowed to traverse the track for at least 20 laps. This environment was now considered familiar, F2, at which point the environment was switched to a second novel environment, N2. Water rewards in N2 were 8 µl, and mice completed at least 20 laps before being placed in their home cage. 24 hours later, on experimental day 3, mice were placed back in N2 and completed at least 15 laps, at which point N2 was considered familiar, F3. Data from the two familiar environments prior to VR switch, F1 and F2, were grouped together and referred to as F throughout the main text and figures. Data from the two novel environments following VR switch, N1 and N2, were grouped together and referred to as either N throughout the main text and figures. No differences in the results reported here were observed between the first switch (F1 to N1) and the second switch (F2 to N2), justifying their grouping.

Two-photon imaging

A Moveable Objective Microscope (Sutter Instruments) was customized for our imaging experiments. The microscope consisted of a resonant scanning module (Thorlabs), a 40×/0.80 NA water immersion objective (LUCPlanFL N, Olympus) and enhanced collection optics. Green GCaMP6 fluorescence was routed to a GaAsP PMT (H10770PA-40) using a series of dichroic mirrors and band-pass filters (in order after leaving the back aperture; Semrock): FF665-Di02 long pass dichroic, FF01-680/sp short pass filter, FF560-Di01 long pass dichroic, FF01-510/84 band-pass filter. Stray light from the virtual reality monitor was blocked using a custom box surrounding the top of the microscope objective and the overlying dichroic mirror (not including the tube lens, scan lens, galvos or routing mirrors). This box had one hole on top, for entry of the excitation beam, which was covered with a color glass filter (FGL780, Thorlabs) and one hole on bottom for the microscope objective. This bottom hole was sealed using the same loose black rubber tube and tight fitting metal rings described previously (Dombeck, Harvey et al. 2010). ScanImage 4 was used for microscope control and acquisition (Pologruto, Sabatini et al. 2003).

Ti:Sapphire laser (Chameleon Ultra II, Coherent) light at 890 (for GCaMP6s) or 920 (for GCaMP6f) nm was used as the excitation source. Laser average power at the sample (after the objective) was 70–100 mW. A pockels cell (350-80-LA-BK-02, 302RM driver, Conoptics) was used to blank laser excitation at the edges of the field of view. Time-series movies (1024 or 512x256 pixels) were acquired at 50 Hz for single plane (population and interneuron axon imaging), 25 Hz for 2 plane and 12.5 Hz for 4 plane (dendrite imaging using an electric lens, see (Sheffield and Dombeck 2015)) acquisitions. A Digidata1440A (Molecular Devices) data acquisition system was used to record (Clampex 10.3) and synchronize position in the linear track, reward timing, and two-photon image frame timing.

Image processing

Time-series movies for multi-plane recording were acquired using interleaved frames (i.e. every other frame was from the same plane for 2-plane imaging). The electric lens settling time of ~5 ms sometimes created distortions in the first few lines of each frame of the movie; these lines were therefore removed before subsequent analysis. Each multi-plane time-series was then split into separate time-series movies, one for each acquired plane. Each single-plane time-series, including those from population imaging, was then independently motion corrected using whole frame cross-correlation, as described previously (Dombeck, Harvey et al. 2010, Miri, Daie et al. 2011, Sheffield and Dombeck 2015). To decrease the motion correction time and increase the stability of the motion corrected movie, all time series movies from multiplane and single plane acquisitions were cropped in the x and y dimensions around an area containing structures with high baseline fluorescence that changed little throughout the movie. The x and y shifts for each frame calculated from the cropped movie was then applied to the original non-cropped movie.

These motion corrected movies were then used for subsequent analysis. After time-series imaging, z series were acquired from each field of view from the external capsule fiber surface through the proximal apical dendrite.

ROI selection and calcium transient analysis

For single cell imaging (sparse labeling) ROIs were selected by hand on the mean soma or dendrite images (mean time projection of all frames in the motion corrected time-series at each plane). ROIs were drawn to closely follow the outline of the structure of interest (soma or dendrite). Dendrites belonging to the co-imaged parent soma were identified offline by tracing them to the soma in the z series; additional verification was provided by their often co-occurring significant calcium transients with the soma.

For interneuron axon imaging in the Stratum Oriens (SOM+ mice) and pyramidal cell layer (PV+ mice), ROIs were selected by hand around an area containing a high density of axons in the image, avoiding somata and dendrites and minimizing areas with an absence of structure.

For population imaging, ROIs were defined as previously described (Mukamel, Nimmerjahn et al. 2009) (mu = 0.6, 150 principal components, 150 independent components, s.d. threshold = 2.5, s.d. smoothing width = 1, area limits = 100-1200 pixels). As seen previously (Dombeck, Harvey et al. 2010), ROIs nearly always defined single cell regions. To calculate the average population ΔF/F (Figure 2.4A and B), we selected a single ROI encompassing the entire FOV.

From dendrite and population time-series, ΔF/F versus time traces were generated for each ROI as previously described (Dombeck, Harvey et al. 2010). Briefly, slow changes in the fluorescence traces were removed by examining the distribution of fluorescence in a ~6 sec interval around each sample in the trace and normalized by the 8th percentile value. These baseline corrected soma and dendrite fluorescence traces were then subjected to the analysis of the ratio of positive to negative going transients of various amplitudes and durations described previously (Dombeck, Khabbaz et al. 2007). We used this analysis to identify significant transients with < 0.01% (< 0.001% for dendrites) false positive error rates; these identified significant transients were used in the subsequent analysis.

The somatic ΔF/F traces consisted of a baseline interrupted periodically by calcium transients of varying amplitude, consistent with a difference in the number of underlying APs, and varied in duration, consistent with the summation of multiple transients (Dombeck, Harvey et al. 2010, Sheffield and Dombeck 2015). Dendritic calcium transients were consistent with those observed previously (Sheffield and Dombeck 2015).

To avoid subtracting any slow changes in the fluorescence traces from interneuron axons, which have a baseline firing rate that could slowly vary with behavior and cause slow changes in fluorescence, time-series ΔF/F traces were generated for each ROI by examining the distribution of fluorescence from the entire trace and normalizing each sample in the trace by the 8th percentile value (i.e. no removal of slow baseline variations). Measurements of ΔF/F in Figure 4 are calculated from these baseline corrected traces.

Behavior analysis

To calculate mean lap virtual velocity (Figure 2.2B; Figure 2.7C and I) for each lap, we divided the track length (3 m) by the time taken to traverse the track. Stopping periods or slow moving periods were included in this measure. To calculate stopping probability on each lap, we used an instantaneous virtual velocity threshold of 1 cm$_{-s}$. If instantaneous virtual velocity fell below this threshold for at least 100 ms, we considered this a stopping period, and the probability of stopping on that lap was given a value of 1, regardless of whether additional stopping periods occurred on that lap. The lap stopping time was calculated from these stopping periods, and if mice stopped multiple times on a single lap, the total time stopped was summed together from each stopping period on that lap. We used the same virtual velocity threshold to classify running versus resting behavior (Figure 2.7B and H).

Defining place fields

Place fields were identified and defined as described previously (Dombeck, Harvey et al. 2010) with minor changes outlined below. Place fields were defined solely based on somatic calcium transients. First, long running periods were defined in which mouse movement along the virtual track consisted of virtual velocity >~7 cm$_{-s}$ and run length >40 cm without hitting the end of the track. The mean somatic $\Delta F/F$ was calculated as a function of virtual track position for 150 position bins and this mean fluorescence versus position plot was then averaged over 3 adjacent points. Potential place fields were first identified as contiguous regions of this plot in which all of the points were greater than 25% of the difference between the peak somatic $\Delta F/F$ value (for all 150 bins) and the baseline value (mean of the lowest 20 out of 150 somatic $\Delta F/F$ values). These potential place field regions then had to satisfy the following criteria: 1. The field must be >20 cm in width, 2. The field must have one value of at least 10% mean $\Delta F/F$, 3. The mean in field $\Delta F/F$ value must be >4 times the mean out of field $\Delta F/F$ value and 4. Significant calcium transients must be present >40% of the time the mouse spent in the place field. Potential place field regions that met these criteria were then defined as place fields if their p-value from boot strapping was < 0.05, as described previously (Dombeck, Harvey et al. 2010). These place fields were then treated independently, and transients that occurred outside of the defined place field region were removed for analysis of each specific field. The resultant place field was then used in all subsequent analysis. Place cells with multiple potential place field regions were treated in the same way, with each potential place field region treated independently and subjected to the same tests as above, except the mean out of field ΔF/F value excluded ΔF/F values from other potential place field regions. We only included place fields in which neither edge of the identified field was at the track start or track end.

Place field spatial correlation

To measure place field spatial correlation across environments, we found place cells that had place fields in both environments and compared their mean place fields. Each place field pair to be compared was split into 150 position bins (2cm/bin) from which we calculated a Pearson's correlation coefficient, our measure of spatial correlation between 2 place fields. To measure place field spatial correlation within environments, we first divided the session up into two halves based on the total number of laps completed within the session. We calculated a mean place field from transients that occurred within the first half of all the laps in that session, and a second mean place field from transients that occurred within the second half of that session. These two place fields then underwent the same spatial correlation test as above.

Place field onset lap

To determine place field onset lap (Figure 2.2E,F, 2F), starting on lap 1 we searched for a significant somatic ΔF/F calcium transient present within the boundaries of the previously determined mean place field calculated from all the laps in the session. If one were found we would then search for somatic ΔF/F calcium transients on each of the next 5 laps. If 4 of the 6 laps had somatic ΔF/F calcium transients within the mean place field boundaries, lap 1 would be considered the place field onset lap. If either lap 1 had no somatic ΔF/F calcium transient or less than 4 of the 6 laps had somatic ΔF/F calcium transients, we would move to lap 2 and repeat the search.

To determine place field onset lap in F (Figure 2.2F2), we trained a separate set mice as described above. In these mice, on experimental day 1, we began imaging the CA1 population prior to the first traversal of F on that day (this imaging procedure was repeated for the data acquired in Figure 2.4C-J).

***In vivo* dendrite analysis**

Identification of branch spikes, definition of branch spike prevalence (Figure 2.3) and analysis of dendritic area of significant ΔF/F increase (Figure 2.6 and Figure 2.5) was the same as previously described (Sheffield and Dombeck 2015). Additionally, significant dendrite localized calcium transients had to consist of at least 2 contiguous samples in the trace to be included. To prevent calcium transients from dendrites belonging to other cells in the FOV from potentially contaminating our dendrite ΔF/F traces, we excluded from analysis periods when other cells in the FOV had significant somatic calcium transients. This step likely leads to missing some dendrite localized calcium transients, but eliminates false positives caused by calcium transients from other neurons.

Track location of dendrite localized transients (Figure 2.6D) was determined by finding the track location where the peak of the dendritic transient occurred. We then calculated the track distance between this location and the location of the mean somatic place field’s weighted center of mass (see (Sheffield and Dombeck 2015)). This distance was then normalized by the mean somatic place field width in each case.

We imaged both GCaMP6f-expressing (n = 12 place fields) and GCaMP6s-expressing dendrites (n = 6 place fields). Imaging at 920 nm, we found the baseline fluorescence signal in the GCaMP6s-expressing dendrites was oftentimes undetectable. Since unbound GCaMP6s emission is larger when excited by shorter wavelengths, we used 890 nm for all imaging experiments using GCaMP6s. This increased the signal from dendrites at rest, but resulted in reduced ΔF/F transient amplitudes. Dendrite localized calcium transient max amplitudes during the delay period were therefore smaller in GCaMP6s-expressing dendrites compared to GCaMP6f-expressing dendrites (GCaMP6s amplitudes: 114.6 ± 25.6 % ΔF/F vs. GC6f amplitudes: 224.2 ± 25.1 % ΔF/F, t-test, p = 0.0002). However, the number of dendrite localized calcium transients detected during the delay period was similar (GCaMP6s: n = 14; GCaMP6f: n = 16), and the transient durations (defined by the full width half max of the significant transients) were also not significantly different (GCaMP6s duration: 230.8 ± 8.1 SEM ms vs. GCaMP6f duration: 186.4 ± 13.7 SEM ms, t-test, p > 0.05). The branch spike prevalence numbers and the dendrite-localized transients reported consisted of recordings from both GCaMP6s and GCaMP6f-expressing dendrites.

To calculate the spatial extent of dendrite localized calcium transients from the high-resolution movies of single dendritic branches *in vivo* and *in vitro* (Figure 2.5C and D), we measured along the length of the dendrite from one edge to the other of the region containing contiguous significant pixels.

NMDA receptor knockdown

Grin1$_{lox/lox}$ (B6.129S4-*Grin1*$_{tm2Stl}$/J) mice (Tsien, Huerta et al. 1996) were injected with a high titer Cre -virus (AAV1-CamkII-Cre, 1.5x10$_8$ GC/mL) in combination with a high titer of flexed-GCaMP6 virus (AAV1-Syn-flex-GCaMP6f) leading to expression of GCaMP-6f in a dense CA1 pyramidal neuron population and knockdown of functional NMDA receptors in the same cells expressing GCaMP6f. Imaging of these neurons began ~3 weeks later to ensure sufficient knockdown of NMDA receptors (Chu, Atherton et al. 2015). For sparse labeling of CA1 pyramidal neurons in Grin1 mice we replicated the method used to obtain sparse labeling in wildtype mice: a low titer Cre -virus (AAV2/1-CamkII-Cre, 1.5x10$_8$ GC/mL) injected in combination with a high titer of flexed-GCaMP6f virus (AAV1-Syn-flex-GCaMP6f, 1.4x10$_{13}$ GC/mL) leading to sparse expression of GCaMP-6f and knockdown of functional NMDA receptors in the same cells expressing GCaMP6f. We also waited at least 3 weeks before imaging these neurons to ensure NMDA receptor knockdown. The Grin1 mice required ~1 week more training in F1 to reach behavior criterion (>~2 rewards/minute) compared to wild type mice.

NMDA receptor knockdown immunohistochemistry

Grin1$_{lox/lox}$ mice expressing GCaMP6f and Cre in dorsal hippocampal pyramidal neurons were anaesthetized with isoflurane and perfused with phosphate buffered saline (PBS, pH = 7.4) followed by fixation with 4 % paraformaldehyde in PBS. Brains were removed and post-fixed in the same fixative at 4°C overnight, then stored at 4°C in 30% sucrose/PBS solution. Coronal sections (40 µm) were prepared using a freezing microtome, washed three times with tris-buffered saline (TBS; pH = 7.6) for 10 minutes and then incubated with blocking solution (5% normal goat serum, 0.3% Triton X-100 in 1x TBS) for 2 hours at room temperature. The primary antibody (rabbit polyclonal anti-GluN1 IgG, abcam, ab17345; 1:200) was diluted in blocking solution and slices were treated overnight at 4°C. The next day, slices were washed with TBS buffer three times and incubated with diluted secondary antibody (Alexa 594 goat anti-rabbit IgG, 1:500) for 2 hours at room temperature. Slices were washed with TBS buffer three times and then mounted on glass slides in VECTASHIELD (Vector labs, H-1000). Fluorescence images were acquired using an automated slider scanner (VS120 virtual Slide, Olympus).

Hippocampal slice preparation

Transverse hippocampal slices (~300 µm) were prepared from virus injected male C57BL/6 mice (see **Mouse surgery and stereotaxic virus injections**) using a vibrating microtome (VT1200S; Leica Systems, Germany). Animals were anaesthetized with isoflurane and perfused with ice-cold sucrose artificial cerebrospinal fluid (ACSF) solution containing (in mM) 85 NaCl, 2.5 KCl, 1.25 NaH_2PO_4, 25 $NaHCO_3$, 25 glucose, 75 sucrose, 0.5 $CaCl_2$, and 4 $MgCl_2$, saturated with 95% O_2 and 5% CO_2. After slices were made they were transferred to a warmed (32 °C) incubation chamber with bubbled ACSF consisting of 125 mM NaCl, 2.5 mM KCl, 25 mM NaHCO3, 1.25 mM NaH2PO4, 1 mM MgCl2, 2 mM CaCl2 and 25 mM glucose for 25 min, after which they were allowed to recover at room temperature in oxygenated ACSF for 1 hour before imaging.

In vitro imaging and glutamate uncaging

Glutamate uncaging and imaging of hippocampal CA1 basal dendrites *in vitro* were performed on an Ultima two-photon laser scanning microscope (Bruker, former Prairie Technologies, Middleton, WI) equipped with duel galvanometers driving two Ti:Sapphire lasers (Chameleon, Coherent). The lasers were tuned to the wavelength of 920 nm and 720 nm for imaging and uncaging, respectively, and the intensity of each laser was independently controlled with electro-optical modulators (Conoptics). Images were acquired with an upright Zeiss Axiovert microscope using a 40x, 1.0 numerical aperture water immersion objective. During imaging and uncaging, slices were maintained at a constant temperature ranging from 30–34 °C (mean 32.1 °C and bathed in recirculating bubbled ACSF containing 3 mM MNI-caged L glutamate (4-methoxy-7-nitroindolinyl-caged L-glutamate, Tocris), 1 μM TTX (Tocris Bioscience) and 2 uM of GABA$_A$ receptor antagonist SR-95531 (Tocris Bioscience). MNI-glutamate was uncaged using 500 μs pulses (28-64 mW after the objective) onto varying sequences of 1 to 8 spines with a 120 μs interstimulus interval (all inputs within 5 ms) to evoke local dendritic calcium transients. Uncaging power was adjusted, based on the depth of the dendritic branch, to be in the range of powers previous research has demonstrated generate a post synaptic potential mimicking presynaptic activation with bath applied MNI-glutamate (Bloodgood, Giessel et al. 2009, Seong, Behnia et al. 2014). Time-series movies were acquired at ~ 30 Hz for the duration of uncaging events and were analyzed with MATLAB (MathWorks) and ImageJ following motion correction (see ROI selection and calcium transient analysis). Multiple ROIs were selected for each dendrite by hand and consisted of a ROI encompassing all the pixels with a significant ΔF/F increase at the peak of the transient (Sheffield and Dombeck 2015) as well as a small ROI drawn on the shaft (~ 1 um) that was a least 2 spine widths away from the closest uncaging site and another similar sized ROI drawn at the center of each dendritic area of significant ΔF/F increase. These various ROIs were intended to approximate the various sampling cross sections of the dendritic regions that would be expected from the *in vivo* imaging geometry. ΔF/F versus time traces were generated for each ROI as previously described (Dombeck, Harvey et al. 2010).

QUANTIFICATION AND STATISTICAL ANALYSIS

Data was analyzed on a Dell Power Edge 720 Server using ImageJ (Version 1.47) and custom software written in MATLAB (Version R2012a and Version R2013b). No statistical methods were used to predetermine sample sizes. Data collection and analysis were not performed blind to the conditions of the experiments. Paired and Unpaired t tests, repeated measures ANOVA with Tukey's post-test, Wilcoxon rank test and Chi squared test for proportional difference were used to test for statistical significance when appropriate. Statistical parameters including the exact value of n, precision measures (mean ± SEM) and statistical significance are reported in the text and in the figure legends (see individual sections). The significance threshold was placed at $p < 0.05$.

Experiments described in Chapter 2 have been published as:

Sheffield, M. E. J., Adoff, M.D., Dombeck, D.A. (2017). "Increased Prevalence of Calcium Transients across the Dendritic Arbor during Place Field Formation." Neuron **96**(2): 490-504 e495.

Chapter 3 - Methodology for subcellular dendritic imaging in vivo

3.1 Summary

Understanding how synaptic inputs are integrated and converted into action potential output is essential to understanding how the brain computes and stores information. Advances in the development of genetically encoded indicators of neuronal activity have revolutionized our ability to monitor synaptic transmission in vivo with a level of spatiotemporal detail inconceivable a decade prior (Lin and Schnitzer 2016). Dendritic spines contain various glutamatergic calcium-permeable channels which are activated by presynaptic glutamate release. Activation of these receptors results in local depolarization and subsequent influx of calcium ions which are localized to the spine head (Grienberger, Chen et al. 2015). The spine isolated calcium transients seen in vivo are considered a correlate of synaptic activation and primarily depend on calcium influx through NMDA receptors, with some contribution from voltage gated calcium channels (Bloodgood and Sabatini 2007, Chen, Leischner et al. 2011). For this reason, calcium imaging using genetically encoded calcium indicators remains the most widely used approach for measuring synaptic activity in vivo.

3.2 Indicators of synaptic release

3.2.1 GCaMP

Genetically encoded calcium indicators (GECIs) generally come in two variations, those involving Förster resonance energy transfer (FRET) and those with a single-fluorophore backbone. A prime example of the single-fluorophore GECIs is the GCaMP family, which is currently one of the most sensitive and widely used calcium indicators available. GCaMP is expressed cytosolically and consist of a circularly permuted enhanced green fluorescent protein (EGFP), sandwiched between the calcium-binding protein calmodulin on one side and the calmodulin-binding peptide M13 on the other side (Nakai, Ohkura et al. 2001). Binding of calcium elicits conformational changes in the fluorophore leading to an increase in emitted fluorescence. The biochemical and optical properties of the latest generation of GECIs match and in some respects surpass synthetic calcium dyes such as OBG-1 (Chen, Wardill et al. 2013). By selectively labeling sparse populations using FLEXED-GCaMP6s AAV and CRE recombinase, it is now possible to chronically monitor spine calcium signals following synaptic activation in live animals (Chen, Wardill et al. 2013, Wilson, Scholl et al. 2018). Using this method, I was able to record calcium activity from dendritic spines of CA1 place cells sparsely labeled with GCaMP6s in mice navigating a virtual reality linear track (Fig.3.1).

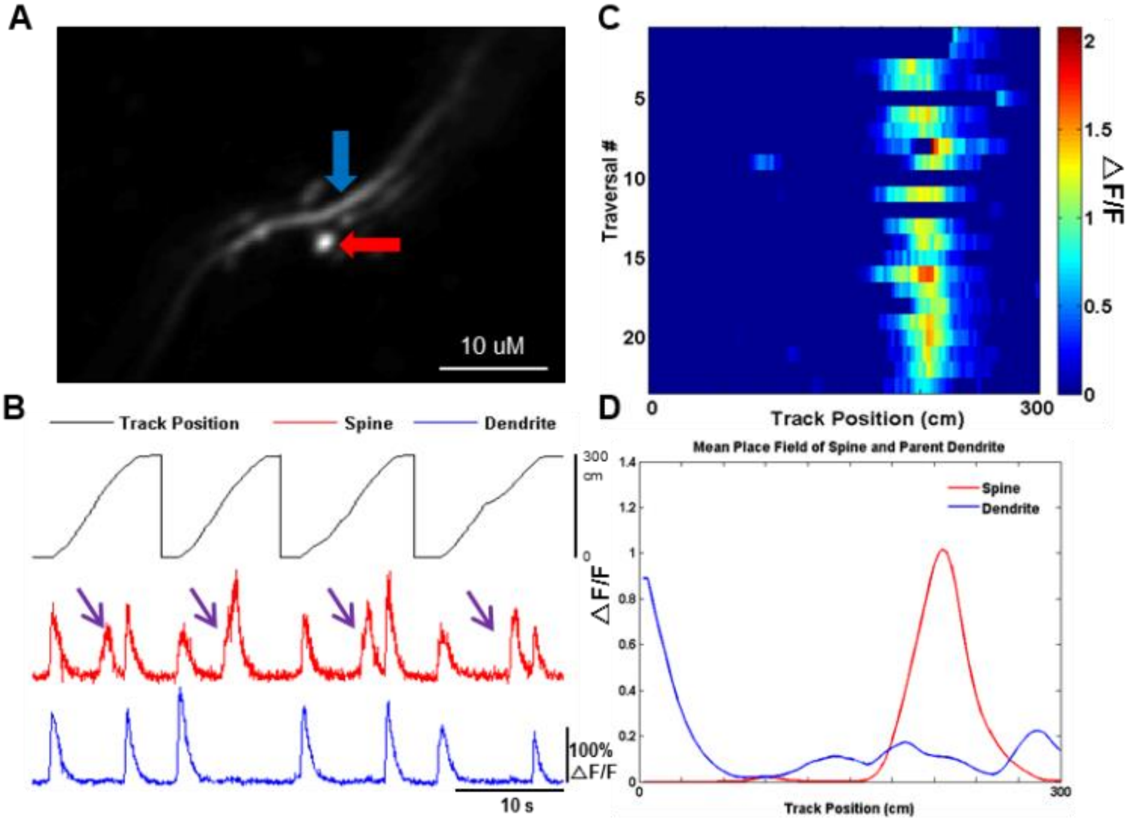

xii Figure 3.1: Calcium imaging of basal dendritic spines during navigation of virtual linear track

A. Example of dendritic focal plane from imaging session during behavior. Scale bar 10 um. Red arrow indicates Spine analyzed, blue arrow indicates dendritic branch analyzed.

B. Fluorescence traces from spine (red) and adjacent dendritic branch (blue), top trace indicates animal's position on the track (black) purple arrows indicate localized spine transients.

C. Heat map of mean change in fluorescence for spine during each traversal.

D. Mean place field of dendrite superimposed over spine place field.

3.2.2 Complications with GCaMP imaging

Yet there are several drawbacks and complications inherent to imaging with GCaMP which influence interpretations of spine calcium imaging. Observable increases in spine calcium are dependent on the opening of NMDARs or voltage-dependent calcium channels and thus basal synaptic transmission may fail to trigger detectable changes in spine calcium levels. Hence GCaMP would report only those synaptic activations that are sufficiently strong to relieve the magnesium block. This is further supported by experiments using glutamate uncaging onto dendritic spines of CA1 pyramidal neurons sparsely expressing GCaMP6s in mouse brain slices. Single stimulations at a laser power shown to mimic mEPSPs results in very few evoked localized spine transients. Temporally concurrent stimulations on the same spines resulted in calcium events in both the stimulated spines and nearby dendritic shaft. (Fig.4.2).

The calcium transients that occur in dendritic spines can be caused by dendritic branch spiking events or synaptic activation or both. These dendritic events invade all visible pixels of the recorded branch (both spines and shaft) and are due to either back-propagating action potentials (bAPs) or dendritically evoked spikes. Synaptic input-induced calcium transients in the spines can be obscured by the co-occurrence of these dendritic branch transients during somatic firing, further complicating the detection and isolation of input-specific spine activity.

Previous studies have attempted to circumvent this problem by restricting their analysis to neurons with low activity and isolating the input-specific signals by post-hoc removal of transients that co-occur in the shaft and spine using a subtraction procedure(Chen, Wardill et al. 2013, Wilson, Whitney et al. 2016, Iacaruso, Gasler et al. 2017). Any spines displaying a significant correlation with the dendritic signal following this subtraction procedure were subsequently excluded from further analysis. These signals may include the large dendritic responses that result from the clustering of synaptic inputs, limiting the utility of this approach for detecting the strongest events. Additionally, this approach is of relatively limited use when trying to empirically identify the quantity of inputs specifically contributing to place cell firing, which often co-occurs with bAPs or global dendritic signals. It was recently shown that this subtraction approach produces biased estimates of correlations between nearby spines because the depolarization required for calcium influx in one compartment also acts on nearby compartments(Kerlin, Boaz et al. 2019). The subtraction procedure also does not account for differences in the decay times of bAP-generated transients in the soma compared to the dendrites. Systematic errors in subtraction can lead to an inaccurate depiction of the organization of task-related calcium signals in the dendrite through the over or underestimation of spine selectivity (Kerlin, Boaz et al. 2019). Because of these challenges in detecting the strongest and weakest activations, care needs to be taken with how synaptic calcium signals are interpreted(Ali and Kwan 2020). To circumvent these issues associated with GCaMP I turned to other available means of optically recording synaptic activity.

3.2.3 iGluSnFR

Glutamate is the most abundant excitatory neurotransmitter in the mammalian nervous system and plays a pivotal role in chemical neurotransmission between neurons. Following the arrival of an action potential, glutamate is released from presynaptic terminals through the fusion of neurotransmitter-containing vesicles. Once released, glutamate molecules diffuse across the synaptic cleft and bind to glutamate receptors located on postsynaptic neurons (Clements 1996). With the development of the genetically encoded sensor for glutamate (iGluSnFR)(Marvin, Borghuis et al. 2013) it is now possible to directly visualize synaptic glutamate release providing a powerful approach for monitoring neuronal communication and information processing in vivo (Borghuis 2019). iGluSnFR is constructed from the periplasmic glutamate/aspartate-binding protein cloned from *E. coli* Glt1 and circularly permutated (cp) GFP. When glutamate binds to the glutamate-binding domain of Glt1 it induces a conformational change, which shifts the cpGFP group from a quenched to an unquenched highly fluorescent state (Marvin, Borghuis et al. 2013, Lin and Schnitzer 2016). iGluSnFR expression is not selectively targeted to synapses but rather is expressed throughout the plasma membrane with the ligand-binding domain and fluorescent group located extracellularly. iGluSnFR senses glutamate in the extracellular space and reports increases in extracellular glutamate concentration through increasing fluorescence, in a manner independent of post-synaptic strength (Soares, Lee et al. 2017). Thus, as opposed to calcium imaging, the iGluSnFR signal provides no information about level of activation of the postsynaptic neuron.

The extracellular glutamate concentration following the release of a single synaptic vesicle into the synaptic cleft has been estimated to reach a about 1.1 mM before rapidly decaying (~ 1 ms) through diffusion and reuptake (Clements, Lester et al. 1992, Diamond and Jahr 1997). While the affinity (~ 4 uM) and brightness of the original version of iGluSnFR put it in the physiologically relevant range for glutamate detection of single release events, its' dim emission profile and propensity to photobleach with laser powers normally used for in vivo imaging limited its utility for imaging in behaving animals over longer timescales. iGluSnFR was recently improved through the development of a range of iGluSnFR variants of different affinities and kinetics. The baseline fluorescence was also improved by substituting the original GFP backbone with a circularly permuted superfolder GFP leading to improved brightness and stability(Marvin, Scholl et al. 2018). The increased affinity and greater $\Delta F/F$ of the high-affinity variant SF-iGluSnFR.A184S makes it a promising alternative to in vivo spine calcium imaging. Evidence for this can be seen in recent work in the ferret visual cortex where SF-iGluSnFR.A184S lead to improved detection of robust spine-localized glutamate events enabling for the identification of orientation-selective responses in individual dendritic spines (Marvin, Scholl et al. 2018). Since SF-iGluSnFR.A184S and NMDA receptors have a similar glutamate binding affinity (SF-iGluSnFR.A184S: 0.6 μM; High-affinity NMDA receptors: 1 μM)(Clements 1996, Marvin, Scholl et al. 2018), this indicator provides means to investigate the amount and source of glutamate input to CA1 dendrites and its relevance to synaptic cooperativity.

3.3 Methods and technical considerations for in vivo subcellular optical imaging

Presently, few methods exist for recording and measuring the anatomical organization and functional properties of individual dendritic synapses during behavior. While electrophysiological recordings remain the gold standard for assessing synaptic transmission and signal processing at subcellular scale, the lack of spatial resolution, inability to chronically record, and low-throughput nature inherent to this approach makes it unsuitable for probing the activity of dendrites and spines in behaving rodents. For this reason, in vivo 2P imaging exists as the only known technique capable of probing synaptic activity in vivo at the single-synapse scale. Until recently, most in vivo imaging studies have been restricted to the study of spine morphology due to the difficulty of imaging functional activity from fine dendrites and spines in awake behaving animals (Grienberger, Chen et al. 2015).Motion artifacts resulting from brain motion can cause spines to move out of focus during imaging, while photodamage as a result of high laser power can negatively affect cellular health. Additionally, visualizing spine activity requires sufficiently high sampling rates as to achieve the necessary signal-to-noise ratio for resolving these small structures (Chen, Leischner et al. 2012). Motion artifacts resulting from brain movements during animal locomotion are a major impediment to imaging functional activity from fine dendrites and spines in behaving animals. These movement-induced artifacts are exacerbated by poor surgical technique and often cannot be corrected for with offline motion correction algorithms. To reduce the prevalence of these artifacts during imaging I optimized the hippocampal window surgery to maximize the mechanical stability of the imaging window. This involved increasing the amount of sealant used to hold the window in place and altering the size of the craniotomy hole to further stabilize the window. By refining and improving the window surgery procedure I was able to minimize the prevalence of these large motion artifacts and can now reliably image dendritic branches with single spine resolution in the awake, behaving animal.

Photo-damage and bleaching can occur from the relatively high laser power necessary to image small and dim subcellular structures. Photo-damage negatively impacts cell health and can result in dendritic blebbing at the area of interest while bleaching can attenuate the amplitude of spine-localized calcium or glutamate transients and lead to further dimming in subcellular structure. By assessing the extent of photodamage and photobleaching inflicted by altering the laser intensity and imaging wavelength I determined the maximum laser power at which we can image to maintain cell health and reduce bleaching to acceptable levels.

Both the imaging frame rate and the properties of the fluorescent indicator can have a significant effect on signal to noise. Faster imaging speeds can aide in the detection of shorter duration events but may also increase noise levels. By varying the frame acquisition rate during imaging, I determined which imaging speed provided the best signal for imaging glutamate activity. The variants of iGluSnFR differ in their kinetics and sensitivity, and thus may vary in their ability to detect changes in extracellular glutamate concentration in vivo. To investigate the detection efficiency of glutamate transients with SF-iGluSnFR.A184S, I compared the rate of events detected with SF-iGluSnFR.A184S to the expected number of synaptic events based on the anatomical and functional properties of CA3 neurons in vivo (see chapter 3 methods for details) and found they were in agreement (~0.10 vesicles/(sec*µm) vs ~0.17 vesicles/(sec*µm)). Using these optimized parameters, I was able to reliably record glutamate activity from dendritic branches of CA1 place cells sparsely labeled with SF-iGluSnFR.A184S in mice navigating a virtual reality linear track. After demonstrating the feasibility of this approach, I next sought to determine whether synaptic inputs are clustered or distributed throughout the dendritic arbor of CA1 place cells in the intact brain of a behaving animal by using iGluSnFR and the red-shifted calcium indicator jRGECO1a to measure glutamatergic and somatic calcium activity from the same neuron. Results from these experiments are detailed in Chapter 4.

Chapter 4 - The functional organization of excitatory synaptic input to place cells

4.1 Summary

Hippocampal place cells increase their firing when animals traverse a particular region of the local environment and as an ensemble, form an internal spatial representation known as the cognitive map. This map is thought to underlie the ability of animals to navigate within their environments and form and retrieve spatial memories. However, the neural mechanisms underlying the generation of place firing have remained a mystery. The current, most widely accepted model posits that place cells receive excitatory inputs with tuning curves that together tile all spatial locations, and that input-potentiating post-synaptic plasticity mechanisms select which inputs drive firing. Further, many models predict that the functional dendritic organization of excitatory input contributes to place firing through recruitment of super-linear dendritic summation. A key missing piece of the puzzle to test these models is knowledge of the pattern of excitatory synaptic input received by place cells (direct measurements of the excitatory inputs across the dendritic arbor that drive place firing). As such data is missing across all brain regions and neuron types during behavior, it is currently unknown what pattern of synaptic inputs underlie behaviorally relevant neural firing.

We developed new optical recording methods that allowed us to gather and analyze exactly this type of data, providing the first measurements of the pattern of synaptic inputs underlying a cognitive representation during behavior. We used resonant scanning two-photon microscopy to record dendritic glutamate input to place cells (from presynaptic partners) using a new variant of a fluorescent genetically encoded glutamate sensor (iGluSnFR). Through extensive calibration, we show that our methods provide micron-scale dendritic spatial resolution and single excitatory vesicle detection efficiency in CA1 place cells of mice navigating along

virtual linear tracks. We found that dendrites of individual place cells received significant excitatory input at locations both inside and outside of the somatic place field. Many micron-scale dendritic regions of interest (ROIs) received highly spatially tuned excitatory input (place-ROIs), while other regions received input with little spatial tuning or no detectable input. Surprisingly, and contrary to the current widely accepted model, the total excitatory input across all dendritic ROIs was greater in the somatic place field versus outside, and this increased excitation mainly arose from place-ROIs with spatial tuning overlapping the somatic field. Finally, we found that excitatory input to place cell dendrites displayed functional clustering on the ~10 µm scale and this clustering was more pronounced in the somatic place field versus outside. Our results implicate increases in total excitatory input and super-linear dendritic summation in CA1 place field firing, indicating that post-synaptic strength is not the sole determinant of field location, as is currently thought. Further, our finding that CA1 place cells largely inherit their fields from upstream synaptic partners with similar fields, suggests that these cells are part of multi-brain-region cell assemblies forming representations of specific locations.

4.2 Introduction

Hippocampal place cells encode an animal’s location in its environment through somatic action potential firing in discrete place fields(O'Keefe and Dostrovsky 1971). Current models posit that these cells receive excitatory inputs with tuning curves that together tile all spatial environment locations, and that potentiating post-synaptic plasticity mechanisms select which inputs drive firing(Burgess and O'Keefe 1996, Lee, Lin et al. 2012, Bittner, Grienberger et al. 2015, Bittner, Milstein et al. 2017, Weber and Sprekeler 2018, Sheffield and Dombeck 2019, Zhao, Wang et al. 2019). Some models also predict that the functional dendritic organization of excitatory input contributes to place firing through recruitment of super-linear dendritic summation(Golding, Staff et al. 2002, Lee, Lin et al. 2012, Sheffield, Adoff et al. 2017, Sheffield and Dombeck 2019). However, the pattern of excitatory synaptic input leading to place field firing is unknown. Therefore, here we used resonant scanning two-photon microscopy (2P) to record dendritic glutamate input with micron-scale spatial resolution and single vesicle detection efficiency in CA1 place cells of mice navigating along virtual linear tracks. Dendrites of individual place cells received significant excitatory input at track locations both inside and outside of the somatic place field. Many micron-scale dendritic regions of interest (ROIs) received highly spatially tuned excitatory input (place-ROIs), while other regions received input with little spatial tuning or no detectable input. Contrary to current widely accepted models(Burgess and O'Keefe 1996, Lee, Lin et al. 2012, Bittner, Grienberger et al. 2015, Bittner, Milstein et al. 2017, Weber and Sprekeler 2018, Sheffield and Dombeck 2019, Zhao, Wang et al. 2019), the total excitatory input across all dendritic ROIs was greater in the somatic place field versus outside, and this increased excitation mainly arose from place-ROIs with spatial tuning overlapping the somatic field. Finally, excitatory input to place cell dendrites displayed functional clustering on the ~10 μm scale and this clustering was more pronounced in the somatic place field versus outside. These results implicate increases in total excitatory (glutamate) input and super-linear dendritic summation in CA1 place field firing, indicating that post-synaptic strength is not the sole determinant of field location, as is currently thought. Further, since they largely inherit their fields from upstream synaptic partners with similar fields, many CA1 place cells appear to be part of multi-brain-region cell assemblies forming representations of specific locations.

4.3 Results

4.3.1 Method for optical recording of excitatory input to CA1 neuron dendrites during spatial behaviors

To optically record excitatory synaptic input to CA1 neuron dendrites, we sparsely labeled the CA1 pyramidal neuron population in adult mice with SF-iGluSnFR.A184S (iGluSnFR)(Marvin, Scholl et al. 2018)—a membrane targeted genetically encoded glutamate sensor that reports increases in extracellular glutamate concentration through increasing fluorescence, in a manner independent of post-synaptic strength(Soares, Lee et al. 2017). To determine the sensitivity of iGluSnFR, we used whole cell recording and glutamate uncaging in slice (hippocampal slices, adult mice). We characterized spontaneous mini-EPSPs representing single vesicle release events(Enoki, Hu et al. 2009, Weber, Andrasfalvy et al. 2016) with whole-cell recordings (mean±SEM: half width 13.44±0.49 ms, 4.36±0.09 ms 10-90% rise time, 0.53 ± 0.017 mV amplitude; 299 events in 5 cells from 4 mice; Figure 4.1a-c) and then found that uncaging with 25-29 mW generated evoked-EPSPs of the same amplitude and duration as the single vesicle release mini-EPSPs (Figure 4.1d). Using 2P microscopy, we found that the amplitude of the iGluSnFR fluorescence transients ($\Delta F/F$) in the 1 μm dendritic region adjacent to the uncaging site increased monotonically with increasing uncaging power (29 spine uncaging sites, 14 branches, 3 mice; Figure 4.1e-g) and, importantly, 96% of the 25-29 mW stimulations (mimicking single vesicle release(Soares, Trotter et al. 2019)) resulted in significant iGluSnFR transients with mean peak amplitudes, durations and integrals of 0.56+-0.18 (SD) $\Delta F/F$, 0.23+-0.059 (SD) seconds, and 0.058+-0.003 (SD) $\Delta F/F$*sec*μm, respectively (Figure 4.1h-j). By contrast, the detection sensitivity under the same conditions using a GECI (GCaMP6s,f)(Chen, Wardill et al. 2013) was far less (Figure 4.2), likely due to Mg^{2+} block of NMDA receptors.

Therefore, iGluSnFR ΔF/F averaged over 1 μm regions of CA1 pyramidal neuron dendrites provides a measure of excitatory input with single vesicle detection sensitivity.

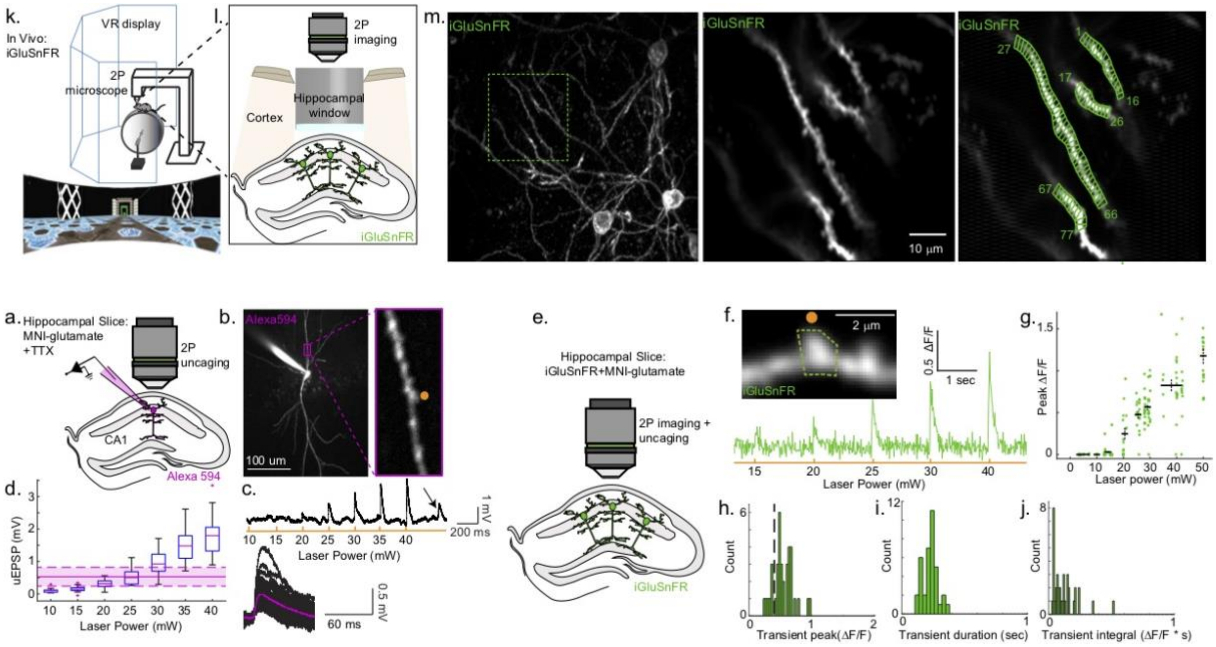

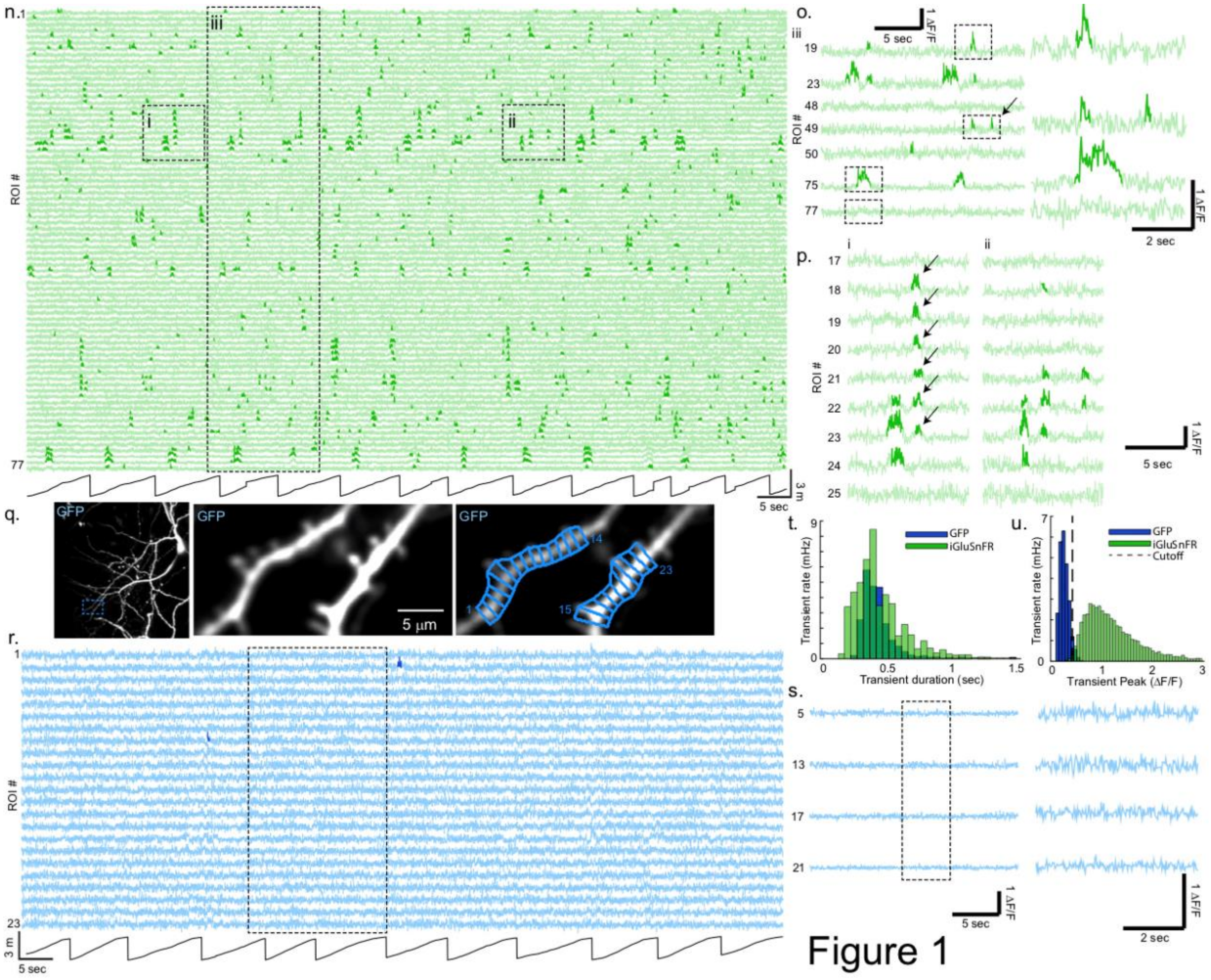

xiii Figure 4.1: Optical recording of excitatory input to CA1 neuron dendrites during spatial behaviors.

a. Schematic depicting slice intracellular current clamp recording and 2P glutamate uncaging experiments. Glutamate was uncaged at dendrites of CA1 neurons filled with Alexa-594 in bath solution containing MNI-glutamate and TTX.

b. Left, Example neuron filled with Alexa-594; right, dendritic uncaging site marked with orange dot.

c. Top, example membrane potential trace of uncaging evoked EPSPs (uEPSPs) driven using different laser powers from example shown in **b**. Spontaneous EPSP (arrow) in presence of TTX represents a single vesicle release event (miniature EPSP). Bottom, all miniature EPSPs from all recordings (black) and the average of all miniature EPSPs (purple).

d. Plot of mean peak membrane potential amplitude of uEPSPs vs. uncaging power from all recordings (16 uncaging sites, 11 branches, 6 slices, n = 4 mice). Mean miniature EPSP peak amplitude (solid purple line) and SD (shaded region out to dashed lines) from **c** shown directly overlapping uEPSPs from 25-29mW stimulations.

e. Schematic depicting slice experiments with 2P iGluSnFR imaging combined with 2P glutamate uncaging. Glutamate was uncaged at dendrites of CA1 pyramidal neurons expressing iGluSnFR in a sparsely labeled CA1 population.

f. Top, Example dendritic segment from neuron expressing iGluSnFR; dendritic uncaging site marked with orange dot and 1-µm length ROI outlined in green. Bottom, example ΔF/F vs time trace during uncaging with different laser powers from the example ROI and uncaging site shown at top.

g. Plot of peak of iGluSnFR fluorescence transients (in 1 µm ROIs) vs. uncaging power from all recordings (29 uncaging sites, 14 branches, 5 slices, n = 3 mice)—green = individual transients, black = mean ± SE.

h-j. Histograms of peaks (**h**), durations (**i**) and integrals (**j**) of all iGluSnFR fluorescence transients (in 1 µm ROIs) generated using 25-29mW uncaging power (mimicking single vesicle release). Amplitude cutoff threshold for significant iGluSnFR transients determined *in vivo* during behavior shown by dashed line.

k. Schematic of behavioral apparatus (top) and example of the virtual linear track (bottom). **l.** Schematic of hippocampal imaging window used to image CA1 pyramidal neurons expressing iGluSnFR with 2P microscopy during spatial behaviors in VR.

m. Left, example z-projection image of CA1 pyramidal neurons expressing iGluSnFR and imaged during behavior. Middle, mean image from time-series acquired at a single imaging plane (from region shown at left). Right, same as middle, but 77 1 µm ROIs shown in green.

n. iGluSnFR ΔF/F vs time traces for each ROI shown in **m** (right) acquired during linear track navigation (track position at bottom). Significant transients highlighted in bold.

o. Left, expanded scale of a subset of traces shown in region iii from **n**; arrow, example transients restricted to 1 ROI. Right, expanded scale of traces shown dashed at left.

p. Left, expanded scale of traces shown in region i from **n** showing synchronous transients occurring over adjacent ROIs 18-23, marked with arrows. Right, expanded scale of traces shown in region ii from **n** showing transients in only some of the ROIs that were synchronously active in region i.

q. same as **m**, but neurons expressing GFP.

r. same as **n**, but from ROIs shown in **q** (right).

s. Left, expanded scale of traces shown in dashed region in **r**. Right, expanded scale of traces shown dashed at left.

t-u. Histograms of durations (**t**) and peaks (**u**) of all significant iGluSnFR or GFP fluorescence transients from all 1 µm ROIs from all CA1 dendritic imaging sessions during behavior. Significant iGluSnFR transient amplitude cutoff threshold shown by dashed line.

To optically record excitatory input to CA1 neuron dendrites during spatial behaviors, we sparsely labeled CA1 pyramidal neurons with SF-iGluSnFR.A184S, installed a chronic hippocampal window, and used 2P microscopy to image the labeled neuron dendrites as mice performed spatial behaviors in virtual reality (VR). We recorded time-series movies from 109 basal and proximal oblique dendritic segments (mean±SD: 126±46 microns from soma, 2.2±0.8 branch points from soma), from 47 fields of view ([40-72 µm]x[25-71 µm], 30-60 Hz frame rate) from 11 mice navigating in a familiar linear track for water rewards (Figure 4.1k,l). Recordings from these dendrites are highly relevant for understanding the synaptic basis of CA1 place field firing since acute silencing of the presynaptic regions providing their inputs results in cessation of CA1 place firing(Davoudi and Foster 2019). We selected 1-micron length regions of interest (ROIs) tiling the length of each dendritic segment and generated a ΔF/F vs time trace for each ROI (Figure 4.1m,n). These traces consisted of numerous, statistically significant, positive-going iGluSnFR transients (<0.01 false positive rate, see Methods; bold in Figure 4.1n), typically appearing as a sharp rise, followed by a slower decay to baseline, and with a range of amplitudes and durations (Figure 4.1o,t,u; mean peak amplitude: 1.11+-0.65 (SD) ΔF/F; mean duration: 0.35+-0.21 (SD) seconds). iGluSnFR transients were typically restricted to 1 or 2 ROIs (76% restricted to 1 ROI, 15% restricted to 2; Figure 1n, o, arrow; Extended Data Figure 2a), though synchronous transients occurring over larger numbers of adjacent ROIs were also observed (9% ≥3 ROIs; Figure 4.1p arrows, Figure 4.3c).

As a control, we repeated the above experiments and analyses, but expressed the non-functional indicator GFP (19 basal and proximal oblique dendritic segments, n=4 mice) instead of iGluSnFR. The GFP traces consisted of noise, with only occasional false positive transients occurring at the expected statistical false positive rate (Figure 4.1q-s). The distribution of GFP noise transient amplitudes were smaller (Figure 4.1u) and almost completely non-overlapped with the iGluSnFR transient amplitudes. Applying a minimum amplitude threshold of 0.40 ΔF/F left only 5% of GFP transients, but 98% of iGluSnFR transients; these remaining significant iGluSnFR transients were used for all subsequent analysis. Importantly, applying this minimum 0.40 ΔF/F threshold to the slice iGluSnFR transients generated using 25-29mW stimulations (mimicking single vesicle release) left 81% of the slice transients (Figure 4.1h). Therefore, our methods allow for measurements of transient excitatory synaptic input to CA1 pyramidal neuron dendrites, with single vesicle sensitivity at the 1 µm spatial scale in behaving mice, consistent with previous reports *in vitro*(Jensen, Zheng et al. 2019, Soares, Trotter et al. 2019), but now extending the methods to *in vivo* investigations.

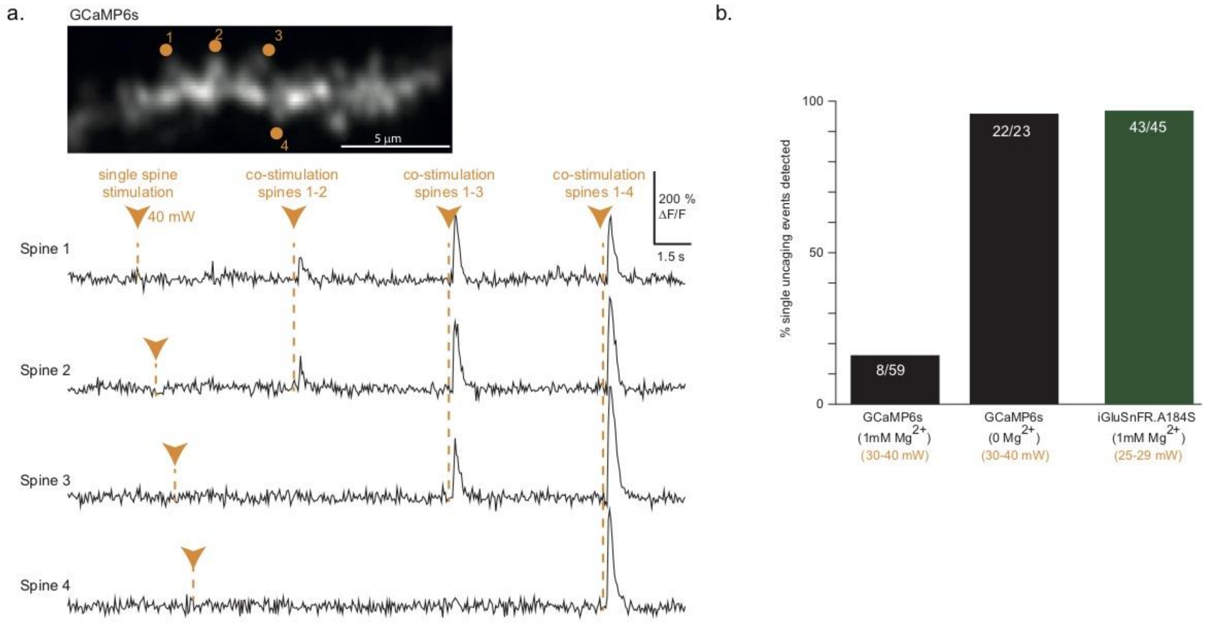

xiv Figure 4.2: Sensitivity of GCaMP6s for detecting single vesicle release.

a. Top, Example dendritic segment from CA1 pyramidal neuron expressing GCaMP6s in hippocampal slice; dendritic uncaging sites marked with orange dots. Bottom, example ΔF/F vs time traces during uncaging using 40mW uncaging power (even larger than the 25-29 mW uncaging power mimicking single vesicle release) from the example spines and uncaging sites shown at top (with 1mM Mg^{2+} in bath). No fluorescence transients were detectable when spines were individually stimulated (first stimulations, 300 ms inter-stimulus interval), but co-stimulation of 2 or more spines (120 µs inter-stimulus interval) led to detectable fluorescence transients—demonstrating that spines were responsive, and cooperativity was required in most cases to detect synaptic glutamate arrival with GCaMP6s.

b. Percent of single uncaging events (uncaging power >= single vesicle release power) detected using GCaMP6s (with 1mM Mg^{2+} in bath; 14 branches, n = 4 mice), GCaMP6s (with 0mM Mg^{2+} in bath; 5 branches, n = 2 mice), or iGluSnFR (with 1mM Mg^{2+} in bath; 29 spines, 14 branches, n = 3 mice). While most events were not detected with GCaMP6s with Mg^{2+} in the bath, nearly all events were detected when Mg^{2+} was removed from the bath, suggesting that Mg^{2+} block of NMDA receptors prevents sufficient calcium influx to occur during single vesicle release to be detected by GCaMP6s.

4.3.2 Characterization of Glutamate Transmission In Vivo

Glutamate spillover beyond the synaptic cleft could activate NMDA receptors in nearby synapses and enhance synaptic cooperativity(Asztely, Erdemli et al. 1997). Since SF-iGluSnFR.A184S and NMDA receptors have a similar glutamate binding affinity (SF-iGluSnFR.A184S: 0.6 µM; High-affinity NMDA receptors: 1 µM)(Clements 1996, Marvin, Scholl et al. 2018), the spatiotemporal profile of the iGluSnFR transients provides an estimate of this spillover and has important implications for interpreting the amount and source of glutamate input to CA1 dendrites. Small amplitude (smallest 20%; ~<0.75 ΔF/F) and short duration (shortest 35%; ~<0.3sec) *in vivo* iGluSnFR transients were highly similar to the slice iGluSnFR transients evoked from single vesicle mimicking uncaging events (Figure 4.1f-j,o,t,u and Figure 4.3e-f), suggesting that many of the *in vivo* transients were generated from single vesicles released at single synapses. Most (76%) *in vivo* iGluSnFR transients were contained within a single 1-micron ROI (see Figure 4.3d for average profile image), and an additional 15% were contained within 2 adjacent 1-micron ROIs (Figure 4.1n, o, arrow; Figure 4.3a), likely representing single synapses bisected by the ROIs. Given this small scale of spillover (similar to previous *in vitro* reports using iGluSnFR(Jensen, Zheng et al. 2019)), it is unlikely that much glutamate spilled from synapses onto adjacent unlabeled dendrites of other neurons was detected in our labeled dendrites (See Methods for further discussion). Higher amplitude and longer duration transients presumably represent the release of multiple presynaptic vesicles. Our observations thus suggest that most spillover detected by iGluSnFR is highly localized (~1 µm) on CA1 dendrites during behavior.

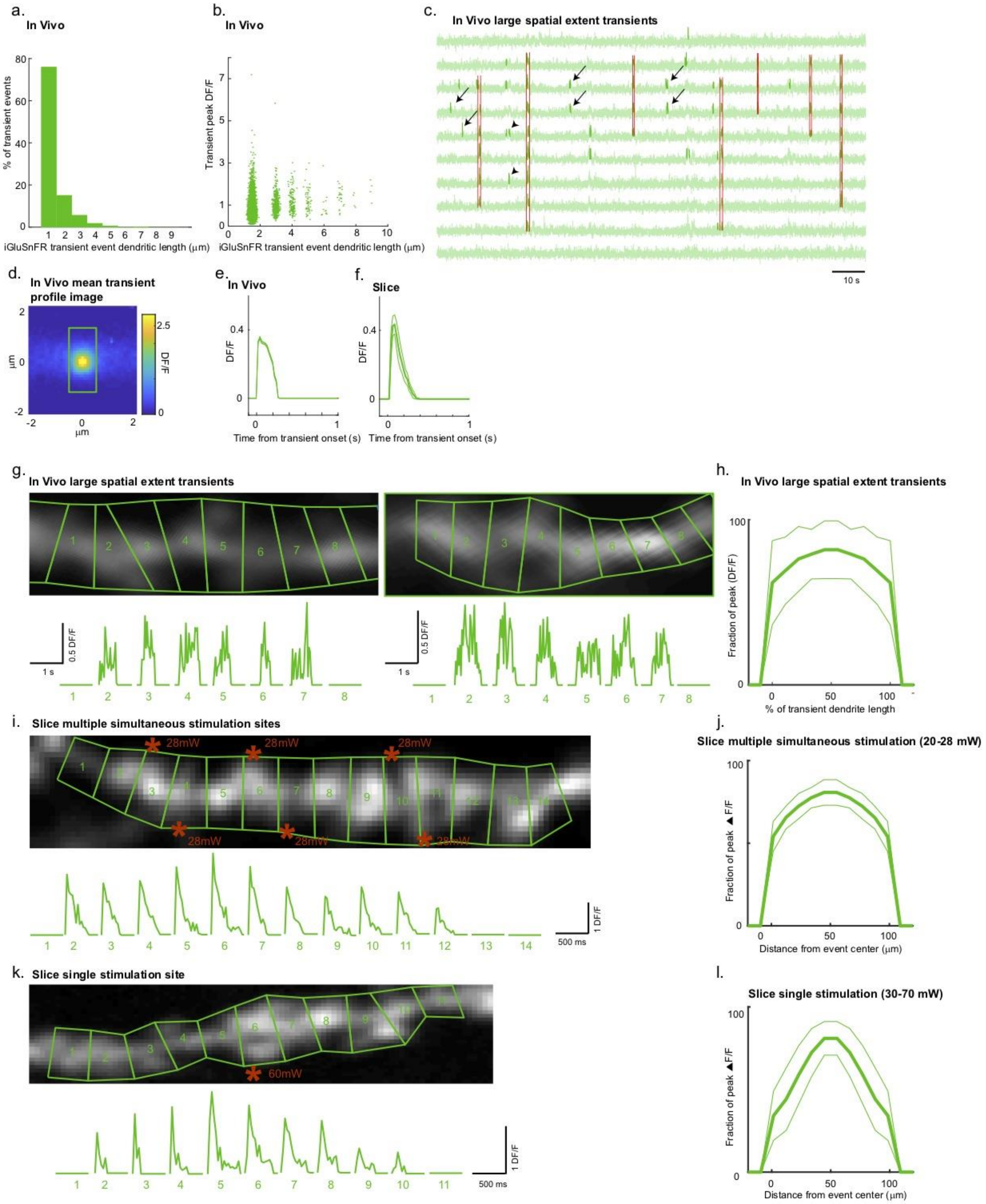

xv Figure 4.3: Characterization Characterization of spatiotemporal properties of single ROI and large spatial extent iGluSnFR transients.

a. Histogram of iGluSnFR transient event dendritic length measured in number of 1µm ROIs. Transients are from all iGluSnFR *in vivo* dendrite recordings, including place cells, nonplace cells, and dendrites that could not be traced to recorded somas.

b. Plot of peak ΔF/F amplitude versus iGluSnFR transient event dendritic length for all transients shown in **a**. Note that little or no correlation exists between the amplitude and spatial extent of the *in vivo* transients.

c. iGluSnFR ΔF/F vs time traces from ROIs on a single branch acquired during linear track navigation. Significant transients highlighted in bold green, and large spatial extent transients outlined in red. Note that the co-active adjacent ROIs recruited during the large spatial extent transients (red) could be recruited with fewer (arrows) and/or non-adjacent ROIs at other times (arrowheads).

d. Mean image of iGluSnFR transients restricted to 1 µm ROIs. The full width at half maximum of 0.8 µm (Gaussian fit) suggests that most glutamate spillover beyond a synapse that is detected by iGluSnFR is highly localized (~1 µm) on CA1 dendrites during behavior. Size of 1 µm ROI (along length of dendrite) shown for reference in green.

e. Triggered average of smallest 20% ΔF/F and shortest 35% duration *in vivo* iGluSnFR transients restricted to 1 µm ROIs (214 transients). Average triggered on transient onset.

f. Triggered average of all slice iGluSnFR transients generated by 25-29 mW stimulations (mimicking single vesicle release), same transients as shown in **Figure 4.1h,i**. Average triggered on transient onset. Note the similarity between the average of the smallest and shortest *in vivo* transients and the transients from single vesicle stimulations in slice, suggesting that many of the *in vivo* transients were generated from single vesicles released at single synapses. Also note that the range of uncaging powers used here to mimic single vesicle release (25-29mW) has previously been shown in CA1 dendrites in slice to generate iGluSnFR transients highly similar to transients generated from pre-synaptic release(Soares, Trotter et al. 2019).

g. Two examples of large spatial extent iGluSnFR transients extending over 6 adjacent ROIs observed during spatial navigation. ROIs drawn in green on iGluSnFR labeled dendrite at top, and significant iGluSnFR transients from each ROI shown at bottom. Note the relatively flat (plateau like) profile of the peak ΔF/F across the different ROIs containing the transients.

h. Mean profile of the peak ΔF/F across the different ROIs containing large spatial extent iGluSnFR transients, averaged over all large spatial extent transients >=5 ROIs in length observed *in vivo* during spatial navigation (99 transients, 11 mice). Note the relatively flat (plateau like) profile, similar to the individual examples in **g**.

i. Example of large spatial extent iGluSnFR transient extending over 11 adjacent ROIs generated in slice using multi-site simultaneous glutamate uncaging. Uncaging sites (28 mW, 500 µs per site, 120 µs interstimulus site interval) marked with red asterisks at top, and significant iGluSnFR transients from each ROI shown at bottom. Note the relatively flat (plateau like) profile of the peak ΔF/F across the different ROIs containing the transients.

j. Mean profile of the peak ΔF/F across the different ROIs containing large spatial extent iGluSnFR transients, averaged over all large spatial extent transients >=5 ROIs in length generated in slice using stimulation parameters detailed in **i** (23 transients, 2 mice, 25-29 mW). Note the relatively flat (plateau like) profile, similar to the individual example in **i**, and importantly, similar to the mean *in vivo* profile shown in **h**.

k. Example of large spatial extent iGluSnFR transient extending over 9 adjacent ROIs generated in slice using a single large amplitude glutamate uncaging pulse. Uncaging site (60 mW, 500 µs) marked with red asterisk at top, and significant iGluSnFR transients from each ROI shown at bottom. Note the peaked (mountain-like) profile of the peak ΔF/F across the different ROIs containing the transients.

l. Mean profile of the peak ΔF/F across the different ROIs containing large spatial extent iGluSnFR transients, averaged over all large spatial extent transients >=6 ROIs in length generated in slice using stimulation parameters detailed in **k** (9 transients, 2 mice, >30 mW). Note the peaked (mountain-like) profile similar to the individual example in **k**, and importantly, dissimilar to the mean *in vivo* profile shown in **h**. The profile shapes shown in **h, j, l** support the interpretation that the large spatial extent iGluSnFR transients observed *in vivo* are likely caused by synchronized-release of glutamate vesicles from different presynaptic terminals onto multiple adjacent dendritic ROIs, rather than synchronized-release of many presynaptic vesicles onto a single ROI with glutamate spillover detected over adjacent ROIs.

Different mechanisms could lead to the observed larger spatial extent iGluSnFR transients (>3 adjacent ROIs; Figure 4.1p arrows, Figure 4.3c): 1. Synchronized-release of vesicles from different presynaptic terminals onto multiple adjacent ROIs, or 2. Synchronized - release of many presynaptic vesicles (from one or more terminals) onto a single ROI with glutamate spillover detected over adjacent ROIs. To distinguish between these possibilities, we first examined the spatial ΔF/F amplitude profile of individual *in vivo* large spatial extent transients and found a plateau-like profile (Figure 4.3g,h). Second, we found that the peak amplitude of iGluSnFR transients was only weakly related to their spatial extent (Figure 4.3b), and third that the co-active adjacent ROIs recruited during large spatial extent transients could be recruited with fewer and/or non-adjacent ROIs at other times (Figure 4.1p, Figure 4.3c). These findings are far more consistent with mechanism 1 than 2. Further, we mimicked these mechanisms in slice. Uncaging at multiple sites along a dendrite (mechanism 1) resembled our *in vivo* observations, unlike strong uncaging at a single site (mechanism 2) (Figure 4.3i-l). Thus, the large spatial extent iGluSnFR transients observed *in vivo* are likely caused by synchronized-release of glutamate vesicles from different presynaptic terminals onto multiple adjacent dendritic ROIs.

Since most (~80%, Figure 4.1h,u) single vesicle release events are likely detected *in vivo*, we reasoned that we could use the integral of the iGluSnFR transients generated in slice from the single vesicle release mimicking stimulations to estimate the rate of excitatory vesicles received by CA1 pyramidal neurons during spatial behaviors. We calculated the integral of all significant transients *in vivo* per second per 1-µm ROI (0.0056+-1.6e-4 ΔF/F, mean±SE) and divided by the slice single vesicle integral (0.058+-0.003 ΔF/F*sec*µm/vesicle) to arrive at 0.10 [95% confidence: 0.08-0.11] vesicles/(sec*µm). Importantly, this rate falls within the range of rates that can be estimated using CA3 firing rates during navigation (0.5±0.78 spikes/second)(Mizuseki, Royer et al. 2012), the estimated fraction of active CA3 neurons (0.3±0.2)(Thompson and Best 1989, Shoham, O'Connor et al. 2006, Hainmueller and Bartos 2018), the number of CA3 excitatory synapses per micron of CA1 dendrite (3.25±0.25 spines/µm)(Megias, Emri et al. 2001, Routh, Johnston et al. 2009), and the vesicle release probability at these synapses (0.35±0.15 vesicles/spike)(Bolshakov and Siegelbaum 1995, Holderith, Lorincz et al. 2012), which provides an estimate of 0.17±0.30 vesicles/(sec*µm).

4.3.3 Characterizing Tuning of Inputs to Place Cells and Non-Place Cells

Many CA1 place cell models assume spatially tuned, Gaussian shaped excitatory inputs(Burgess and O'Keefe 1996, Bittner, Grienberger et al. 2015, Weber and Sprekeler 2018), however recordings from the presynaptic CA2/3 populations have found neurons with a wide range of activity and spatial selectivity(Mizuseki, Royer et al. 2012, Mankin, Diehl et al. 2015). It is currently unknown which combination of these neurons provide excitation to CA1 place cells. To address this question, we sparsely labeled CA1 such that single pyramidal neurons co-expressed jRGECO1a (a red calcium indicator)(Dana, Mohar et al. 2016) and iGluSnFR. During track traversals, we first recorded somatic time-series movies (red channel; from 33 fields of view in 11 mice; 22.5 ± 1.5 (SE) traversals /somatic recording) as a measure of action potential firing and then adjusted the focal plane to record the excitatory input to the dendrites with iGluSnFR (green channel). Z-series morphology was used to trace dendrites back to the parent cell body. We identified 23 place cells (with 26 place fields) and 23 non-place cells (including 16 active non-place cells and 7 silent cells; Figure 4.4a-d) and recorded from their basal and proximal oblique dendritic segments (Place cell dendrites: 62 branches, 1192 microns of total length, 128+-44µm (SD) from soma, 2.4±0.9 (SD) branch depth from soma, 17.6 ± 1.5 traversals /dendritic recording; Non-place cell dendrites: 41 branches, 749 microns of total length, 124±49µm from soma, 2.0±0.6 branch depth from soma, 21.6 ± 1.8 traversals /dendritic recording; mean±SE), (Figure 4.4e). For each 1-µm dendritic ROI, we plotted mean significant iGluSnFR transients (ΔF/F) versus track position over all traversals (mean ROI map) and found many ROIs with place fields (place-ROIs), without clearly defined fields (active-non-place ROIs) or without significant activity (silent-ROIs) (Figure 4.4f). Individual place cells typically contained all three general types of ROIs, which covered the track with excitatory input (Figure 4.4g).

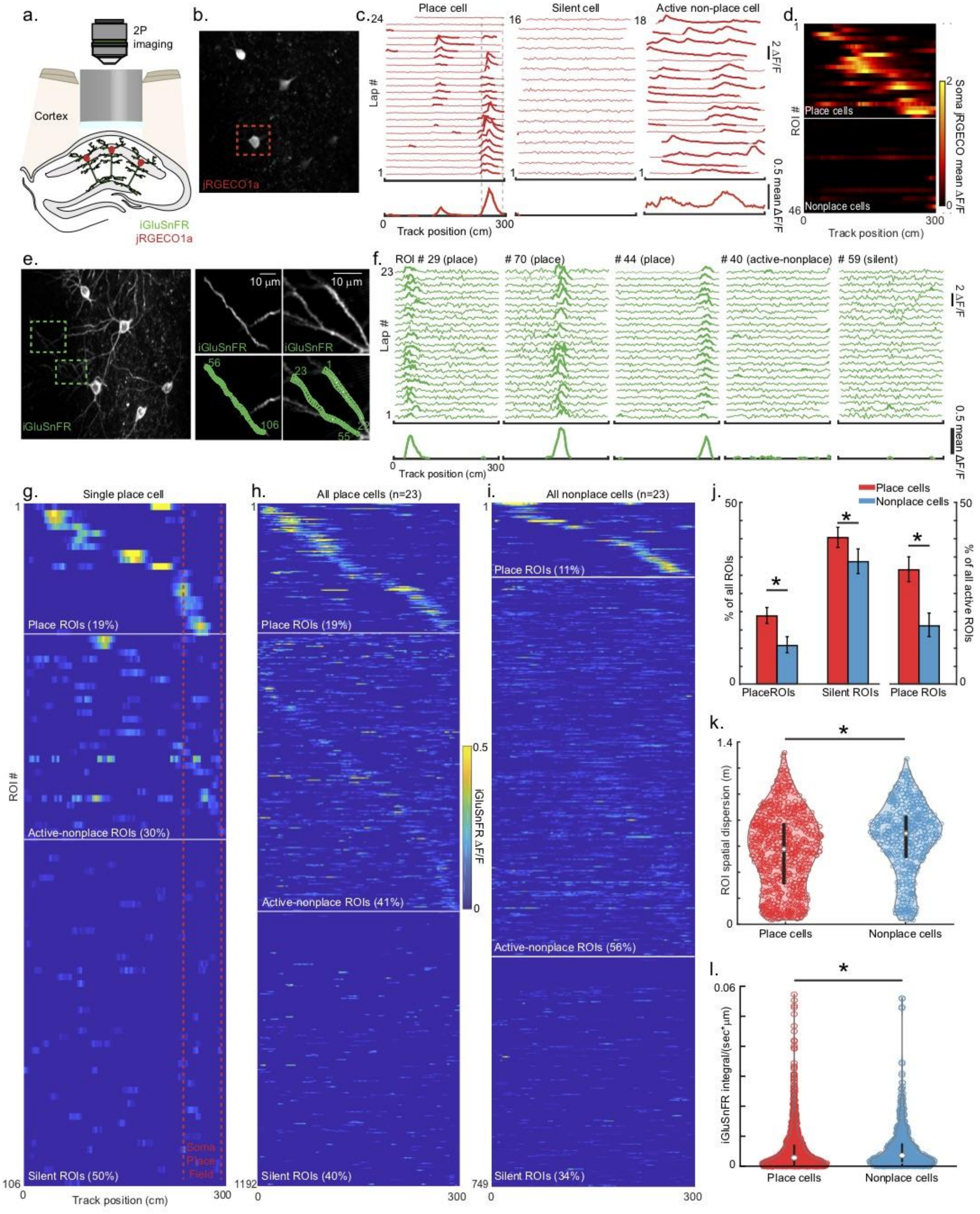

xvi Figure 4.4: Spatial tuning of excitatory synaptic inputs to place and nonplace cells.

a. Schematic of experiments using 2P microscopy to image CA1 pyramidal neuron somatic firing patterns with jRGECO1a (red) and excitatory synaptic inputs to dendrites with iGluSnFR (green) during spatial behaviors in VR.

b. Example image of jRGECO1a fluorescence from labeled CA1 pyramidal neurons imaged during behavior.

c. Somatic jRGECO1a ΔF/F versus track position for each traversal of a single session (top) and mean ΔF/F versus position across all traversals (bottom) for 3 different neurons from different mice. Place cell at left (cell highlighted in **b**) with place field track location between dashed lines, silent cell at middle, active-nonplace cell at right. Significant transients highlighted in bold.

d. Mean somatic jRGECO1a ΔF/F versus track position across all traversals of a single session for all recorded neurons (each row represents single neuron mean ΔF/F).

e. Left, example z-projection image of iGluSnFR fluorescence from labeled CA1 pyramidal neurons imaged during behavior (same neurons and field of view as shown in **b**). Right, top, mean images from time-series acquired at 2 different single imaging planes (from regions shown at left). Right, bottom, same as top, but 106 1-µm ROIs shown in green.

f. iGluSnFR ΔF/F vs track position for each traversal of a single session (top) and mean ΔF/F versus position across all traversals (mean ROI map, bottom) for five example ROIs shown in **e** (right); from place cell shown in **b,c**. Significant transients highlighted in bold. Place ROIs: 29,44, 70; Silent ROI: 59, Active-nonplace ROI: 40.

g. Mean iGluSnFR ΔF/F versus track position across all traversals of a single session (mean ROI map) for all ROIs (each row represents a single ROI mean ΔF/F) shown in **e** (right); from place cell shown in **b,c**. Somatic place field track location between dashed lines. Percentage of ROIs in each ROI category also shown. Plotted via cross-validation within each ROI category.

h-i. Same as g, but for all ROIs from all 62 branches of all 23 place cells (**h**) or all 41 branches of all 23 nonplace cells (**i**).

j. Percentage of ROIs in each ROI category for place vs nonplace cells. Mean ± bci across dendritic branches. (*p<3.2e-3, likelihood ratio test).

k. Spatial dispersion of iGluSnFR transients in each ROI for all ROIs in place cells vs. nonplace cells (*p=1.24e-4, likelihood ratio test).

l. Mean amount of excitatory input per ROI per second (integral of all significant iGluSnFR transients in each ROI divided by recording time) for all ROIs in place cells vs. nonplace cells (*p=9.1e-4, Rank-sum test, place<nonplace).

We then pooled the mean ROI maps across all place cells (Figure 4.4h, plotted and sorted via cross-validation, see Methods) and separately from all non-place cells (Figure 4.4i) to examine the relative fraction of each ROI type in each cell type. We found that place cell dendrites contain 19±2% (95% binomial confidence interval, bci) place ROIs, 41±3% (95% bci) active-non-place ROIs, and 40±3% (95% bci) silent-ROIs, while non-place cell dendrites contain 11±2% (95% bci) place ROIs, 56±4% (95% bci) active-non-place ROIs, and 34±3% (95% bci) silent-ROIs. Place cells contained a significantly larger percentage of place and silent ROIs (χ_{12}=24.13, p=8.9e-7 and χ_{12}= 8.67, p=3.2e-3, respectively, Likelihood ratio test; Figure 4.4j), and a smaller percentage of active-non-place ROIs (χ_{12}=40.4, p=2.1e-10 Figure 4.4j), compared to non-place cells. Interestingly, the pooled mean ROI maps (Figures 4.4h,i) revealed that the non-place ROIs in place cells were more spatially selective than the non-place ROIs of non-place cells (see faint sequence in the non-place ROIs of place cells, not apparent in non-place cells). Further, the track spatial dispersion of iGluSnFR transients in each ROI was significantly smaller on average in place cells versus non-place cells (0.55±0.011m (SE) vs 0.65+-0.012m (SE), respectively, p=1.24e-4, Rank-sum test; Figure 4.4k; see Methods). Thus, place cells receive a combination of place, active-non-place, and silent excitatory inputs that cover all track locations, and these inputs are more spatially selective in place versus non-place cells.

To estimate the mean amount of excitatory input received by each cell type, we calculated the integral of all significant iGluSnFR transients per ROI per second and found that place cells receive 0.0054+-2.1e-4 ΔF/F (or 0.09 [95% confidence: 0.08-0.11] vesicles/(sec*µm) using the slice calibration above), which was similar but less (p=9.1e-4, Rank-sum test) than the 0.0058+-2.5e-4 ΔF/F (or 0.10 [95% confidence: 0.08-0.12] vesicles/(sec*µm)) received by non-place cells (Figure 2l). Therefore, on average, place cells receive slightly less excitatory input compared to non-place cells.

4.3.4 Relationship between Spatial Tuning of Inputs and Somatic Spatial Tuning

Thus far we have established that place cells receive a similar amount of mean excitatory input compared to non-place cells, the excitation covers all track locations in both cell types, and excitatory inputs are more spatially selective in place versus non-place cells. However, none of these findings explain the spatially selective firing of place cells. The following four (non-exclusive) hypotheses have previously been considered. First, post-synaptic plasticity mechanisms could potentiate the specific excitatory inputs that are preferentially active in-field(Bittner, Grienberger et al. 2015, Bittner, Milstein et al. 2017, Sheffield, Adoff et al. 2017, Sheffield and Dombeck 2019, Zhao, Wang et al. 2019). Second, in-field disinhibition could allow for uniform excitation to drive track location specific firing (Ego-Stengel and Wilson 2007, Wilent and Nitz 2007, Ahmed and Mehta 2009). Third, total excitatory (glutamate) input could be greater in-field versus out-of-field(Enoki, Hu et al. 2009, Deguchi, Donato et al. 2011, Hill and Zito 2013, Dragoi and Tonegawa 2014, Berns, DeNardo et al. 2018). Fourth, in-field active excitatory inputs might be more temporally co-active and anatomically clustered in the arbor versus out-of-field inputs, making them more effective at driving firing through super-linear dendritic amplification(Golding, Staff et al. 2002, Ariav, Polsky et al. 2003, Gasparini, Migliore et al. 2004, Losonczy and Magee 2006, Schmidt-Hieber, Toleikyte et al. 2017). Since our iGluSnFR measurements report total excitatory input, and are insensitive to post-synaptic strength(Soares, Lee et al. 2017) and inhibitory input, we could address the third and fourth hypotheses, but not the first and second.

To test whether the total excitatory input was greater in-field versus out-of-field (hypothesis 3), we plotted the mean ROI map for each ROI from each place cell in units of somatic place field width and then pooled the maps together by centering each at the track location of the somatic place field peak (Figure 4.5a). By averaging over all active ROIs, we generated a plot of mean total excitatory input as a function of distance from the center of the mean somatic place field (Figure 4.5b). This revealed that excitatory input was broadly increased around the somatic place field, with a shape and width reminiscent of the hill of depolarization observed from intracellular recordings(Harvey, Collman et al. 2009). In-field total excitation was significantly greater than out-of-field (in-field: 0.023+-0.002 (SE) ΔF/F, out of field: 0.017+-0.001 (SE) ΔF/F, p=3.05e-10, Rank-sum test). Interestingly, when we averaged over place and non-place ROIs separately (Figure 4.5b), we found that nearly all the in-field increase in excitatory input originated from the place ROIs (place ROIs in-field: 0.042+-0.004 (SE) ΔF/F, place ROIs out of field: 0.029+-0.003 (SE) ΔF/F, p=4e-6, Rank-sum test; nonplace ROIs in-field: 0.014+-0.001 (SE) ΔF/F, nonplace ROIs out of field: 0.012+-0.001 (SE) ΔF/F, p=0.72, Rank-sum test). Thus, place cells receive greater total excitatory input inside versus outside of the somatic place field (supporting the third hypothesis above), and this increase originates mainly from the most spatially selective inputs.

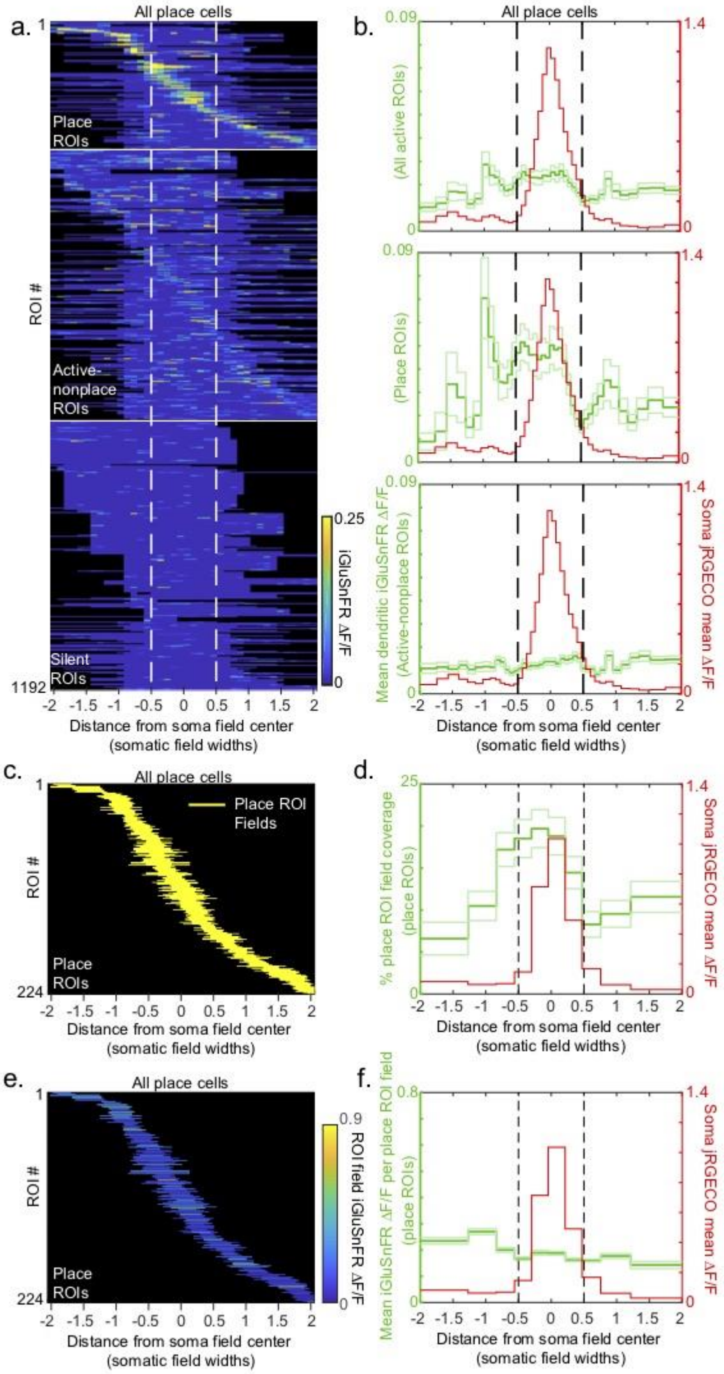

xvii Figure 4.5: Total excitatory input is greater in the somatic place field versus out.

a. Mean iGluSnFR ΔF/F versus position from somatic place field center (in units of somatic place field width) across all traversals of a single session for all ROIs (each row represents single ROI mean ΔF/F) from all 62 branches of all 23 place cells (same ROIs as shown in **Figure 4.4h**).

Mean somatic place field between dashed lines. Plotted via cross-validation within each ROI category.

b. Mean total excitatory input (green) as a function of distance from the center of the mean somatic place field (red) for all active ROIs (top), all place ROIs (middle) and all active-nonplace ROIs (bottom). Mean (dark green) ± SE (light green).

c,d. All place ROI fields (yellow) versus position from somatic place field center (**c**) and percentage of place ROIs with place ROI field coverage (green) of binned positions from center of mean somatic place field (red; **d**, bin size different than in **b**).

e,f. All place ROI fields colored by their (mean) ROI field ΔF/F versus position from somatic place field center (**e**), and mean ΔF/F per place ROI field (green) versus position from center of mean somatic place field (red; **f**, bin size different than in **b**).

We then tested whether this in-field total excitatory input increase was due to a greater percentage of ROIs active in-field or to increased excitatory input to in-field active ROIs. Since the in-field increase was mostly due to place ROIs, we focused our analysis on the place ROI fields (Figure 4.5c-e). We plotted the percentage of place ROI fields covering binned positions from the center of the mean somatic place field and found the percentage was broadly increased around the somatic field (Figure 4.5c,d; in-field 17.8+-1.4% (SE), significantly larger than out-of-field, 11.3+-0.9% (SE), p=1.15e-05, rank-sum test), with an ~1.6x in-field to out-of-field percentage increase, similar to the total excitatory increase described above (Figure 4.5b). Next, we plotted the mean ΔF/F per place ROI field versus position from the center of the mean somatic place field, and found that the mean in-field ΔF/F was not significantly different than out-of-field (Figure 4.5e,f, in-field, 0.17+-0.01 (SE) ΔF/F, not significantly different than out of field, 0.172+-0.01(SE) ΔF/F, p=0.416, Rank-sum test). Therefore, the in-field total excitatory input increase is largely due to an increased percentage (increased number) of place-ROIs with spatial tuning overlapping the somatic field versus outside of the field.

4.3.5 Relationship between the functional and anatomical organization of inputs onto the dendrite and the spatial location of the somatic place field

To test whether excitatory input inside versus outside of the place field was more temporally co-active and anatomically clustered in the arbor (hypothesis 4), we examined the functional dendritic organization of the ROIs in terms of both their spatial track selectivity and temporal activation patterns (Figures 4.6 and Figure 4.7). When we colored ROIs according to their spatial selectivity, we often observed groups of adjacent ROIs (<~10) with similar track selectivity (Figure 4.6a, arrows), a pattern that appeared more often in place versus non-place cells. Spatial correlation versus intra-dendrite ROI distance analysis also revealed elevated correlations on the ~10 µm scale in place cells, larger correlations than in non-place cells or inter-dendrite correlations (Figure 4.6b, see also Figure 4.5a-c; exponential fits, χ_{12}=86.6, p~0). Further, as expected from our observation of large spatial extent transients (Figure 4.1p, Figure 4.3c), temporal correlation versus intra-dendrite ROI distance analysis revealed greater correlations over <~10 µm in place versus non-place cells or inter-dendrite correlations (exponential fits, χ_{12} =60.3, p~8.3e-15; Figure 4.6c), and further, a greater percentage of intra-dendrite ROIs within 10 µm of each other were likely to be co-active in place vs non-place cells (Figure 4.7d). The flat inter-dendrite correlations versus ROI distance relationships (Figure 4.6b,c) further indicates that it is unlikely that much glutamate spilled from synapses onto adjacent unlabeled dendrites of other neurons was detected in our labeled dendrites (See

Methods for further discussion; Figure 4.3). Thus, excitatory input to place cell dendrites was functionally organized such that, on average, ROIs <~10 µm apart encoded more similar track locations and were more likely to be co-active compared to greater dendritic distances.

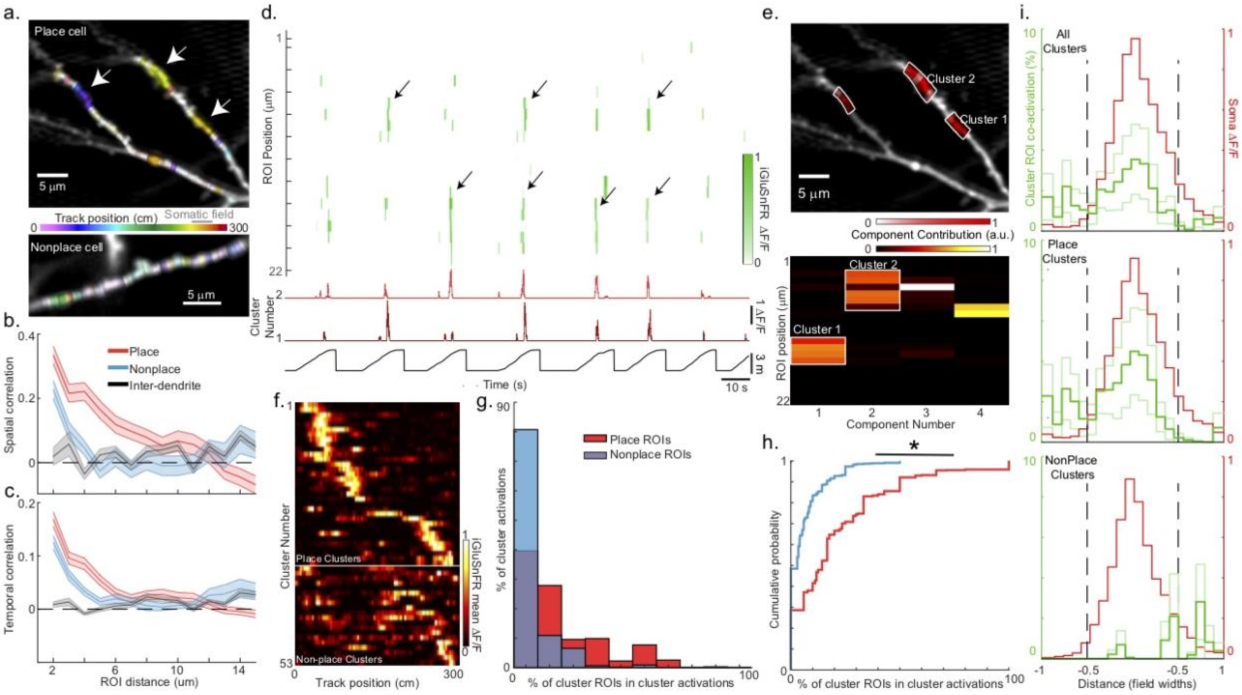

xviii Figure 4.6: Excitatory inputs are more temporally co-active and anatomically clustered in the somatic place field versus out.

a. Dendritic segments from a place cell (top) and nonplace cell (bottom) with ROIs colored according to the center of mass of each ROI's mean ΔF/F map. The brightness indicates peak ΔF/F value in the mean ΔF/F map divided by the spatial dispersion. Track location of somatic place field for place cell (top) shown in grey.

b. Spatial correlation (Pearson's correlation) between the mean ΔF/F maps of all pairs of active ROIs on a single branch versus the dendritic distance between the pairs of ROIs, averaged over all branches from place (red) or nonplace (blue) cells. Inter-dendrite spatial correlation versus

Euclidean distance for pairs of ROIs that belonged to different branches co-recorded in the same field, averaged over all pairs of branches from all dendritic iGluSnFR recordings (black).

c. Temporal correlation versus dendritic distance plots calculated as in b, except significant transient only traces were used instead of mean ΔF/F maps.

d. Matrix of significant iGluSnFR ΔF/F transients vs time traces (green, 100 ms bins) for 22 neighboring ROIs from the top branch shown in **a** (top) acquired during linear track navigation (track position at bottom, black). Numerous co-active and anatomically clustered ROI events are shown with arrows. Cluster ΔF/F vs time traces for the 2 clusters from **e** (bottom) shown in red.

e. Bottom, non-negative independent components for the matrix shown in **d** (top), with 2 functional clusters highlighted in white. Top, Dendritic segments shown in a, but ROIs belonging to 3 different functional clusters are highlighted in white.

f. Mean cluster iGluSnFR ΔF/F versus track position across all traversals of a single session (mean cluster map) for all functional clusters (each row represents single cluster mean ΔF/F) from all place and nonplace cells. Plotted via cross-validation within each cluster category.

g. Histogram of percent of place (red) or nonplace (blue) ROIs that were part of a cluster that were co-active during a cluster activation (non-zero cluster ΔF/F).

h. Cumulative probability from histograms shown in **g**. * p=2.7e-117, Rank-sum test. **i.** Mean cluster ROI co-activation (green, percentage of cluster activations with >70% cluster ROI co-activation) as a function of distance from the center of the mean somatic place field (red) for all clusters (top), all place clusters (middle) and all nonplace clusters (bottom). Mean (dark green) ± SE (light green).

We then sought to determine whether the groups of nearby ROIs (~10 µm) with similar spatial tuning were also likely to be co-active in time in place cells. For each dendritic branch, we applied independent component analysis (see Methods) to the ROI iGluSnFR ΔF/F traces. We found that the ROIs making up the dominant components were often co-active in time and grouped in close proximity along the branch (Figure 4.6d,e); we defined such groups as functional clusters (see Methods; cluster size 4-9 ROIs, 4.5±0.94 ROIs, mean±std; 20.6±20.7% (SD) of cluster ROIs co-active during any cluster activation; 39 clusters from 23 place cells; 0.90±1.1 (SD) clusters/branch; 26.8% [95% bci: 23.5% 28.1%] of ROIs in place cells were in clusters, significantly greater than 5.9% [4.6% 6.5%] from shuffle distribution, χ_{12}=139.2, p~0). Interestingly, a greater percentage of place cell ROIs were in functional clusters versus nonplace cell ROIs (26.8% [bci 23.5-28.1%] vs 18.7% [bci 14.9-20.3%], 1.4x increase, LR test, χ_1^2=8.1, p=0.004). In both cell types, approximately 2/3 of clusters had place fields (place-clusters) and ~1/3 did not (active-non-place clusters) (Figure 4f.6), and during a cluster ROI activation (non-zero cluster ΔF/F) place ROIs that were part of the cluster were more co-active than nonplace ROIs (p=2.7e-117, Rank-sum test, Figure 4.6g,h). Place-ROIs were therefore more likely to be part of a cluster and co-active versus non-place ROIs (Figure 4.6f-h). Importantly, in place cells, 44% (98/224) of place ROIs were in clusters, which was greater than the 14.6% expected by chance (χ_{12}=57.5, p=3.4e-14, likelihood ratio test). Thus, place cell dendrites contained clusters of nearby place-ROIs (<~10 µm; nearly half of all place-ROIs) with similar spatial selectivity that were often co-active in time.

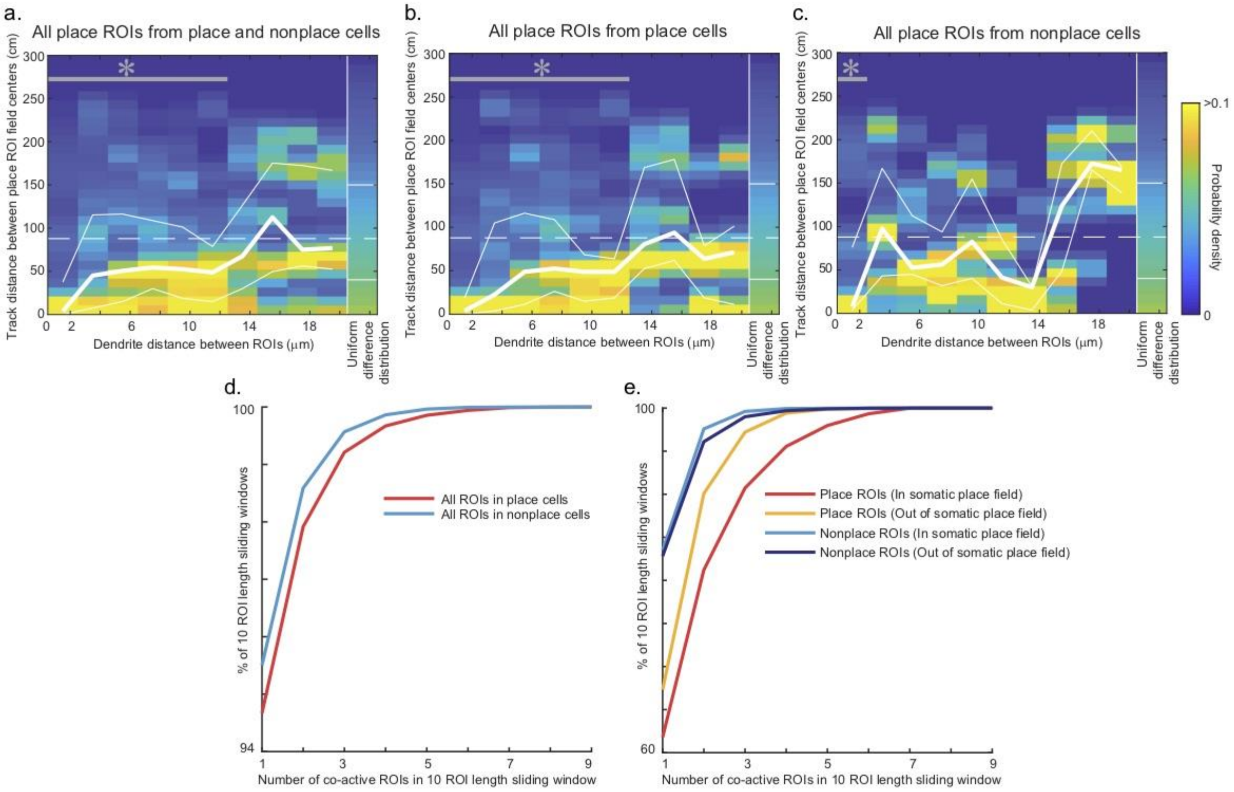

xix Figure 4.7: Further characterization of functional clustering of ROIs in place cells and place fields.

a. Track distance between place ROI field centers (distance between COM of mean ΔF/F maps) of all pairs of place ROIs on a single branch versus the dendritic distance between the pairs of ROIs, averaged over all branches from place and nonplace cells. Colors indicate probability density of ROI pairs (normalized in each column separately) and white lines indicate median ± 1 quartile of track distance vs dendrite distance. Grey line indicates dendritic distances with track distance distributions significantly different (Kolmogorov-Smirnov test, $p<0.0025$, Bonferroni corrected alpha<0.05) from uniform difference distribution shown in last column, with median track distance from uniform difference distribution shown with white dashed line.

b. Same as **a**, but for all pairs of place ROIs from place cells.

c. Same as **a**, but for all pairs of place ROIs from nonplace cells.

d. Cumulative probability from histograms of number of co-active ROIs in 10 ROI length sliding windows (see Methods) from place (red) or nonplace (blue) cells; *p~0 Rank-sum test. **e.** Cumulative probability from histograms of number of co-active ROIs in 10 ROI length sliding windows (see Methods) from place ROIs or nonplace ROIs, with sliding windows either inside or outside of somatic place field.

We then asked where cluster ROI activations occurred with respect to the somatic place field, and whether place- versus active-non-place clusters differentially contributed to total in-field excitatory input. For place cells, we plotted cluster ROI co-activations (the percent of time during cluster ROI activations in which >70% of ROIs in each cluster were co-active) as a function of distance from the somatic place field (Figure 4.6i). Interestingly, we observed a trend in which cluster ROIs displayed greater co-activation inside versus outside the field (2.0% inside vs 1.3% outside; similar shape as in Figure 4.5b), and this in-field increase was mostly due to place-clusters (2.5% inside vs 1.4% outside). Similar results were found using a separate sliding window approach to define clusters (Figure 4.7d,e). Therefore, clusters of nearby place-ROIs (<~10 µm) with similar spatial tuning were more temporally co-active inside versus outside the somatic place field, supporting the fourth hypothesis above.

4.4 Discussion

Here we established optical methods to record glutamate synaptic input to CA1 place cell dendrites with micron-scale spatial resolution and single vesicle detection efficiency in mice navigating along familiar linear tracks (Figure 4.1). We found that dendrites of individual place cells received excitatory input at track locations both inside and outside the somatic place field(Harvey, Collman et al. 2009, Lee, Lin et al. 2012, Bittner, Grienberger et al. 2015, Bittner, Milstein et al. 2017), with many micron-scale dendritic ROIs receiving highly spatially tuned excitatory input and others receiving input with little spatial tuning or no detectable input (Figure 4.4f-h). On average, place cells received slightly less total excitation versus non-place cells (Figure 4.4l). In place cells, however, two general features of the in-field excitatory inputs suggested mechanisms of somatic place firing that were previously unknown: 1. Greater total excitatory input inside versus outside of the somatic place field (Figure 4.5) and 2. More temporally co-active, dendritically clustered ROIs (<~10 µm) inside versus outside the somatic place field (Figure 4.6).

Excitatory input to the proximal dendrites recorded here provides most of the drive for CA1 place firing(Davoudi and Foster 2019), and here we showed that most of the in-field increase in total excitation was derived from place-ROIs with similar fields as the somatic field (Figure 3b). Thus, a significant amount of the CA1 place code in familiar environments appears to be inherited through integration of input from CA2/3 place cells, rather than being formed through integration of non-spatial CA2/3 neurons. This suggests that many CA1 place cells are part of multi-brain-region cell assemblies forming representations of specific locations. Importantly, however, our results do not rule out additional contributions to place firing from other mechanisms or inputs, for example from in-field disinhibition(Ego-Stengel and Wilson 2007, Wilent and Nitz 2007, Ahmed and Mehta 2009), selective changes in post-synaptic strength(Bittner, Grienberger et al. 2015, Bittner, Milstein et al. 2017, Sheffield, Adoff et al. 2017, Sheffield and Dombeck 2019) or from distal inputs(Hafting, Fyhn et al. 2005).

We also found that the in-field total increase in excitatory input was due to a greater *number* of place-ROIs with spatial tuning overlapping the somatic field (Figure 4.5c,d). The increased number originated from both isolated single place-ROIs (49% of the 107 place ROIs overlapping the somatic field) and clusters of co-active adjacent place-ROIs with similar fields (51% of the 107 place ROIs overlapping the somatic field). The increased number of single isolated place-ROIs could be interpreted in different ways: 1. We were able to detect nearly all glutamate released onto place cells, and therefore the increased in-field number was due to a greater number of place-tuned-inputs releasing glutamate, or 2. We were unable to detect a large fraction of small glutamate release events onto place cells and the increased in-field number was due to increased detection efficiency of stronger in-field-tuned-inputs releasing more glutamate. However, the second interpretation seems unlikely given our estimate that we could observe ~80% (Figure 4.1h, u) of single vesicle release events *in vivo* (Figures 4.1h,u), and our observation that the mean in-field ΔF/F was not significantly different than out-of-field (Figure 4.5e,f). Our quantification of iGluSnFR transients presumably from single vesicles was also in agreement with recent literature describing the spatial extent, amplitude and duration of such transients(Soares, Lee et al. 2017, Jensen, Zheng et al. 2019, Soares, Trotter et al. 2019). Additionally, our estimate of 0.10 vesicles/(sec*µm) arriving on CA1 dendrites using iGluSnFR measurements is within the range of values estimated using different methods(Bolshakov and Siegelbaum 1995, Megias, Emri et al. 2001, Routh, Johnston et al. 2009, Holderith, Lorincz et al. 2012, Mizuseki, Royer et al. 2012), further suggesting that we are able to detect most excitatory input. Thus, our data and analysis are more consistent with the first interpretation, indicating that place firing is driven in part by an increased number of place-tuned excitatory inputs releasing glutamate in the somatic field. Such synaptic organization could be formed through genetically-defined wiring(Deguchi, Donato et al. 2011, Druckmann, Feng et al. 2014, Berns, DeNardo et al. 2018), new synapse formation to encode new environments(Hill and Zito 2013), and/or stimulus-dependent recruitment of pre-strengthened neuronal ensembles formed through multiple iterations of synaptic plasticity and pruning(Miller 1996, Lee, Lin et al. 2012, Dragoi and Tonegawa 2014, Oh, Parajuli et al. 2015, Sheffield and Dombeck 2019).

Finally, we found that clusters of nearby place-ROIs (<~10 μm) with similar spatial tuning were more temporally co-active inside versus outside the somatic place field (Figure 4.6). The analysis presented above (large spatial extent transients; Figure 4.1p, 4.6d, Figure 4.3c) indicates that these excitatory input events were likely generated by synchronized-release of vesicles from different presynaptic terminals along the dendritic length rather than synchronized-release of many presynaptic vesicles onto a single ROI and spilling over onto adjacent ROIs. Since CA1 neuron dendrites contain voltage-gated channels and NMDA receptors that allow them to produce regenerative (spiking) events to amplify clustered and co-active synaptic input(Golding, Staff et al. 2002, Ariav, Polsky et al. 2003, Gasparini, Migliore et al. 2004, Losonczy and Magee 2006), the clustered co-activation of inputs observed here suggests that such super-linear summation contributes to place firing. This is consistent with previous *in vivo* calcium imaging demonstrating dendritic branch spiking during place firing(Sheffield and Dombeck 2015). The functional organization of excitatory input that we observed is also consistent with local learning rules strengthening local subsets of synapses to store memories, either through LTP(Schiller, Major et al. 2000, Golding, Staff et al. 2002, Losonczy and Magee 2006, Wu and Mel 2009, Smith, Smith et al. 2013, Palmer, Shai et al. 2014, Weber, Andrasfalvy et al. 2016, Sheffield, Adoff et al. 2017, Rossato, Moreno et al. 2018, Sheffield and Dombeck 2019), intracellular signaling(Harvey, Yasuda et al. 2008, Murakoshi and Yasuda 2012), or genetically defined clustered wiring(Deguchi, Donato et al. 2011, Druckmann, Feng et al. 2014) and are difficult to explain using only global plasticity mechanisms(Zhou, Yan et al. 2008, Hill, Varga et al. 2013, Grienberger, Chen et al. 2014, Bittner, Grienberger et al. 2015, Bittner, Milstein et al. 2017). Overall, our results support a new model in which an increased number of synapses from presynaptic neurons with the same field form functional clusters onto CA1 neuron dendrites to drive place specific firing.

4.5 Methods

Animals

9 to 12 weeks old male C57BL/6 (WT, Charles River) mice (20-30 g) were individually housed under a reverse 12 hr light/dark cycle. All experiments were approved by the Northwestern University Animal Care and Use Committee. Behavioral experiments were conducted during the animal's dark cycle.

Mouse surgery and virus injections

Mice were anesthetized (~1-2% Isoflurane) and a small (~0.5–1.0 mm) craniotomy was made over the hippocampus (1.8 mm lateral, 2.3 mm caudal of Bregma). A low titer Cre -virus (AAV1-*CaMKII*-Cre, $1.51\text{x}10_8$ GC/mL, Addgene) was injected (1 injection of ~60 nL at a depth of ~1250 µm below the dural surface using a beveled glass micropipette: ~1-2 MΩ after beveling) in combination with a high titer of flexed-iGluSnFR.A184S virus(Marvin, Scholl et al. 2018) (AAV2/1-hSyn-FLEX.SF-iGluSnFR.A184S, $5.87\text{x}10_{12}$ GC/mL) and flexed-jRGECO1a virus(Dana, Mohar et al. 2016) (AAV1-*hSyn*-FLEX.NES-jRGECO1a, 4.05 x 10_{12} GC/mL) leading to expression of SF-iGluSnFR.A184S and jRGECO1a in a sparse subset of the CA1 pyramidal neuron population. For control GFP imaging experiments, mice were injected following the same sparse labeling protocol, but with flexed GFP virus (AAV1-*pCAG*-FLEX-EGFP-WPRE at $1.55\text{x}10_{13}$ GC/mL and AAV1-*CaMKII*-Cre at $1.51\text{x}10_8$ GC/mL). Mouse water scheduling began the day after virus injections (0.8-1.0 mL/day, and continued through all training and experiments) followed ~7 days later by a hippocampal window and head-plate implantation surgery (as described previously(Dombeck, Harvey et al. 2010, Sheffield, Adoff et al. 2017)). For live slice imaging and glutamate uncaging experiments, mice were injected following the same sparse labeling protocol and allowed to recover for 3 to 4 weeks prior to hippocampal slice preparation.

Behavior and training in virtual reality

We used the same virtual reality and treadmill set-up as previously described(Sheffield, Adoff et al. 2017), consisting of a 1D treadmill and a view angle within the virtual environment straight down the track. Training in a 3 m virtual linear track began ~7 days after window implantation and continued until mice routinely ran along the track to achieve a high reward rate (>~2 rewards/minute); rewards consisted of water (4 µL) delivered as described previously(Dombeck, Harvey et al. 2010, Sheffield, Adoff et al. 2017). Mice were teleported back to the beginning of the track after each reward and after a 1 sec delay. Once this criterion was reached (~5-7 days of virtual reality training), imaging commenced.

Two-photon imaging

A Moveable Objective Microscope (Sutter Instruments) was customized for our imaging experiments. The microscope consisted of a resonant scanning module (Vidrio), a 40×/0.80 NA water immersion objective (LUCPlanFL N, Olympus) and enhanced collection optics. Green iGluSnFR (or GFP) and red jRGECO1a fluorescence were routed to separate GaAsP PMTs (H10770PA-40) using a series of dichroic mirrors and band-pass filters (in order after leaving the back aperture; Semrock): FF665-Di02 long pass dichroic, FF01-680/sp short pass filter, FF560-Di01 long pass dichroic, FF01-510/84 band-pass filter (Green), 620/52 band-pass filter (red). Stray light from the virtual reality monitor was blocked using a custom box surrounding the top of the microscope objective and the overlying dichroic mirror (not including the tube lens, scan lens, galvos or routing mirrors). This box had one hole on top, for entry of the excitation beam, which was covered with a color glass filter (FGL780, Thorlabs) and one hole on bottom for the microscope objective. This bottom hole was sealed using the same loose black rubber tube and tight-fitting metal rings described previously(Dombeck, Harvey et al. 2010). ScanImage 2017 was used for microscope control and acquisition (Vidrio). Ti:Sapphire laser (Chameleon Ultra II, Coherent) light at 920 (for GCaMP6f, GFP) nm and fiber laser (Fidelity-2, Coherent) light at 1070nm were used as the excitation sources for iGluSnFR and jRGECO1a, respectively. Laser average power at the sample (after the objective) was 47-136 mW (920nm; mean: 65mW) or 112-160 mW (1070nm; mean: 138mW). Pockels cells (350-105-02 KD*P, 302RM driver, Conoptics) were used to blank laser excitation at the edges of the field of view. Time-series movies (Somatic: 512x256-512 pixels, [214-281 µm] x [104-284 µm] field of view; dendritic: 512x256-512 pixels, ([40-72 µm]x[25-71 µm] field of view) were acquired at 30-60Hz. A Digidata1440A (Molecular Devices) data acquisition system was used to record (Clampex 10.3) and synchronize position in the linear track, reward timing, and two-photon image frame timing.

Somatic red jRGECO1a fluorescence time-series were acquired from the sparsely labeled cell bodies (5.6±0.2 minutes/time-series, 22.5±1.5 track traversals/time-series, mean±SE). To maximize the number of place cells recorded, cells that were active along the track were targeted in most recordings, though other somas were often in the imaging field. The imaging plane and wavelengths were then adjusted to acquire dendritic green iGluSnFR fluorescence time-series (~4.7±0.2 minutes/time-series, 19.8±1.3 track traversals/time-series, mean±SE). It was possible online to follow dendrites from the targeted cell of interest to a more distal dendritic site, though offline analysis and tracing was later performed to confirm the parent cell body of the recorded dendrites. Dendritic recording planes were selected based only on dendritic branch morphology to obtain recordings from the longest dendritic branches possible, no online functional iGluSnFR measures were used to select branches. Other dendritic branches were often in the dendritic imaging field, and these dendrites were included in cell type specific analysis (Figure 2-4; Extended Data Figure 3) when they could be traced to one of the somas recorded in the somatic time-series (using z-series acquired at the end of the session, see below). Even if these other dendrites could not be traced to recorded somas, they were included in analysis that did not require somatic recordings (Figure 1; Extended Data Figure 2). In a subset of recordings, after dendritic time-series acquisition, a second time-series recording was acquired from the soma to confirm the stability of the somatic spatial firing pattern. For control GFP recordings, no somatic recordings were made, but dendritic recording planes were selected using the same criteria as with iGluSnFR.

After time-series acquisition, z-series were acquired from each field of view from the external capsule fiber surface through the proximal apical dendrite (2 µm between planes) and motion corrected as described previously(Sheffield and Dombeck 2015). All dendritic branches recorded during time-series were traced offline in all 46 cells included here from motion corrected z-series using Simple Neurite Tracer in Fiji (ImageJ). This method was used to identify the parent soma of each recorded dendrite by tracing them unambiguously back to the soma in the z-series. All dendritic distances from soma represent distance traveled along the neurite. Any ambiguous cases (i.e. crossing dendrites that could not be resolved) were not included in cell type specific analysis and the dendrites were then only included in analysis that did not require somatic recordings (Figure 1; Extended Data Figure 2).

Image processing

Imaging data was analyzed on a Dell Power Edge 720 Server using ImageJ and custom software written in MATLAB. Motion correction of somatic plane jRGECO1a time-series was performed using whole frame cross-correlation, as described previously(Dombeck, Harvey et al. 2010). Motion correction of dendritic plane iGluSnFR (or GFP) time-series was performed using NoRMCorre(Pnevmatikakis and Giovannucci 2017) and whole frame cross-correlation(Dombeck, Harvey et al. 2010). Dendritic time-series often required multiple rounds of motion correction (in series) to remove finer and finer motion. This was accomplished using different x and y shift values and/or different reference frames (typically an image built from averaging multiple frames) on each round. In some cases, the dendritic time-series were cropped in the x and y dimensions around either single dendritic branches, or multiple dendritic branches in the same region of the field of view, and subsequent rounds of motion correction were performed on the cropped time-series. Once dendritic movements were not reduced by further rounds of motion correction, the time-series were visually inspected and either included if in plane movements were small in comparison to the structures of interest (width of the dendrites) and out of plane (z) movement was minimal, or excluded if in plane movements were larger than the structures of interest or if out of plane movement was visible. These criteria were strictly applied and were biased towards rejecting any borderline cases; ~2/3 of acquired dendritic time-series were able to be sufficiently motion corrected and included for further analysis. Thus, our inclusion criteria only focused on the structure (movement) of the dendritic branches, and did not include any functional iGluSnFR measures. The same motion correction and inclusion criteria were applied to the GFP control data.

ROI selection and fluorescent transient analysis

Somatic jRGECO1a time-series analysis: ROIs were selected by hand on the mean soma images to closely follow the outline of the soma. A background ROI to define the background fluorescence for each somatic ROI was drawn in a nearby dark region of the image. Fluorescence versus time traces were generated for each ROI by averaging the pixel values in each ROI in each frame. Each background ROI fluorescence trace was subtracted from its matching somatic ROI fluorescence trace (timepoint by timepoint). ΔF/F versus time traces were then generated for each background subtracted somatic ROI trace similar to previous methods(Dombeck, Harvey et al. 2010). Briefly, slow changes in the fluorescence traces were removed by examining the distribution of fluorescence in a ±3 sec interval around each sample in the trace and normalized by the 8th percentile value. Only periods of these traces when the mice were running along the track (velocity >4cm/sec, length of run periods>40cm) were included for further analysis. The baseline corrected soma fluorescence traces (during track running periods) were then subjected to the analysis of the ratio of positive to negative going transients of various amplitudes and durations described previously(Dombeck, Khabbaz et al. 2007). We used this analysis to identify significant ΔF/F transients with <0.1% false positive error rates; these identified significant transients were used in the subsequent analysis.

Dendritic iGluSnFR (and control GFP) time-series analysis: Dendritic ROIs from iGluSnFR or GFP labeled dendrites were defined along each dendritic branch separately by first drawing an ROI by hand that closely followed the outline of the branch. 1 µm segments along the dendritic branch (within the outline) were then identified using custom code. These segments defined the 1 µm ROIs (Figure 1m,q, 2e, 4a) used for all subsequent dendritic analysis. A background ROI to define the background fluorescence for each dendritic branch was drawn in a nearby dark region of the image (with size similar to the dendritic branch). Fluorescence versus time traces were generated for each ROI by averaging the pixel values in each ROI in each frame. Each background ROI fluorescence trace was subtracted from each 1 µm ROI fluorescence trace (timepoint by timepoint; background ROI from matching branch). Slow changes in the fluorescence traces were removed by examining the distribution of fluorescence in a ±1.5 sec interval around each sample in the trace and normalized by the 8th percentile value. Only periods of these traces when the mice were running along the track (velocity >4cm/sec, length of run periods>40cm) were included for further analysis. Several exclusion criteria were then defined to handle ROIs with weak fluorescence signal, ROIs with out of plane movements and time periods in which large out plane movements were observed across many ROIs: 1. ROIs at ends of dendritic segments were not included for further analysis since they were most prone to out of plane movements. 2. ROIs with mean fluorescence of <1.5 counts were too dim for an accurate measure of $\Delta F/F$ and were excluded from further analysis; these criteria excluded 8.6% of ROIs. 3. Time periods (frames) in which large out of plane movements were observed across many ROIs were excluded from further analysis; these periods were identified by calculating the mean fluorescence versus time trace across all ROIs in a field, calculating the STD of this trace, and then excluding any time periods in which the fluorescence was >2STD from the mean in the positive direction or >1STD from the mean in the negative direction; this excluded 0.3% of frames during track running.

The remaining baseline corrected dendritic ROI fluorescence traces were then subjected to the analysis of the ratio of positive to negative going transients of various amplitudes and durations described previously(Dombeck, Khabbaz et al. 2007). When estimating baseline fluorescence (F) in this analysis, we used the positive going noise above the mean F to measure noise std (keeping the original mean F in the std calculation to estimate std of the original trace) to avoid an underestimation of std caused by a floor effect. We used this analysis to identify significant ΔF/F transients with <0.1% false positive error rates; these identified significant transients were used in the subsequent analysis. ΔF/F versus time traces consisted of these significant transients with non-significant transient periods set to 0 (significant transient only traces). The above analysis was performed identically on the GFP and iGluSnFR labeled dendrites.

The GFP significant transient only traces consisted of noise, with only occasional false positive transients occurring at the expected false positive rate (Figure 1q-s). The distribution of GFP noise transient amplitudes were smaller (Figure 1u) and almost completely non-overlapped with the iGluSnFR transient amplitudes (significant transient only traces). Applying a minimum amplitude threshold of 0.40 ΔF/F left only 5% of GFP transients, but 98% of iGluSnFR transients; these remaining significant iGluSnFR transients were used for all subsequent analysis and the small percentage (2%) of iGluSnFR transients less than the amplitude threshold were set to 0 in the significant transient only traces.

Transient amplitude peak and duration (Figure 1t,u) were characterized for every significant transient from each included ROI. The duration was defined as the full duration of the transient and the peak was defined as the peak ΔF/F within this duration. To estimate the mean amount of excitatory input received by the iGluSnFR labeled dendrites in vivo, we calculated the integral (area under the transients) of the significant transient only ΔF/F traces from all ROIs, and divided by the number of ROIs and the total recording time to arrive at the average integral per second per 1-µm ROI.

iGluSnFR transient event dendritic length and peak amplitude (Extended Data Figure 2a,b) were analyzed separately on each dendritic branch (only branches >= 8 ROIs were included; event length measurements required different analysis compared to Figures 1t,u). For each branch we generated a matrix in which each row corresponded to a single ROI on the branch and the order of the rows corresponded to the position of the ROIs on the branch (i.e. neighboring rows corresponded to neighboring ROIs on the branch). The columns corresponded to 100ms time-bins, and the values of the matrix elements corresponded to average ΔF/F (from significant transient only traces) over the 100ms time-bin. Transient events were defined as contiguous co-active (non-0 ΔF/F) ROIs. For transients restricted to 1 ROI, the length was defined as 1 µm and the peak amplitude as the peak ΔF/F value within the active time-points. For transients extending to 2 or more ROIs, the length was defined by the time-point(s) when the largest number of contiguous ROIs were co-active, and the peak amplitude was defined as the peak ΔF/F value (of any of the co-active ROIs) within those timepoints.

The mean image of iGluSnFR transients restricted to 1 µm ROIs (Extended Data Figure 2d) was generated by first identifying the time-series fluorescence (F) frame at which the transient peak occurred and excising a 4 µm by 4 µm region surrounding the transient pixels. This image was then transformed into a ΔF/F image on a pixel by pixel basis. For each pixel in the peak image, a fluorescence versus time trace was generated from the peak frame back to the preceding 0.6 seconds of the time-series. This trace was normalized by the 8th percentile of the pixel values (excluding the peak), and then the median of the resulting normalized trace was subtracted to arrive at a ΔF/F trace. The peak ΔF/F of this trace (the last time point) was assigned as the pixel value in the peak ΔF/F image. The ΔF/F images for each transient were then averaged together by first rotating each ΔF/F image to align the dendritic branch segment along the horizontal axis, and then calculating the center of mass of the ΔF/F image (center of mass of image after thresholding ΔF/F> 0). To align the dendritic segments across images, if the site of the center of mass was below the mean horizontal axis of the dendrite, then the image was rotated 180°. The mean ΔF/F image was then generated by aligning the ΔF/F images on their center of masses and calculating the pixel by pixel mean ΔF/F value.

Defining place and nonplace cells

Place cells were identified by first calculating the mean of the significant transient only trace as a function of track position using 80 spatial bins (mean ΔF/F map; Figure 2c,d) and then smoothing this mean ΔF/F map (3 bin boxcar). The original significant transient only trace (versus time) was then shuffled to randomize the transients with respect to track position, and a mean ΔF/F map (smoothed using 3 bin boxcar) was generated for the shuffled trace. This was repeated 10,000 times to generate 10,000 mean shuffled ΔF/F maps. We then identified significant spatial bins from the original mean ΔF/F map as bins in which ΔF/F values were greater than the ΔF/F values in 9,500 of the 10,000 corresponding bins of mean shuffled ΔF/F maps ($p<0.05$). Place fields were identified as spatial regions that consisted of 5-46 contiguous significant spatial bins and displayed a significant transient within the region on >33% of track traversals. The bounds of significant fields were extended until the smoothed (3 bin boxcar) florescence map descended to 10% of the peak florescence or began to increase(Hafting, Fyhn et al. 2008). When place cells had more than one place field, each field was treated separately (20 place cells had 1 field, 3 had 2 or more fields). Nonplace cells were identified as any cells without a place field based on the above criteria; nonplace cells were further separated into silent cells and active nonplace cells based on an activity threshold (silent: significant transients < 1% of time running on track; active nonplace: significant transients > 1% of time running on track). In total, 1192 1 µm ROIs were recorded from place cells and 749 1 µm ROIs were recorded in nonplace cells. These total lengths represent a significant fraction of the total length of proximal dendrites in a single CA1 pyramidal neuron(Megias, Emri et al. 2001, Routh, Johnston et al. 2009), and therefore by combining dendritic recordings over multiple cells based on cell type we were able to generate a fairly complete description of the functional organization of excitatory synaptic input to an average place or nonplace cells.

Defining place and nonplace ROIs

Place ROIs were identified by first calculating the mean of the significant transient only trace as a function of track position using 80 spatial bins (mean ΔF/F map; Figure 2f-i) and then smoothing this mean ΔF/F map (3 bin boxcar). The original significant transient only trace (versus time) was then shuffled to randomize the transients with respect to track position, and a mean ΔF/F map (smoothed using 3 bin boxcar) was generated for the shuffled trace. This was repeated 1000 times to generate 1000 mean shuffled ΔF/F maps. We then identified significant spatial bins from the original mean ΔF/F map as bins in which ΔF/F values were greater than the ΔF/F values in 950 of the 1000 corresponding bins of mean shuffled ΔF/F maps ($p<0.05$). Place ROIs were identified as spatial regions that consisted of 5-46 contiguous significant spatial bins and displayed a significant transient within the region on >33% of track traversals. The bounds of significant fields were extended until the smoothed (3 bin boxcar) florescence map descended to 10% of the peak florescence or began to increase(Hafting, Fyhn et al. 2008). When place ROIs had more than one place ROI field, each field was treated separately (321 place ROIs had 1 field, 9 had 2 or more fields). Nonplace ROIs were identified as any ROI without a place field based on the above criteria; nonplace ROIs were further separated into silent ROIs and active nonplace ROIs based on an activity threshold (silent: significant transients < 1% of time running on track; active nonplace: significant transients > 1% of time running on track).

Fluorescence changes versus track position analysis

Mean ΔF/F maps were analyzed without smoothing. They were plotted via cross validation (Figures 2d,g-i, 3a,c,d, 4f) by calculating the mean ΔF/F maps for the first half and second half of each session. Sorting order was determined by the peak ΔF/F value in the first half map, and then the second half map was displayed in the plots.

The spatial dispersion (Figures 2k and 4a) of the significant transients of an ROI was defined based on the mean ΔF/F map as:

$$spatial\ dispersion = \frac{\sum_{i=1}^{N} f_i (COM - x_i)^2}{\sum_{i=1}^{N} f_i}$$

Where i is spatial bin number, N is 80 spatial bins, f_i is the ΔF/F value of the ith spatial bin, x_i is the position of the ith spatial bin in cm, and COM is the center of mass of the mean ΔF/F map in cm and is defined as:

$$COM = \frac{\sum_{i=1}^{N} f_i x_i}{\sum_{i=1}^{N} f_i}$$

Mean ΔF/F maps in units of somatic place field width (Figure 3a) were generated by scaling the distance axis in the mean ΔF/F maps by the width of the somatic place field (full width), and then pooling the maps together by centering each at the track location of the somatic place field peak. For place cells with more than 1 place field, mean ΔF/F maps for each field included the track locations before and after the field up to either the edge of the next place field or the track edge (whichever came first). Place fields with one edge at a track edge were included, and the width of these fields was defined as twice the distance from the place field peak to the field edge (field edge not at track edge).

The plots of mean total excitatory input as a function of distance from mean somatic place field center (Figure 3b) were generated by calculating the average ΔF/F across all place and active-nonplace ROIs in each spatial bin (including only spatial bins for each ROI that contained ΔF/F values). Spatial bin size varied as a function of distance from somatic field center so that each bin contained a similar number of datapoints (i.e. larger bins further from field center).

The plot of percentage of place ROIs with place ROI field coverage of binned positions from the center of the mean somatic place field (Figure 3c,d) was generated by calculating the percentage of place ROIs with an ROI field in each spatial bin (including only spatial bins for each place ROI that contained ΔF/F values). The plot of mean ΔF/F per place ROI field versus position from the center of the mean somatic place field (Figure 3e,f) was generated by first assigning all track locations in each place ROI field the mean ΔF/F value over the field and then calculating the average of these mean-field ΔF/F values across all place ROI fields in each spatial bin (including only place ROI fields). Spatial bin size varied as a function of distance from somatic field center for both plots (Figure 3c-e) so that each bin contained a similar number of datapoints (i.e. larger bins further from field center).

Functional dendritic organization analysis

Images in Figure 4a were generated by coloring each ROI according to the center of mass of its mean ΔF/F map. The brightness of each ROI was defined by the peak ΔF/F value in the mean ΔF/F map divided by the spatial dispersion.

Spatial correlation versus distance (Figure 4b) was calculated as the Pearson's correlation between the mean ΔF/F maps of all pairs of active ROIs (excluding silent ROIs) on a single branch versus the dendritic distance between the pairs of ROIs. Average spatial correlation versus distance plots were generated by averaging over all pairs belonging to place or nonplace cells. Inter-dendrite spatial correlation versus distance was calculated in the same way, except pairs of ROIs belonged to different branches that were co-recorded in the same field and distance was defined as the Euclidean distance between the ROIs. Temporal correlations (Figure 4c) were calculated in the same way, except the significant transient only traces were used instead of mean ΔF/F maps.

Sliding window ROI co-activation analysis (Extended Data Figure 3d,e) was performed separately on each dendritic branch (only branches > 10 ROIs were included). For each branch we generated a matrix in which each row corresponded to a single ROI on the branch and the order of the rows corresponded to the position of the ROIs on the branch (i.e. neighboring rows corresponded to neighboring ROIs on the branch). The columns corresponded to 100ms time-bins, and the values of the matrix elements corresponded to average ΔF/F (from significant transient only traces) over the 100ms time-bin. The number of co-active ROIs within a window of 10 rows x 1 column was quantified over all possible positions of the window in the matrix. For place versus non-place cells (Extended Data Figure 3d), the resulting histograms of co-active ROIs over all window positions were pool by cell type. For place versus nonplace ROIs in somatic field versus out of somatic field measurements (Extended Data Figure 3e), window positions inside versus outside of the somatic field were pooled separately and only including either place ROIs or nonplace ROIs. At least 1 of the ROI type of interest were required to be present in a given window to be included.

Functional clusters (Figures 4d-i) were defined separately on each dendritic branch (only branches > 8 active ROIs were included). For each branch we generated a matrix in which each row corresponded to a single ROI on the branch and the order of the rows corresponded to the position of the ROIs on the branch (i.e. neighboring rows corresponded to neighboring ROIs on the branch). The columns corresponded to 100ms time-bins, and the values of the matrix elements corresponded to average ΔF/F (from significant transient only traces) over the 100ms time-bin. We then decomposed the matrix into components by reconstruction ICA using PCA as an initial guess. The resulting weight matrix was then made nonnegative by finding the closest nonnegative matrix as measured by the Frobenius norm. The rows in the resulting weight matrix corresponded to ROI number, the columns to independent components, and the values of the matrix elements to contribution of each ROI to each component. Neighboring rows corresponded to neighboring ROIs on the branch, although notably the order of rows has no effect of on the PCA/ICA analysis. Within each component, we normalized the component contributions by the peak ROI component value and then identified all ROIs with values >10% of the peak. Among these highest contributing ROIs, we then defined functional clusters as groups of at least 4 ROIs that were in close proximity: All ROIs in the groups of >4 ROIs were required to be adjacent, with the exception that a gap of 1 ROI between the contributing ROIs was allowed and at least 70% of the ROIs in the functional cluster were required to be contributing ROIs (values >10% of the component peak). All possible numbers of components were tried up to one half the number of active ROIs on the branch, and any detected clusters within these components were used for further analysis.

Cluster ΔF/F traces in time (Figure 4d) consisted of the weighted sum of the iGluSnFR ΔF/F traces of the ROIs in each cluster, with weighting determined by each ROIs non-negative independent component contribution. Mean cluster ΔF/F maps were generated by calculating the mean cluster ΔF/F traces as a function of track position over all traversals using 80 spatial bins; these cluster maps were plotted via cross validation (Figures 4f), as described above (see “Fluorescence changes versus track position analysis” section). Place and nonplace clusters were defined using the same methods as described above for individual ROIs (see "Defining place and nonplace ROIs" section). Cluster activation was defined as anytime a cluster component trace was >0; that is, whenever any ROI in the cluster was active. The percent of cluster ROIs (place or nonplace ROIs) that were co-active in each cluster activation (Figures 4g) was defined as the fraction of (place or nonplace) ROIs active during any cluster activation. Plots of cluster co-activation vs distance from mean somatic field (Figure 4i) were made by making spatial bins in units of somatic field widths, and then calculating the percentage of time during cluster activations in which >70% of cluster ROIs were co-activated. Spatial bin size varied as a function of distance from somatic field center so that each bin contained the same amount of data (i.e. larger bins further from field center).

Is any glutamate detected from synapses onto neighboring neurons?

An important limitation of our approach is that we are unable to unambiguously identify the synapses providing the glutamate. A key point for interpreting our results is whether our methods are detecting glutamate from synapses formed onto the imaged dendrites, or spillover from adjacent synapses onto unlabeled dendrites of other neurons. The following analyses presented here suggest that it is unlikely that much glutamate from synapses onto adjacent unlabeled dendrites of other neurons was detected at our iGluSnFR labeled dendrites:

1. Our observations indicate that most glutamate spilling over beyond the synapse and detected by iGluSnFR is highly localized (~1 µm) on CA1 dendrites during behavior (Extended Data Figure 2a,d), and therefore any glutamate spilling over from neighboring neurons would likely generate a weak and undetectable change in fluorescence.

2. We observed greater total excitatory input inside versus outside of the somatic place field (Figure 3). Since hippocampal place cells are not topographically organized(Redish, Battaglia et al. 2001, Dombeck, Harvey et al. 2010), the glutamate spillover from neighboring neurons would not be expected to have coherent spatial tuning, making it difficult to explain our finding of increased input in the somatic field with random sampling of neighboring neuron synapses.

3. Our estimate of 0.10 vesicles/(sec*µm) arriving at CA1 pyramidal neuron dendrites during behavior is within the range of rates that can be estimated (0.17±0.28 vesicles/(sec*µm)) using CA3/2 firing rates during navigation, the number of CA3/2 synapses per micron of CA1 dendrite, and the vesicle release probability at these synapses. It is unlikely that these independent methods for estimating excitatory input rate would agree if a large amount of the glutamate we detected here originated from synapses onto neighboring neurons.

4. Since significant glutamate spillover would be expected to increase signal correlations between ROIs on different dendritic branches, our observation of a flat correlation versus inter-dendrite ROI distance (Figure 4b,c, black traces) down to 2-3 microns (the closest pairs measured), rather than an increasing correlation with decreasing distance, indicates little glutamate spillover down to at least 2-3 microns.

Hippocampal slice preparation

Transverse hippocampal slices (~300 □m) were prepared from iGluSnFR virus injected male C57BL/6J mice (same age mice and same injection procedures as used for *in vivo* experiments; see “Mouse surgery and virus injections” section above) using a vibrating microtome (VT1200S; Leica Systems, Germany). For GCaMP6 imaging and uncaging experiments, the same virus injection procedures were used as described for iGluSnFR, but AAV1-*hSyn*-flex-GCaMP6f or s,

1.4×10^{13} GC/mL) was used instead. Animals were anaesthetized with isoflurane and perfused with ice-cold sucrose artificial cerebrospinal fluid (ACSF) solution containing (in mM): 85 NaCl, 2.5 KCl, 1.25 NaH2PO4, 25 NaHCO3, 25 glucose, 75 sucrose, 0.5 CaCl2, and 4 MgCl2, saturated with 95% O2 and 5% CO2, 3 Sodium Pyruvate, 1 Ascorbic Acid. After slices were cut (in the same sucrose ACSF used for perfusion) they were transferred to a warm (32 °C) incubation chamber with oxygen bubbled ACSF containing (in mM): 125 NaCl, 2.5 KCl, 25 NaHCO3, 1.25 NaH2PO4, 1 MgCl2, 2 CaCl2 and 25 glucose, for 25 minutes after which time they were allowed to recover at room temperature in oxygenated ACSF for 1 hour before imaging and/or intracellular patch recording.

Slice imaging, intracellular recording and glutamate uncaging

Glutamate uncaging and imaging of hippocampal CA1 pyramidal neuron basal and proximal oblique dendrites *in vitro* were performed on an Ultima two-photon laser scanning microscope (Bruker, former Prairie Technologies, Middleton, WI) equipped with duel galvanometers driving two Ti:Sapphire lasers (Chameleon, Coherent). The lasers were tuned to 920 nm for iGluSnFR imaging (Figure 1e-j, Extended Data Figure 2f, i-l; or for GCaMP6 imaging, Extended Data Figure 1) imaging or 840 nm for Alexa 594 imaging, and 720 nm for glutamate uncaging, and the intensity of each laser was independently controlled with electro-optical modulators (Conoptics). Imaging and uncaging were performed with an upright Zeiss Axiovert microscope using a 40x, 1.0 numerical aperture water immersion objective. During imaging and uncaging, slices were maintained at a constant temperature ranging from 30–34 °C (mean 32.4 °C and bathed in recirculating oxygen bubbled ACSF containing 3 mM MNI-caged L glutamate (4-methoxy-7-nitroindolinyl-caged L-glutamate, Tocris), 1 μM TTX (Tocris Bioscience) and 2 uM of GABAA receptor antagonist SR-95531 (Tocris Bioscience); in a subset of GCaMP6 uncaging and imaging experiments, Mg^{2+} was not included in the ACSF (0 Mg^{2+}, Extended Data Figure 1). MNI-glutamate was uncaged using 500 □s pulses (10-70 mW after the objective) with a 120 □s interstimulus interval for multi-site stimulation (Figure 1a-j, Extended Data Figure 1, 2). All dendritic branches were 25-75 □m from the slice surface. Intracellular patch recordings were made using patch electrodes (3–6 MΩ) filled with intracellular solution containing the following (in mM): 115 K-gluconate, 20 KCl, 10 HEPES, 10 Na_2 creatine phosphate, 2 Mg-ATP, 0.3 Na-GTP. For uncaging experiments without iGluSnFR (Figure 1a-c), 0.025 mM Alexa 594 was included in the pipette. Time-series movies were acquired at >15 Hz (mean 43.5 Hz) for the duration of uncaging events and were analyzed with MATLAB (MathWorks) and ImageJ following motion correction (see "Slice ROI selection and fluorescent transient analysis" section).

Slice ROI selection and fluorescent transient analysis

Slice time-series movies were motion corrected using whole-frame cross correlation to remove any slow drift. 1 □m ROI selection and generation of significant transient only traces for each ROI were performed using the same procedure as used for *in vivo* imaging dendritic datasets (see "ROI selection and fluorescent transient analysis" section). iGluSnFR transient amplitude peak (Figure 1h), duration (Figure 1i) and integral (Figure 1j) were characterized for every significant transient generated by single 25-29mW uncaging stimulations (mimicking single vesicle release)—96% (43/45) of these stimulations generated significant transients. For peak and duration, if significant transients were generated in more than 1 ROI, the ROI with the largest amplitude was used for analysis. The duration was defined as the full duration of the transient and the peak was defined as the peak ΔF/F within this duration. For the integral of the transients generated by single 25-29mW uncaging stimulations, we calculated the integral of all significant transients (i.e. if significant transients were generated in more than 1 ROI, the integral included all responding ROIs).

Chapter 5 General Discussion

5.1 Summary

The ability to learn and remember new experiences is a critical feature of the central nervous system and is the foundation upon which we define ourselves. It has been widely accepted that memory formation and storage depend on the strengthening of the neural connections between neurons through experience-dependent plasticity mechanisms. This principle, postulated by Donald Hebb in 1949, states that if one neuron repeatedly participates in the activation of another interconnected neuron, the connection between these two neurons will become strengthened (Hebb 1949)(1950). Long-term potentiation (LTP) of synaptic strength that is dependent on the NMDA receptor represents the classic example of a Hebbian synaptic learning rule. Since the original discovery of the phenomenon of LTP in the rabbit hippocampus it has come to be considered the fundamental rule by which the brain is wired. In the rodent hippocampus, pyramidal neurons in the CA1 region known as place cells show location-specific activity patterns (O'Keefe and Dostrovsky 1971) and provide a means to assess the mechanisms of memory processing from synapse to behavior. Although a large body of studies have implicated a role for Hebbian synaptic plasticity rules in the formation of place fields (Blum and Abbott 1996, Tsien, Huerta et al. 1996), the precise mechanisms underlying this transformation remains unknown. Despite the prominence of Hebbian synaptic plasticity rules in models of place field formation, other modes of plasticity have emerged in the form of local Hebbian, anti-Hebbian, and non-Hebbian learning rules(Bittner, Milstein et al. 2017, Sheffield, Adoff et al. 2017, Schiller, Berlin et al. 2018). These mechanisms feature global and local dendritic spikes as a prominent mediator of postsynaptic plasticity and may act over much longer timescales then predicted by conventional Hebbian plasticity(Bittner, Milstein et al. 2017, Sheffield, Adoff et al.

2017). In chapter 2 of my thesis, we explored how local regenerative dendritic events contribute to the de novo formation of place fields by using virtual reality (VR) and two-photon functional imaging to directly monitor dendritic calcium activity during exposure to novel environments.

5.2 Local dendritic spikes contribute to de novo Place field formation in a subset of Place cells

In these experiments it was found that in a subset of CA1 pyramidal neurons, place fields are delayed in their formation and appear only after the animal has traversed the novel several times. Exposure to a new environment alters the configuration of active synapses onto the dendrites of a CA1 neurons whose activation is insufficient to drive somatic firing. This is likely due to a bias toward weaker synapses in this new synaptic distribution (Sheffield and Dombeck 2019). The sudden emergence of place fields during multiple traversals of the environment, without any prior corresponding somatic activity suggests a plasticity mechanism different from conventional Hebbian mechanisms most likely mediated through local synaptic plasticity by the generation of dendritic spikes. Indeed, we found that in these delayed place cells, local calcium transients in the basal dendrites appeared at the eventual location of the somatic place field several laps before the occurrence of somatic activity. These events were reminiscent of dendritically generated NMDA spikes which may form through the coincident activation of nearby synapses on the same dendritic branch at the same environmental location. This is supported by in vitro experiments using glutamate uncaging on GCaMP labeled CA1 basal dendrites in hippocampal brain slices showing that the local dendritic calcium spikes seen in vivo likely result from concurrent activation of spatially clustered inputs(Sheffield, Adoff et al. 2017). Also, knocking out NMDA receptor functionality specifically in the CA1 region led to a reduction in the number of local dendritic spikes as well as general place field formation across the CA1 population, suggesting that NMDA-dependent plasticity strongly contributes to the formation of some place cells. These results imply a role for clustered coincident inputs and dendritically generated NMDA spikes in facilitating experience dependent place specificity without somatic activity.

While there is now abundant evidence that synaptic arrangements in CA1 dendritic branches may not be randomly distributed (Druckmann, Feng et al. 2014, Sheffield, Adoff et al. 2017, Bloss, Cembrowski et al. 2018), evidence for the existence of local input clustering in vivo is contradictory(Jia, Rochefort et al. 2010) (Varga, Jia et al. 2011, Takahashi, Kitamura et al. 2012, Chen, Wardill et al. 2013) (Wilson, Whitney et al. 2016, Iacaruso, Gasler et al. 2017). Given this disparity of findings on in vivo synapse distribution and activation properties, it is necessary to use the appropriate tools to establish whether synaptic input carrying similar information arrives onto the same or different CA1 dendrites. With the recent development of the glutamate sensor iGluSnFR, there is now a means to explore the spatial patterns of dendritic inputs from presynaptic cell assemblies in vivo. In chapter 4 of my thesis, I used this indicator to investigate some of the most pressing questions in the field such as how excitatory synaptic input to place cells is organized along a given dendrite and whether this organization contributes to place field firing.

5.3 Place cells receive more excitatory input at the location of the somatic place field.

It was recently found that that place fields can be formed at any position on a track by inducing a plateau potential at that specific location (Bittner, Grienberger et al. 2015). This suggests that each CA1 cell receives input for every spatial location along the track as opposed to receiving the most substantial input only at the specific track location of the cell’s place field.

Thus, place cells predominantly express their fields through the potentiation of specific subsets of spatially tuned inputs. In accordance with this we found that the dendrites of individual place cells indeed received excitatory input at track locations both inside and outside the somatic place field (Harvey, Collman et al. 2009, Lee, Lin et al. 2012, Bittner, Grienberger et al. 2015, Bittner, Milstein et al. 2017), and that many of these inputs are highly spatially tuned to different track locations (Figure 3.2 f-h). This pattern of input distribution was evident in both place cells and non-place cells. However, in opposition to the notion that place cells receive a uniform distribution of inputs reflecting all spatial locations on a track we found that in place cells there is greater total excitatory input inside versus outside of the somatic place field (Figure 3.2). Additionally, this increase of in-field excitatory input was due to a greater number of place-ROIs with spatial tuning overlapping the somatic field as opposed to simply a greater number of active ROIs at the field location. This implies that place cells receive greater total excitatory input inside versus outside of the somatic place field and this increase originates mainly from the most spatially selective inputs. Thus, place firing is driven in part by an increase in the number of spatially-tuned excitatory inputs releasing glutamate at the site of the somatic field instead of, or in addition to, the selective post-synaptic potentiation of specific subsets of spatially tuned inputs.

5.4 Inputs to CA1 Place cells are functionally clustered.

Co-incident synaptic activation can lead to the generation of local NMDA spikes and plateau potentials in CA1 dendrites and has been implicated in initiation of synaptic potentiation in the absence of somatic spiking in these cells (Hardie and Spruston 2009). This mechanism could promote the potentiation of branch- specific clusters of inputs thereby increasing the influence of subsets of clustered inputs on somatic output. These regenerative dendritic events are implicated in the formation of new place fields in CA1 neurons (Bittner, Grienberger et al. 2015, Sheffield, Adoff et al. 2017) but whether they are the result of synaptic input clustering has yet to be determined.

Using iGluSnFR we found that excitatory input to place cell dendrites displayed functional clustering on the ~10 μm scale and this clustering was more pronounced in the somatic place field versus outside. This spatial spread is in line with other work investigating synaptic clustering (Kleindienst, Winnubst et al. 2011, Takahashi, Kitamura et al. 2012, Scholl, Wilson et al. 2017) and co-activation of spatially clustered synapses at this scale can drive nonlinear responses in dendrites (Losonczy and Magee 2006, Wilson, Whitney et al. 2016). There are several possible mechanisms by which inputs can be spatially clustered. 1. A population of presynaptic neurons converge their axons onto a small segment of a postsynaptic dendrite and activate nearby spines simultaneously through synchronous release of glutamate. 2. A single presynaptic axon makes multiple synaptic connections onto a small dendritic segment and activates nearby spines through synchronous release of glutamate from multiple boutons. 3. Multiple vesicular release of glutamate from a single synapse diffuses out of the cleft and activates neighboring synapses through spillover. To discriminate these between these mechanisms, we characterized the spatiotemporal properties of single ROI and large spatial extent iGluSnFR transients. Our analysis of the spatial spread of these large-scale glutamate events implies that they are likely generated by synchronized-release of vesicles from different presynaptic terminals rather than large multi-vesicular release events on to a single synapse that spill over onto neighboring regions. This is supported by a recent anatomical study using serial-section transmission electron microscopy to probe hippocampal connectivity. The authors found that single presynaptic axons could form multiple synapses at nearby locations on a dendritic segment but that these clustered synapses occurred predominantly at apical tuft dendrites from entorhinal afferents and were rarely found in the more proximal basal and apical dendrites (Bloss, Cembrowski et al. 2018). Spillover of glutamate through multi-vesicular release events can lead to the activation of extrasynaptic NMDARs and metabotropic glutamate receptors located on the dendritic shaft as well as glutamate receptors in neighboring synapses (Kullmann, Erdemli et al. 1996). To discern the impact of spillover on our in vivo recordings either from multi-vesicular release events onto iGluSnFR-labeled dendrites or from synapses onto adjacent unlabeled dendrites of other neurons we analyzed the spatiotemporal profile of the iGluSnFR transients within and across each 1 um ROI box. Most (76%) *in vivo* iGluSnFR transients were contained within a single 1-micron ROI (an additional 15% were contained within 2 adjacent 1-micron ROIs likely representing single synapses bisected by the ROIs). This indicates that most glutamate spilling over beyond the synapse and detected by iGluSnFR is highly localized on CA1 dendrites and any change in fluorescence generated from glutamate spilling over from neighboring neurons would likely be too weak to detect. Additionally, since significant glutamate spillover would be expected to increase signal correlations between ROIs on different dendritic branches, our observation of a flat correlation versus inter-dendrite ROI distance down to 2-3 microns indicates little glutamate spillover down to at least 2-3 microns. This result differs from findings using iGluSnFR in layer 2/3 visual cortex neurons in anaesthetized mice that showed correlated spatially structured activity between dendrites on a scale of approximately 50 µm (Kazemipour, Novak et al. 2019). This implies that both the brain region and cognitive state of the animal may influence network connectivity and signaling properties. Our observations thus suggest that most spillover detected by iGluSnFR is highly localized on CA1 dendrites during behavior. Thus mechanisms 2 and 3 are unlikely and our analysis of the spatial spread of glutamate events points to mechanism 1 and implies that the large-scale glutamate transients seen in vivo are likely generated by synchronized-release of vesicles from different presynaptic terminals rather than large multi-vesicular release events on to a single synapse that spill over onto neighboring regions. These analyses and results implicate a role for super-linear dendritic summation in CA1 place field firing, indicating that post-synaptic strength is not the sole determinant of field location, as is currently thought. This finding is also consistent with our previous in vivo dendritic calcium imaging data demonstrating dendritic branch spiking during place firing (Sheffield and Dombeck 2015).

5.5 Are we detecting single vesicle release?

While the exact resolution limits have yet to be empirically determined, previous work has indicated that iGluSnFR can reliably report the release of individual synaptic vesicles (Marvin, Borghuis et al. 2013). To verify the sensitivity of iGluSnFR, we used glutamate uncaging in mouse brain slices to investigate the relationship between glutamate release at single spines and iGluSnFR transient amplitudes. This was done by changing the amount of glutamate released onto iGluSnFR-labeled CA1 basal dendritic spines in a step-wise fashion through incremental increases in uncaging laser power. These experiments showed a linear relationship between uncaging laser power and iGluSnFR amplitude in the physiologically-relevant range of glutamate release, as determined by the average amplitude of evoked-EPSPs of the same amplitude and duration as single vesicle release mini-EPSPs. This range of laser power stimulations (25-29mW) mimicking single vesicle release from electrophysiological recordings of CA1 neurons in TTX and is corroborated by a recent study using a similar laser power to evoke single vesicle release events which generated iGluSnFR transients of similar amplitude and duration to our in vitro findings (Soares, Trotter et al. 2019). Using the iGluSnFR transient amplitudes generated by this stimulation range as a proxy for unitary signals we determined that approximately 80% of the single release events are retained in our in vivo recordings and imply that the operating range and resolution of iGluSnFR allow for measurements of excitatory synaptic input to CA1 pyramidal neuron dendrites with single vesicle sensitivity at the 1 µm spatial scale in behaving mice. To further verify our detection threshold in vivo future analyses to infer quantal parameters from iGluSnFR recording should be conducted. iGluSnFR provides a favorable proxy to measure glutamate release at single synapses compared to calcium-based and electrophysiological-based measurements of synaptic release, whose responses depend on the density and conductance of glutamate receptors which can vary from spine to spine (Biederer, Kaeser et al. 2017, Padamsey, Tong et al. 2019). iGluSnFR signals do not rely on postsynaptic glutamate receptor activation and due to its homogenous expression on the plasma membrane can report glutamate release independently of the site of vesicular release (Soares, Trotter et al. 2019). Quantal analysis aims to deduce the three quantal parameters thought to define synaptic strength, the total number of vesicles ready to be released (n), the single vesicle release probability (p), and the quantal size (q) by using binomial model to predict the amplitude distribution of the three parameters and the standard deviation of quantal content (Del Castillo and Katz 1954). Since iGluSnFR reports physiologically-relevant glutamate release in a linear fashion, the unitary response to the release of a single vesicle (q) (measured in units of $\Delta F/F$) can be quantitatively determined. Using this approach or other methods of quantal analysis (Soares, Trotter et al. 2019) at single ROIs will provide insight into the precise mechanisms of information transfer occurring at synapses in vivo.

5.6 A new model for place field formation

It was recently proposed that place fields may be generated through a novel form of synaptic potentiation that vastly diverges from Hebbian learning rules. In this mechanism, dubbed behavioral time scale synaptic plasticity (BTSP), place fields could be produced in vivo in a single trial by potentiation of input that arrived seconds before and after plateau potentials. Thus, inputs that did not necessarily participate in the generation of a plateau potential could be potentiated over an extended time-period resulting in the appearance of a new place field. This learning rule depends on a yet to be defined external instructive signal as the source of the initial depolarization causing the plateau potential and subsequent place field (Bittner, Milstein et al. 2017). A potential source for the initial depolarizing signal could be the local dendritic NMDA spikes observed during de novo place field formation in novel environments (Sheffield, Adoff et al. 2017). Clustered coincident inputs such as those recorded with iGluSnFR imaging could generate local NMDA spikes, which in turn potentiate local inputs sufficiently to evoke a plateau potential. The plateau potential will in turn potentiate additional inputs through BTSP which may promote a greater number of spatially-tuned excitatory inputs at the site of the somatic field through presynaptic Hebbian plasticity mechanisms (Enoki, Hu et al. 2009). Thus, place fields could emerge via a combination of Hebbian and non-Hebbian plasticity mechanisms that rely on the initial functional organization of inputs, the strength of the inputs, the cognitive state of the animal, and other factors (inhibition) (Schiller, Berlin et al. 2018).

5.7 Concluding remarks

How inputs are organized along a given stretch of dendrite has implications for how they are integrated (i.e. supra-linearly vs. linearly) to contribute to action potential output. Clustered inputs have been shown to generate dendritic spikes *in vitro* which result from the supra-linear summation of concurrently activated synapses (Losonczy and Magee 2006). Because dendritic spikes can be generated in individual branches across the dendritic arbor, each dendrite has the capability to independently integrate synaptic inputs in a supra-linear fashion. This compartmentalization likely provides a massive increase in the computational power of a single neuron as it enables individual dendrites to selectively influence neuronal output depending on the spatiotemporal patterns of synaptic activity. Alternatively, previous studies have suggested that the occurrence of randomly distributed inputs throughout the dendrites indicates that the soma is the main site of synaptic integration and that dendrites may primarily function to passively collect and transmit synaptic inputs (Cash and Yuste 1999). When I began my thesis project it was unknown which mode of synaptic integration predominates during place cell firing *in vivo*. Little progress has been made since in answering this question. Thus, my project is one of the first to address this question and several others by imaging dendritic activity and the patterns of synaptic input to hippocampal place cells during navigation behavior using in vivo two-photon imaging of calcium and glutamate transients. These experiments have provided valuable insight into the type of information CA1 pyramidal neurons receive during awake behavior such as the degree and proportion of incoming spatially-tuned inputs and how this differs in comparison to non-place cells. Additionally, our finding that the spatial tuning of inputs to place cells appears to be weighted toward the specific location of the somatic field as opposed to being evenly distributed across space has major implications for how place fields develop their spatially specific firing patterns and challenges the current dogma which depends purely on post synaptic plasticity. Perhaps most interesting was our finding that input to place cells appears to be anatomically and functionally clustered along CA1 dendrites on the ~10 μm scale and that this clustering was more pronounced within the somatic place field versus outside. Our findings provide the strongest evidence yet that recruitment of dendritic super-linear summation occurs during behavior and imparts a key missing piece of the puzzle to test current models of place field formation. Overall, our results support a new model in which CA1 neurons receive inputs from multiple upstream place cells with CA1 place specific firing being determined by an increased number of synapses from presynaptic neurons with the same field which form functional clusters onto CA1 neuron dendrites to drive place specific firing.

References

(1950). "Hebb, D. O. Organization of behavior. New York: Wiley, 1949, pp. 335, $4.00." Journal of Clinical Psychology **6**(3): 307-307.

Ahmed, O. J. and M. R. Mehta (2009). "The hippocampal rate code: anatomy, physiology and theory." Trends Neurosci **32**(6): 329-338.

Ali, F. and A. C. Kwan (2020). "Interpreting in vivo calcium signals from neuronal cell bodies, axons, and dendrites: a review." Neurophotonics **7**(1): 011402.

Ariav, G., A. Polsky and J. Schiller (2003). "Submillisecond precision of the input-output transformation function mediated by fast sodium dendritic spikes in basal dendrites of CA1 pyramidal neurons." J Neurosci **23**(21): 7750-7758.

Aronov, D. and D. W. Tank (2014). "Engagement of neural circuits underlying 2D spatial navigation in a rodent virtual reality system." Neuron **84**(2): 442-456.

Asztely, F., G. Erdemli and D. M. Kullmann (1997). "Extrasynaptic glutamate spillover in the hippocampus: dependence on temperature and the role of active glutamate uptake." Neuron **18**(2): 281-293.

Berns, D. S., L. A. DeNardo, D. T. Pederick and L. Luo (2018). "Teneurin-3 controls topographic circuit assembly in the hippocampus." Nature **554**(7692): 328-333.

Biederer, T., P. S. Kaeser and T. A. Blanpied (2017). "Transcellular Nanoalignment of Synaptic Function." Neuron **96**(3): 680-696.

Bittner, K. C., C. Grienberger, S. P. Vaidya, A. D. Milstein, J. J. Macklin, J. Suh, S. Tonegawa and J. C. Magee (2015). "Conjunctive input processing drives feature selectivity in hippocampal CA1 neurons." Nat Neurosci **18**(8): 1133-1142.

Bittner, K. C., A. D. Milstein, C. Grienberger, S. Romani and J. C. Magee (2017). "Behavioral time scale synaptic plasticity underlies CA1 place fields." Science **357**(6355): 1033-1036.

Bliss, T. V. and G. L. Collingridge (1993). "A synaptic model of memory: long-term potentiation in the hippocampus." Nature **361**(6407): 31-39.

Bloodgood, B. L., A. J. Giessel and B. L. Sabatini (2009). "Biphasic synaptic Ca influx arising from compartmentalized electrical signals in dendritic spines." PLoS Biol **7**(9): e1000190.

Bloodgood, B. L. and B. L. Sabatini (2007). "Nonlinear regulation of unitary synaptic signals by CaV(2.3) voltage-sensitive calcium channels located in dendritic spines." Neuron **53**(2): 249-260.

Bloss, E. B., M. S. Cembrowski, B. Karsh, J. Colonell, R. D. Fetter and N. Spruston (2018). "Single excitatory axons form clustered synapses onto CA1 pyramidal cell dendrites." Nat Neurosci **21**(3): 353-363.

Blum, K. I. and L. F. Abbott (1996). "A model of spatial map formation in the hippocampus of the rat." Neural Comput **8**(1): 85-93.

Bolshakov, V. Y. and S. A. Siegelbaum (1995). "Regulation of hippocampal transmitter release during development and long-term potentiation." Science **269**(5231): 1730-1734.

Borghuis, B. G. (2019). Two-Photon Fluorescence Imaging of Visually Evoked Glutamate Release Using iGluSnFR in the Mouse Visual System. Multiphoton Microscopy. E. Hartveit. New York, NY, Springer New York**:** 87-109.

Bostock, E., R. U. Muller and J. L. Kubie (1991). "Experience-dependent modifications of hippocampal place cell firing." Hippocampus **1**(2): 193-205.

Brandalise, F., S. Carta, F. Helmchen, J. Lisman and U. Gerber (2016). "Dendritic NMDA spikes are necessary for timing-dependent associative LTP in CA3 pyramidal cells." Nat Commun **7**: 13480.

Burgess, N. and J. O'Keefe (1996). "Neuronal computations underlying the firing of place cells and their role in navigation." Hippocampus **6**(6): 749-762.

Buzsaki, G. and E. I. Moser (2013). "Memory, navigation and theta rhythm in the hippocampal-entorhinal system." Nat Neurosci **16**(2): 130-138.

Cacucci, F., T. J. Wills, C. Lever, K. P. Giese and J. O'Keefe (2007). "Experience-dependent increase in CA1 place cell spatial information, but not spatial reproducibility, is dependent on the autophosphorylation of the alpha-isoform of the calcium/calmodulin-dependent protein kinase II." J Neurosci **27**(29): 7854-7859.

Carr, M. F., S. P. Jadhav and L. M. Frank (2011). "Hippocampal replay in the awake state: a potential substrate for memory consolidation and retrieval." Nat Neurosci **14**(2): 147-153.

Cash, S. and R. Yuste (1999). "Linear summation of excitatory inputs by CA1 pyramidal neurons." Neuron **22**(2): 383-394.

Chen, S. X., A. N. Kim, A. J. Peters and T. Komiyama (2015). "Subtype-specific plasticity of inhibitory circuits in motor cortex during motor learning." Nat Neurosci **18**(8): 1109-1115.

Chen, T. W., T. J. Wardill, Y. Sun, S. R. Pulver, S. L. Renninger, A. Baohan, E. R. Schreiter, R. A. Kerr, M. B. Orger, V. Jayaraman, L. L. Looger, K. Svoboda and D. S. Kim (2013). "Ultrasensitive fluorescent proteins for imaging neuronal activity." Nature **499**(7458): 295-300.

Chen, X., U. Leischner, N. L. Rochefort, I. Nelken and A. Konnerth (2011). "Functional mapping of single spines in cortical neurons in vivo." Nature **475**(7357): 501-505.

Chen, X., U. Leischner, Z. Varga, H. Jia, D. Deca, N. L. Rochefort and A. Konnerth (2012). "LOTOS-based two-photon calcium imaging of dendritic spines in vivo." Nat Protoc **7**(10): 1818-1829.

Chu, H. Y., J. F. Atherton, D. Wokosin, D. J. Surmeier and M. D. Bevan (2015). "Heterosynaptic regulation of external globus pallidus inputs to the subthalamic nucleus by the motor cortex." Neuron **85**(2): 364-376.

Cichon, J. and W. B. Gan (2015). "Branch-specific dendritic Ca(2+) spikes cause persistent synaptic plasticity." Nature **520**(7546): 180-185.

Clements, J. D. (1996). "Transmitter timecourse in the synaptic cleft: its role in central synaptic function." Trends Neurosci **19**(5): 163-171.

Clements, J. D., R. A. Lester, G. Tong, C. E. Jahr and G. L. Westbrook (1992). "The time course of glutamate in the synaptic cleft." Science **258**(5087): 1498-1501.

Cohen, J. D., M. Bolstad and A. K. Lee (2017). "Experience-dependent shaping of hippocampal CA1 intracellular activity in novel and familiar environments." Elife **6**.

Dana, H., B. Mohar, Y. Sun, S. Narayan, A. Gordus, J. P. Hasseman, G. Tsegaye, G. T. Holt, A. Hu, D. Walpita, R. Patel, J. J. Macklin, C. I. Bargmann, M. B. Ahrens, E. R. Schreiter, V. Jayaraman, L. L. Looger, K. Svoboda and D. S. Kim (2016). "Sensitive red protein calcium indicators for imaging neural activity." Elife **5**.

Davoudi, H. and D. J. Foster (2019). "Acute silencing of hippocampal CA3 reveals a dominant role in place field responses." Nat Neurosci **22**(3): 337-342.

Deguchi, Y., F. Donato, I. Galimberti, E. Cabuy and P. Caroni (2011). "Temporally matched subpopulations of selectively interconnected principal neurons in the hippocampus." Nat Neurosci **14**(4): 495-504.

Del Castillo, J. and B. Katz (1954). "Quantal components of the end-plate potential." J Physiol **124**(3): 560-573.

Diamond, J. S. and C. E. Jahr (1997). "Transporters buffer synaptically released glutamate on a submillisecond time scale." J Neurosci **17**(12): 4672-4687.

Dombeck, D. A., C. D. Harvey, L. Tian, L. L. Looger and D. W. Tank (2010). "Functional imaging of hippocampal place cells at cellular resolution during virtual navigation." Nat Neurosci **13**(11): 1433-1440.

Dombeck, D. A., C. D. Harvey, L. Tian, L. L. Looger and D. W. Tank (2010). "Functional imaging of hippocampal place cells at cellular resolution during virtual navigation." Nature neuroscience **13**(11): 1433-1440.

Dombeck, D. A., A. N. Khabbaz, F. Collman, T. L. Adelman and D. W. Tank (2007). "Imaging large-scale neural activity with cellular resolution in awake, mobile mice." Neuron **56**(1): 43-57.

Dragoi, G., K. D. Harris and G. Buzsaki (2003). "Place representation within hippocampal networks is modified by long-term potentiation." Neuron **39**(5): 843-853.

Dragoi, G. and S. Tonegawa (2011). "Preplay of future place cell sequences by hippocampal cellular assemblies." Nature **469**(7330): 397-401.

Dragoi, G. and S. Tonegawa (2013). "Distinct preplay of multiple novel spatial experiences in the rat." Proc Natl Acad Sci U S A **110**(22): 9100-9105.

Dragoi, G. and S. Tonegawa (2014). "Selection of preconfigured cell assemblies for representation of novel spatial experiences." Philos Trans R Soc Lond B Biol Sci **369**(1635): 20120522.

Druckmann, S., L. Feng, B. Lee, C. Yook, T. Zhao, J. C. Magee and J. Kim (2014). "Structured synaptic connectivity between hippocampal regions." Neuron **81**(3): 629-640.

Ego-Stengel, V. and M. A. Wilson (2007). "Spatial selectivity and theta phase precession in CA1 interneurons." Hippocampus **17**(2): 161-174.

Ekstrom, A. D., J. Meltzer, B. L. McNaughton and C. A. Barnes (2001). "NMDA receptor antagonism blocks experience-dependent expansion of hippocampal "place fields"." Neuron **31**(4): 631-638.

Ellis-Davies, G. C. R. (2018). "Two-Photon Uncaging of Glutamate." Front Synaptic Neurosci **10**: 48.

Enoki, R., Y. L. Hu, D. Hamilton and A. Fine (2009). "Expression of long-term plasticity at individual synapses in hippocampus is graded, bidirectional, and mainly presynaptic: optical quantal analysis." Neuron **62**(2): 242-253.

Fernandez-Ruiz, A., A. Oliva, G. A. Nagy, A. P. Maurer, A. Berenyi and G. Buzsaki (2017). "Entorhinal-CA3 Dual-Input Control of Spike Timing in the Hippocampus by Theta-Gamma Coupling." Neuron **93**(5): 1213-1226 e1215.

Foster, D. J. and M. A. Wilson (2006). "Reverse replay of behavioural sequences in hippocampal place cells during the awake state." Nature **440**(7084): 680-683.

Frank, L. M., G. B. Stanley and E. N. Brown (2004). "Hippocampal plasticity across multiple days of exposure to novel environments." J Neurosci **24**(35): 7681-7689.

Frick, A., J. Magee and D. Johnston (2004). "LTP is accompanied by an enhanced local excitability of pyramidal neuron dendrites." Nat Neurosci **7**(2): 126-135.

Fyhn, M., T. Hafting, A. Treves, M. B. Moser and E. I. Moser (2007). "Hippocampal remapping and grid realignment in entorhinal cortex." Nature **446**(7132): 190-194.

Gasparini, S., M. Migliore and J. C. Magee (2004). "On the initiation and propagation of dendritic spikes in CA1 pyramidal neurons." J Neurosci **24**(49): 11046-11056.

Goldberg, E. M. and D. A. Coulter (2013). "Mechanisms of epileptogenesis: a convergence on neural circuit dysfunction." Nat Rev Neurosci **14**(5): 337-349.

Golding, N. L., N. P. Staff and N. Spruston (2002). "Dendritic spikes as a mechanism for cooperative long-term potentiation." Nature **418**(6895): 326-331.

Gomez Gonzalez, J. F., B. W. Mel and P. Poirazi (2011). "Distinguishing Linear vs. Non-Linear Integration in CA1 Radial Oblique Dendrites: It's about Time." Front Comput Neurosci **5**: 44.

Grienberger, C., X. Chen and A. Konnerth (2014). "NMDA receptor-dependent multidendrite Ca(2+) spikes required for hippocampal burst firing in vivo." Neuron **81**(6): 1274-1281.

Grienberger, C., X. W. Chen and A. Konnerth (2015). "Dendritic function in vivio." Trends in Neurosciences **38**(1): 45-54.

Hafting, T., M. Fyhn, T. Bonnevie, M. B. Moser and E. I. Moser (2008). "Hippocampus-independent phase precession in entorhinal grid cells." Nature **453**(7199): 1248-1252.

Hafting, T., M. Fyhn, S. Molden, M. B. Moser and E. I. Moser (2005). "Microstructure of a spatial map in the entorhinal cortex." Nature **436**(7052): 801-806.

Hainmueller, T. and M. Bartos (2018). "Parallel emergence of stable and dynamic memory engrams in the hippocampus." Nature **558**(7709): 292-296.

Hardie, J. and N. Spruston (2009). "Synaptic depolarization is more effective than back-propagating action potentials during induction of associative long-term potentiation in hippocampal pyramidal neurons." J Neurosci **29**(10): 3233-3241.

Harvey, C. D., F. Collman, D. A. Dombeck and D. W. Tank (2009). "Intracellular dynamics of hippocampal place cells during virtual navigation." Nature **461**(7266): 941-946.

Harvey, C. D., R. Yasuda, H. Zhong and K. Svoboda (2008). "The spread of Ras activity triggered by activation of a single dendritic spine." Science **321**(5885): 136-140.

Hasselmo, M. E. and J. McGaughy (2004). "High acetylcholine levels set circuit dynamics for attention and encoding and low acetylcholine levels set dynamics for consolidation." Prog Brain Res **145**: 207-231.

Heys, J. G., K. V. Rangarajan and D. A. Dombeck (2014). "The functional micro-organization of grid cells revealed by cellular-resolution imaging." Neuron **84**(5): 1079-1090.

Hill, A. J. (1978). "First occurrence of hippocampal spatial firing in a new environment." Exp Neurol **62**(2): 282-297.

Hill, D. N., Z. Varga, H. Jia, B. Sakmann and A. Konnerth (2013). "Multibranch activity in basal and tuft dendrites during firing of layer 5 cortical neurons in vivo." Proc Natl Acad Sci U S A **110**(33): 13618-13623.

Hill, T. C. and K. Zito (2013). "LTP-induced long-term stabilization of individual nascent dendritic spines." J Neurosci **33**(2): 678-686.

Holderith, N., A. Lorincz, G. Katona, B. Rozsa, A. Kulik, M. Watanabe and Z. Nusser (2012). "Release probability of hippocampal glutamatergic terminals scales with the size of the active zone." Nat Neurosci **15**(7): 988-997.

Iacaruso, M. F., I. T. Gasler and S. B. Hofer (2017). "Synaptic organization of visual space in primary visual cortex." Nature **547**(7664): 449-452.

Jensen, T. P., K. Zheng, N. Cole, J. S. Marvin, L. L. Looger and D. A. Rusakov (2019). "Multiplex imaging relates quantal glutamate release to presynaptic Ca(2+) homeostasis at multiple synapses in situ." Nat Commun **10**(1): 1414.

Jia, H., N. L. Rochefort, X. Chen and A. Konnerth (2010). "Dendritic organization of sensory input to cortical neurons in vivo." Nature **464**(7293): 1307-1312.

Kazemipour, A., O. Novak, D. Flickinger, J. S. Marvin, A. S. Abdelfattah, J. King, P. M. Borden, J. J. Kim, S. H. Al-Abdullatif, P. E. Deal, E. W. Miller, E. R. Schreiter, S. Druckmann, K. Svoboda, L. L. Looger and K. Podgorski (2019). "Kilohertz frame-rate two-photon tomography." Nat Methods **16**(8): 778-786.

Kentros, C., E. Hargreaves, R. D. Hawkins, E. R. Kandel, M. Shapiro and R. V. Muller (1998). "Abolition of long-term stability of new hippocampal place cell maps by NMDA receptor blockade." Science **280**(5372): 2121-2126.

Kentros, C. G., N. T. Agnihotri, S. Streater, R. D. Hawkins and E. R. Kandel (2004). "Increased attention to spatial context increases both place field stability and spatial memory." Neuron **42**(2): 283-295.

Kerlin, A., M. Boaz, D. Flickinger, B. J. MacLennan, M. B. Dean, C. Davis, N. Spruston and K. Svoboda (2019). "Functional clustering of dendritic activity during decision-making." Elife **8**.

Kleindienst, T., J. Winnubst, C. Roth-Alpermann, T. Bonhoeffer and C. Lohmann (2011). "Activity-dependent clustering of functional synaptic inputs on developing hippocampal dendrites." Neuron **72**(6): 1012-1024.

Kullmann, D. M., G. Erdemli and F. Asztely (1996). "LTP of AMPA and NMDA receptor-mediated signals: evidence for presynaptic expression and extrasynaptic glutamate spill-over." Neuron **17**(3): 461-474.

Langston, R. F., J. A. Ainge, J. J. Couey, C. B. Canto, T. L. Bjerknes, M. P. Witter, E. I. Moser and M. B. Moser (2010). "Development of the spatial representation system in the rat." Science **328**(5985): 1576-1580.

Larkum, M. E. and T. Nevian (2008). "Synaptic clustering by dendritic signalling mechanisms." Curr Opin Neurobiol **18**(3): 321-331.

Lavzin, M., S. Rapoport, A. Polsky, L. Garion and J. Schiller (2012). "Nonlinear dendritic processing determines angular tuning of barrel cortex neurons in vivo." Nature **490**(7420): 397-401.

Lee, D., B. J. Lin and A. K. Lee (2012). "Hippocampal place fields emerge upon single-cell manipulation of excitability during behavior." Science **337**(6096): 849-853.

Leutgeb, S., J. K. Leutgeb, C. A. Barnes, E. I. Moser, B. L. McNaughton and M. B. Moser (2005). "Independent codes for spatial and episodic memory in hippocampal neuronal ensembles." Science **309**(5734): 619-623.

Leutgeb, S., J. K. Leutgeb, A. Treves, M. B. Moser and E. I. Moser (2004). "Distinct ensemble codes in hippocampal areas CA3 and CA1." Science **305**(5688): 1295-1298.

Lever, C., T. Wills, F. Cacucci, N. Burgess and J. O'Keefe (2002). "Long-term plasticity in hippocampal place-cell representation of environmental geometry." Nature **416**(6876): 90-94.

Lin, M. Z. and M. J. Schnitzer (2016). "Genetically encoded indicators of neuronal activity." Nat Neurosci **19**(9): 1142-1153.

Lorente De Nó, R. (1934). "Studies on the structure of the cerebral cortex. II. Continuation of the study of the ammonic system." Journal für Psychologie und Neurologie **46**: 113-177.

Losonczy, A. and J. C. Magee (2006). "Integrative properties of radial oblique dendrites in hippocampal CA1 pyramidal neurons." Neuron **50**(2): 291-307.

Losonczy, A., J. K. Makara and J. C. Magee (2008). "Compartmentalized dendritic plasticity and input feature storage in neurons." Nature **452**(7186): 436-441.

Lovett-Barron, M., P. Kaifosh, M. A. Kheirbek, N. Danielson, J. D. Zaremba, T. R. Reardon, G. F. Turi, R. Hen, B. V. Zemelman and A. Losonczy (2014). "Dendritic inhibition in the hippocampus supports fear learning." Science **343**(6173): 857-863.

Magee, J. C. and D. Johnston (1997). "A synaptically controlled, associative signal for Hebbian plasticity in hippocampal neurons." Science **275**(5297): 209-213.

Major, G., A. Polsky, W. Denk, J. Schiller and D. W. Tank (2008). "Spatiotemporally graded NMDA spike/plateau potentials in basal dendrites of neocortical pyramidal neurons." J Neurophysiol **99**(5): 2584-2601.

Mankin, E. A., G. W. Diehl, F. T. Sparks, S. Leutgeb and J. K. Leutgeb (2015). "Hippocampal CA2 activity patterns change over time to a larger extent than between spatial contexts." Neuron **85**(1): 190-201.

Marr, D. (1971). "Simple memory: a theory for archicortex." Philos Trans R Soc Lond B Biol Sci **262**(841): 23-81.

Marvin, J. S., B. G. Borghuis, L. Tian, J. Cichon, M. T. Harnett, J. Akerboom, A. Gordus, S. L. Renninger, T. W. Chen, C. I. Bargmann, M. B. Orger, E. R. Schreiter, J. B. Demb, W. B. Gan, S. A. Hires and L. L. Looger (2013). "An optimized fluorescent probe for visualizing glutamate neurotransmission." Nat Methods **10**(2): 162-170.

Marvin, J. S., B. Scholl, D. E. Wilson, K. Podgorski, A. Kazemipour, J. A. Muller, S. Schoch, F. J. U. Quiroz, N. Rebola, H. Bao, J. P. Little, A. N. Tkachuk, E. Cai, A. W. Hantman, S. S. Wang, V. J. DePiero, B. G. Borghuis, E. R. Chapman, D. Dietrich, D. A. DiGregorio, D. Fitzpatrick and L. L. Looger (2018). "Stability, affinity, and chromatic variants of the glutamate sensor iGluSnFR." Nat Methods **15**(11): 936-939.

McHugh, T. J., K. I. Blum, J. Z. Tsien, S. Tonegawa and M. A. Wilson (1996). "Impaired hippocampal representation of space in CA1-specific NMDAR1 knockout mice." Cell **87**(7): 1339-1349.

McNaughton, B. L., F. P. Battaglia, O. Jensen, E. I. Moser and M. B. Moser (2006). "Path integration and the neural basis of the 'cognitive map'." Nat Rev Neurosci **7**(8): 663-678.

Megias, M., Z. Emri, T. F. Freund and A. I. Gulyas (2001). "Total number and distribution of inhibitory and excitatory synapses on hippocampal CA1 pyramidal cells." Neuroscience **102**(3): 527-540.

Mehta, M. R., M. C. Quirk and M. A. Wilson (2000). "Experience-dependent asymmetric shape of hippocampal receptive fields." Neuron **25**(3): 707-715.

Miller, K. D. (1996). "Synaptic economics: competition and cooperation in synaptic plasticity." Neuron **17**(3): 371-374.

Milojkovic, B. A., W. L. Zhou and S. D. Antic (2007). "Voltage and calcium transients in basal dendrites of the rat prefrontal cortex." J Physiol **585**(Pt 2): 447-468.

Miri, A., K. Daie, R. D. Burdine, E. Aksay and D. W. Tank (2011). "Regression-based identification of behavior-encoding neurons during large-scale optical imaging of neural activity at cellular resolution." J Neurophysiol **105**(2): 964-980.

Mizuseki, K., S. Royer, K. Diba and G. Buzsaki (2012). "Activity dynamics and behavioral correlates of CA3 and CA1 hippocampal pyramidal neurons." Hippocampus **22**(8): 1659-1680.

Monaco, J. D., G. Rao, E. D. Roth and J. J. Knierim (2014). "Attentive scanning behavior drives one-trial potentiation of hippocampal place fields." Nat Neurosci **17**(5): 725-731.

Morris, R. G., E. Anderson, G. S. Lynch and M. Baudry (1986). "Selective impairment of learning and blockade of long-term potentiation by an N-methyl-D-aspartate receptor antagonist, AP5." Nature **319**(6056): 774-776.

Morris, R. G., P. Garrud, J. N. Rawlins and J. O'Keefe (1982). "Place navigation impaired in rats with hippocampal lesions." Nature **297**(5868): 681-683.

Mukamel, E. A., A. Nimmerjahn and M. J. Schnitzer (2009). "Automated analysis of cellular signals from large-scale calcium imaging data." Neuron **63**(6): 747-760.

Muller, R. U. and J. L. Kubie (1987). "The effects of changes in the environment on the spatial firing of hippocampal complex-spike cells." J Neurosci **7**(7): 1951-1968.

Murakoshi, H. and R. Yasuda (2012). "Postsynaptic signaling during plasticity of dendritic spines." Trends Neurosci **35**(2): 135-143.

Nakai, J., M. Ohkura and K. Imoto (2001). "A high signal-to-noise Ca(2+) probe composed of a single green fluorescent protein." Nat Biotechnol **19**(2): 137-141.

O'Keefe, J. (1976). "Place units in the hippocampus of the freely moving rat." Exp Neurol **51**(1): 78-109.

O'Keefe, J. and J. Dostrovsky (1971). "The hippocampus as a spatial map. Preliminary evidence from unit activity in the freely-moving rat." Brain Res **34**(1): 171-175.

O'Keefe, J. and L. Nadel (1978). The hippocampus as a cognitive map. Oxford; New York, Clarendon Press ; Oxford University Press.

Oakley, J. C., P. C. Schwindt and W. E. Crill (2001). "Initiation and propagation of regenerative Ca(2+)-dependent potentials in dendrites of layer 5 pyramidal neurons." J Neurophysiol **86**(1): 503-513.

Oh, W. C., L. K. Parajuli and K. Zito (2015). "Heterosynaptic structural plasticity on local dendritic segments of hippocampal CA1 neurons." Cell Rep **10**(2): 162-169.

Padamsey, Z., R. Tong and N. Emptage (2019). "Optical Quantal Analysis Using Ca(2+) Indicators: A Robust Method for Assessing Transmitter Release Probability at Excitatory Synapses by Imaging Single Glutamate Release Events." Front Synaptic Neurosci **11**: 5.

Palmer, L. M., A. S. Shai, J. E. Reeve, H. L. Anderson, O. Paulsen and M. E. Larkum (2014). "NMDA spikes enhance action potential generation during sensory input." Nat Neurosci **17**(3): 383-390.

Pnevmatikakis, E. A. and A. Giovannucci (2017). "NoRMCorre: An online algorithm for piecewise rigid motion correction of calcium imaging data." J Neurosci Methods **291**: 83-94.

Pologruto, T. A., B. L. Sabatini and K. Svoboda (2003). "ScanImage: flexible software for operating laser scanning microscopes." Biomed Eng Online **2**: 13.

Redish, A. D., F. P. Battaglia, M. K. Chawla, A. D. Ekstrom, J. L. Gerrard, P. Lipa, E. S. Rosenzweig, P. F. Worley, J. F. Guzowski, B. L. McNaughton and C. A. Barnes (2001). "Independence of firing correlates of anatomically proximate hippocampal pyramidal cells." J Neurosci **21**(5): RC134.

Rossato, J. I., A. Moreno, L. Genzel, M. Yamasaki, T. Takeuchi, S. Canals and R. G. M. Morris (2018). "Silent Learning." Curr Biol **28**(21): 3508-3515 e3505.

Rotenberg, A., M. Mayford, R. D. Hawkins, E. R. Kandel and R. U. Muller (1996). "Mice expressing activated CaMKII lack low frequency LTP and do not form stable place cells in the CA1 region of the hippocampus." Cell **87**(7): 1351-1361.

Routh, B. N., D. Johnston, K. Harris and R. A. Chitwood (2009). "Anatomical and electrophysiological comparison of CA1 pyramidal neurons of the rat and mouse." J Neurophysiol **102**(4): 2288-2302.

Sadowski, J. H., M. W. Jones and J. R. Mellor (2016). "Sharp-Wave Ripples Orchestrate the Induction of Synaptic Plasticity during Reactivation of Place Cell Firing Patterns in the Hippocampus." Cell Rep **14**(8): 1916-1929.

Schiller, J., S. Berlin and D. Derdikman (2018). "The Many Worlds of Plasticity Rules." Trends Neurosci **41**(3): 124-127.

Schiller, J., G. Major, H. J. Koester and Y. Schiller (2000). "NMDA spikes in basal dendrites of cortical pyramidal neurons." Nature **404**(6775): 285-289.

Schiller, J., Y. Schiller and D. E. Clapham (1998). "NMDA receptors amplify calcium influx into dendritic spines during associative pre- and postsynaptic activation." Nat Neurosci **1**(2): 114-118.

Schmidt-Hieber, C., G. Toleikyte, L. Aitchison, A. Roth, B. A. Clark, T. Branco and M. Hausser (2017). "Active dendritic integration as a mechanism for robust and precise grid cell firing." Nat Neurosci **20**(8): 1114-1121.

Scholl, B., D. E. Wilson and D. Fitzpatrick (2017). "Local Order within Global Disorder: Synaptic Architecture of Visual Space." Neuron **96**(5): 1127-1138.e1124.

Scoville, W. B. and B. Milner (1957). "Loss of recent memory after bilateral hippocampal lesions." J Neurol Neurosurg Psychiatry **20**(1): 11-21.

Seong, H. J., R. Behnia and A. G. Carter (2014). "Impact of subthreshold membrane potential on synaptic responses at dendritic spines of layer 5 pyramidal neurons in the prefrontal cortex." J Neurophysiol **111**(10): 1960-1972.

Sheffield, M. E. and D. A. Dombeck (2015). "Calcium transient prevalence across the dendritic arbor predicts place field properties." Nature **517**(7533): 200.

Sheffield, M. E. and D. A. Dombeck (2015). "Calcium transient prevalence across the dendritic arbour predicts place field properties." Nature **517**(7533): 200-204.

Sheffield, M. E. and D. A. Dombeck (2019). "Dendritic mechanisms of hippocampal place field formation." Curr Opin Neurobiol **54**: 1-11.

Sheffield, M. E. J., M. D. Adoff and D. A. Dombeck (2017). "Increased Prevalence of Calcium Transients across the Dendritic Arbor during Place Field Formation." Neuron **96**(2): 490-504 e495.

Shoham, S., D. H. O'Connor and R. Segev (2006). "How silent is the brain: is there a "dark matter" problem in neuroscience?" J Comp Physiol A Neuroethol Sens Neural Behav Physiol **192**(8): 777-784.

Silva, A. J., R. Paylor, J. M. Wehner and S. Tonegawa (1992). "Impaired spatial learning in alpha-calcium-calmodulin kinase II mutant mice." Science **257**(5067): 206-211.

Smith, S. L., I. T. Smith, T. Branco and M. Hausser (2013). "Dendritic spikes enhance stimulus selectivity in cortical neurons in vivo." Nature **503**(7474): 115-120.

Soares, C., K. F. H. Lee and J. C. Beique (2017). "Metaplasticity at CA1 Synapses by Homeostatic Control of Presynaptic Release Dynamics." Cell Rep **21**(5): 1293-1303.

Soares, C., D. Trotter, A. Longtin, J. C. Beique and R. Naud (2019). "Parsing Out the Variability of Transmission at Central Synapses Using Optical Quantal Analysis." Front Synaptic Neurosci **11**: 22.

Solstad, T., E. I. Moser and G. T. Einevoll (2006). "From grid cells to place cells: a mathematical model." Hippocampus **16**(12): 1026-1031.

Stuart, G. J. and N. Spruston (2015). "Dendritic integration: 60 years of progress." Nat Neurosci **18**(12): 1713-1721.

Takahashi, H. and J. C. Magee (2009). "Pathway interactions and synaptic plasticity in the dendritic tuft regions of CA1 pyramidal neurons." Neuron **62**(1): 102-111.

Takahashi, N., K. Kitamura, N. Matsuo, M. Mayford, M. Kano, N. Matsuki and Y. Ikegaya (2012). "Locally synchronized synaptic inputs." Science **335**(6066): 353-356.

Takeuchi, T., A. J. Duszkiewicz and R. G. Morris (2014). "The synaptic plasticity and memory hypothesis: encoding, storage and persistence." Philos Trans R Soc Lond B Biol Sci **369**(1633): 20130288.

Teles-Grilo Ruivo, L. M., K. L. Baker, M. W. Conway, P. J. Kinsley, G. Gilmour, K. G. Phillips, J. T. Isaac, J. P. Lowry and J. R. Mellor (2017). "Coordinated Acetylcholine Release in Prefrontal Cortex and Hippocampus Is Associated with Arousal and Reward on Distinct Timescales." Cell Rep **18**(4): 905-917.

Teng, E. and L. R. Squire (1999). "Memory for places learned long ago is intact after hippocampal damage." Nature **400**(6745): 675-677.

Thompson, L. T. and P. J. Best (1989). "Place cells and silent cells in the hippocampus of freely-behaving rats." J Neurosci **9**(7): 2382-2390.

Tolman, E. C. (1948). "Cognitive maps in rats and men." Psychol Rev **55**(4): 189-208.

Tsien, J. Z., P. T. Huerta and S. Tonegawa (1996). "The essential role of hippocampal CA1 NMDA receptor-dependent synaptic plasticity in spatial memory." Cell **87**(7): 1327-1338.

van de Ven, G. M., S. Trouche, C. G. McNamara, K. Allen and D. Dupret (2016). "Hippocampal Offline Reactivation Consolidates Recently Formed Cell Assembly Patterns during Sharp Wave-Ripples." Neuron **92**(5): 968-974.

Varga, Z., H. Jia, B. Sakmann and A. Konnerth (2011). "Dendritic coding of multiple sensory inputs in single cortical neurons in vivo." Proc Natl Acad Sci U S A **108**(37): 15420-15425.

Weber, J. P., B. K. Andrasfalvy, M. Polito, A. Mago, B. B. Ujfalussy and J. K. Makara (2016). "Location-dependent synaptic plasticity rules by dendritic spine cooperativity." Nat Commun **7**: 11380.

Weber, S. N. and H. Sprekeler (2018). "Learning place cells, grid cells and invariances with excitatory and inhibitory plasticity." Elife **7**.

Wei, D. S., Y. A. Mei, A. Bagal, J. P. Kao, S. M. Thompson and C. M. Tang (2001). "Compartmentalized and binary behavior of terminal dendrites in hippocampal pyramidal neurons." Science **293**(5538): 2272-2275.

Wilent, W. B. and D. A. Nitz (2007). "Discrete place fields of hippocampal formation interneurons." J Neurophysiol **97**(6): 4152-4161.

Wills, T. J., F. Cacucci, N. Burgess and J. O'Keefe (2010). "Development of the hippocampal cognitive map in preweanling rats." Science **328**(5985): 1573-1576.

Wilson, D. E., B. Scholl and D. Fitzpatrick (2018). "Differential tuning of excitation and inhibition shapes direction selectivity in ferret visual cortex." Nature **560**(7716): 97-101.

Wilson, D. E., D. E. Whitney, B. Scholl and D. Fitzpatrick (2016). "Orientation selectivity and the functional clustering of synaptic inputs in primary visual cortex." Nat Neurosci **19**(8): 1003-1009.

Wilson, M. A. and B. L. McNaughton (1993). "Dynamics of the hippocampal ensemble code for space." Science **261**(5124): 1055-1058.

Wilson, M. A. and B. L. McNaughton (1994). "Reactivation of hippocampal ensemble memories during sleep." Science **265**(5172): 676-679.

Wu, X. E. and B. W. Mel (2009). "Capacity-enhancing synaptic learning rules in a medial temporal lobe online learning model." Neuron **62**(1): 31-41.

Xu, J., N. Kang, L. Jiang, M. Nedergaard and J. Kang (2005). "Activity-dependent long-term potentiation of intrinsic excitability in hippocampal CA1 pyramidal neurons." J Neurosci **25**(7): 1750-1760.

Zhao, X., Y. Wang, N. Spruston and J. C. Magee (2019). "Synaptic mechanisms of context-dependent sensory responses in the hippocampus " BioRxiv.

Zhou, W. L., P. Yan, J. P. Wuskell, L. M. Loew and S. D. Antic (2008). "Dynamics of action potential backpropagation in basal dendrites of prefrontal cortical pyramidal neurons." Eur J Neurosci **27**(4): 923-936.